CRYSTAL PLASTICITY FINITE ELEMENT ANALYSIS OF
DEFORMATION BEHAVIOUR IN
SAC305 SOLDER JOINT

By

Payam Darbandi

A DISSERTATION

Submitted to
Michigan State University
in partial fulfillment of the requirements
for the degree of

Mechanical Engineering-Doctor of Philosophy

2014

ABSTRACT

CRYSTAL PLASTICITY FINITE ELEMENT ANALYSIS OF
DEFORMATION BEHAVIOUR IN
SAC305 SOLDER JOINT

By

Payam Darbandi

Due to the awareness of the potential health hazards associated with the toxicity of lead (Pb), actions have been taken to eliminate or reduce the use of Pb in consumer products. Among those, tin (Sn) solders have been used for the assembly of electronic systems. Anisotropy is of significant importance in all structural metals, but this characteristic is unusually strong in Sn, making Sn based solder joints one of the best examples of the influence of anisotropy.

The effect of anisotropy arising from the crystal structure of tin and large grain microstructure on the microstructure and the evolution of constitutive responses of microscale SAC305 solder joints is investigated.

Insights into the effects of key microstructural features and dominant plastic deformation mechanisms influencing the measured relative activity of slip systems in SAC305 are obtained from a combination of optical microscopy, orientation imaging microscopy (OIM), slip plane trace analysis and crystal plasticity finite element (CPFE) modeling.

Package level SAC305 specimens were subjected to shear deformation in sequential steps and characterized using optical microscopy and OIM to identify the activity of slip systems.

X-ray micro Laue diffraction and high energy monochromatic X-ray beam were employed to characterize the joint scale tensile samples to provide necessary information to be able to compare and validate the CPFE model.

A CPFE model was developed that can account for relative ease of activating slip systems in SAC305 solder based upon the statistical estimation based on correlation between the critical resolved shear stress and the probability of activating various slip systems.

The results from simulations show that the CPFE model developed using the statistical analysis of activity of slip system not only can satisfy the requirements associated with kinematic of plastic deformation in crystal coordinate systems (activity of slip systems) and global coordinate system (shape changes) but also this model is able to predict the evolution of stress in joint level SAC305 sample.

ACKNOWLEDGMENTS

I would like to express my deepest appreciation to my advisors, Dr. Farhang Pourboghrat and Dr. Thomas Bieler, for all their supports, guidance, and encouragement during my PhD study. I would also like to thank the members of my PhD committee; Dr. Alejandro Diaz, and Dr. Thomas Pence for their constructive criticism and suggestions during the course of this work.

I would also like to acknowledge Dr. Carl Boehlert and Dr Tae-kyu Lee for their valuable assistance and support during this work.

My colleagues; Dr. Bite Zhou and Quan Zhou are greatly appreciated for their help and suggestions on this research.

Most importantly, I would like to express my greatest appreciation to my parents and Farnaz for their encouragement through the years.

TABLE OF CONTENTS

LIST OF TABLES

LIST OF FIGURES

x

CHAPTER 1

INTRODUCTION

Due to the awareness of the potential health hazards associated with the toxicity of lead, actions have been taken to eliminate or reduce the use of Pb in consumer products. Among the resulting changes, tin solders are now used for the assembly of electronic systems.

Anisotropy is of significant importance in all structural metals, but this characteristic is unusually strong in Sn, making Sn based solder joints one of the best examples of the influence of anisotropy. The mechanical properties and damage evolution in SAC 305 alloys strongly depend on the underlying microstructures. The existence of single or multi-grain microstructure in this alloy causes each joint to exhibit unique mechanical response and stress and strain history. An outcome of the inhomogeneous behavior of microscale SAC joints is reflected in their thermal cycling fatigue behavior. In general, it is expected that the first joint to fail will be located at the die or package corner where extrinsic shear strains arising from coefficients of thermal expansion (CTE) mismatch are the largest. But in reality, failed joints are not necessarily at the above stated regions. This issue is especially important for package designers. While design engineers look for simple isotropic models to use for package design, this approach is by no means effective for examining damage nucleation processes arising from the large grain microstructure and the anisotropic properties of Sn.

Given the wide range of initial microstructures that SAC 305 alloys can have, in order to conduct an experimental analysis across the entire space of feasible microstructures one needs to have unlimited resources in terms of time and cost. Therefore, developing a material model which is

sensitive to the microstructure and the initial grain orientation is particularly desirable for electronic assembly industry.

In addition to the complexity of the microstructure, the stress state that electronic components can experience is quite complicated. In service conditions, mechanical loads on the packages can vary from high temperature, low strain-rate loads such as thermal cycling, to high strain-rate loads at relatively low temperatures, such as in vibration, shock, drop and mechanical cycling at ambient temperatures [Abtew and Selvaduray (2000)].

This dissertation aims to provide an improved understanding of the modeling of anisotropy in the elastic-plastic behavior of SAC solder at sub-mm length scales, using a combination of microstructural and mechanical characterization and crystal plasticity finite element (CPFE) modeling approaches. The results of this study are applicable to the mechanical response of solders in low temperature, high strain-rate loading conditions where plastic deformation dominates over creep deformation mechanisms. This is particularly important for modeling of accelerated thermal cycling tests in which deformation based on slip mechanisms are dominant and are in common within the industry.

Specific objectives of this dissertation, regarding the unresolved research issues, are to:

1-Propose a mechanistic framework based upon the crystal plasticity finite element modeling of idealized geometries to provide insights into the effect of initial coarse-grained Sn microstructures and orientations on joint dependent deformation behavior of SAC305 solders.

2- Investigate the activities of slip systems in SAC 305 alloys utilizing the orientation imaging microscopy, SEM, and plane trace analysis on prior polished shear deformed samples to assess the effect of initial crystal orientation and evolved crystal orientations on anisotropic plastic deformation arising from the activity of different slip systems in different locations.

3- Examine the predictive capabilities of the CPFE model to capture the kinematics of inhomogeneous plastic deformation in microstructures that are commonly observed in real SAC305 solders, and to assess the relative activity of different slip systems and the evolution of microstructural features.

4- Correlate the mechanical properties, initial microstructure, and crystal orientation based on the CPFE modeling of tensile deformation of joint level samples characterized using 3D x-ray method.

A detailed literature review on the microstructural features and deformation mechanisms related to the lead free solder alloys is given in chapter 2. This chapter also describes the most significant material models that are used to model the mechanical behavior of lead free solders.

The numerical framework regarding the crystal plasticity finite element method is detailed in chapter 3. Chapter 4 describes the experimental procedures that are used in this study

Chapter 5 focuses on the applicability of the CPFE model to study the impact of external and internal constraints associated with the tri-crystal microstructure of lead free solder balls on the activity of slip systems. The correlation between the crystal grain orientation and evolution of microstructural features and activity of slip systems using CPFE, OIM, and comparative studies is given in chapter 6.

A statistical analysis on the relative activity of slip systems based on the orientation imaging microscopy method to characterize 32 shear deformed samples is detailed in chapter 7. An experimental and CPFE study on the plastic deformation of microscale tensile samples and variability in the plastic deformation response under identical loading histories due to the crystal orientation is reported in chapter 7.

Chapter 9 summarizes the results, provides conclusions, and describes needed future work.

Chapter 5 is extracted from a paper that is published in the Journal of Electronic Materials.

Chapter 6 also is extracted from a paper that is submitted to the Journal of Computational Materials Science. The results of chapter 7 will be submitted to Materials Science and Engineering A.

CHAPTER 2

LITERATURE REVIEW

Due to actions that have been taken to eliminate or reduce the use of lead (because of health risk associated with the toxicity of this metal) there has been a great amount of interest in using lead free solder alloys within the electronic assembly industry in last several years.

Reliability is one of the most important concerns regarding the elimination or reduction of Pb based solders. The most important issue with Pb-free soldering is to replace the Sn-Pb solders with alloys that have equivalent mechanical properties, satisfy the standards developed for Sn-Pb soldering, and to insure the reliability of these alloys. Parameters that are important in this regard are the coefficient of thermal expansion, elastic modulus, yield strength, shear strength, fatigue and creep behavior.

Among different choices, the tin-silver-copper (Sn-Ag-Cu or SAC) family of alloys has earned a great deal of positive response from the electronic assembly industry in recent years. Although this family of alloys has relatively low melting points, good reliability, and reasonable cost, there are significant differences between these alloys and Sn-Pb solder alloys. In lead-tin based solder alloys the prediction of failure is straightforward, but due to the anisotropy of tin and the more complicated crystal structure of this metal, it is very difficult to predict its damage initiation and evolution. This issue is clearly reflected in thermal cycling fatigue behavior of Sn based solder alloys. The highest stressed solder ball, which according to the simple mechanical calculations could be the one at the package or die corner, is not necessarily the first joint to fail during the thermal cycling of Plastic Ball Grid Arrays (PBGA).

This unexpected failure location of Pb-free solder joints creates special challenges for package designer who in the past successfully used the isotropic material models for Sn-Pb solders.

In this regard, it is important to assess the differences between the Pb- free solders and Sn-Pb alloys in the light of metallurgical considerations. The main difference between Sn-Pb and Sn based alloys is that soft and isotropic Pb in Sn-Pb alloys can dramatically reduce the anisotropic effects of Sn.

Furthermore, the anisotropy in the coefficient of thermal expansion (CTE) plays an important role in the failure process. **Figure 1.2** illustrates the anisotropy in the CTE. The crystal structure of tin is BCT (a squashed diamond cubic structure), as shown in **Figure 1.3**. The coefficient of thermal expansion is greatest in the c-axis, and the stiffness is also highest in this direction. Because of the different values of the CTE and stiffness in different directions, tin naturally is conflicted at grain boundaries. So, the morphology of grains and grain boundary orientation can have a strong effect on the mechanical properties of solders.

The stress state which electronic components can experience is also complicated. The main source of this stress, however, comes from the fact that electronic components and their supporting board have different coefficients of thermal expansion. Therefore, as the temperature rises, the board expands quite differently than electronic components mounted on it. This gives rise to a state of shear deformation, in turn developing shear stresses and strains in connecting joints. Especially, as electronic circuits pass current on and off, the solder ball becomes subjected to thermal cycling loads, which also lead to cyclic shear stresses. Furthermore, bending that may occur due to mechanical boundary conditions imposed on the electronic board can generate a state of tensile or compressive stress in the connecting solder ball. In the

6

automotive industry, vibration is of significant importance and in these applications; fatigue failure has to be considered. Vibrational failure is one of the most significant failure modes in electronic packages during their service life. In summary, in service, mechanical loads on packages can vary from high temperature, low strain-rate loads such as thermal cycling, power cycling, quasi-static isothermal mechanical cycling at elevated temperatures, to high strain-rate loads at relatively low temperatures, such as vibration, shock, drop and mechanical cycling at ambient temperatures [Abtew and Selvaduray (2000)].

There are two levels of packaging that solders are utilized in electronic assembly industry. At the first level, solder can assist in bonding of a die to substrate to provide the electrical connection. In the next level of assembly, the electronic component is mounted on a printed wiring board (PWB) using solders. One of the more common methods of surface mounting is to use solder balls, which are arranged in ball grid arrays (BGA) between the package and the board.

2.1.1 Crystal structure and physical properties of tin

The bct unit cell is shown in **Figure. 2.3**. For tin crystal structure a = 0.58194 nm and c = 0.31753 nm (c/a = 0.54564). As it is apparent, there are 8 atoms at the corners, one atom at the center and four atoms on the four faces (4 atoms per unit cell). The lattice is a distorted diamond cubic lattice (when c/a =$\sqrt{2}$ it is equivalent to the diamond cubic lattice Yang and Li (2007)). The coefficient of linear thermal expansion at room temperature is 15.4 $\times 10^{-6}$ along the a-axis and 30.5 $\times 10^{-6}$ along the c-axis. As is shown in **Figure2.2,** with increasing temperature, these coefficients increase. The role of anisotropy in CTE in developing inhomogeneous shear deformation is schematically illustrated in **Figure 2.4**. Since the coefficient of thermal expansion

in copper is about 15.4×10^{-6}, when the c-axis is parallel to the interface there is a maximum difference in the coefficient of thermal expansion between solder and the board. Subsequent thermal cycling can lead to oscillation in internal strains and cause grain boundary sliding, dislocation creep, and plastic deformation at values of stress that exceed the yield strength (Bieler et al (2012)).

2.1.2 Activity of slip systems in tin:

A review about the plastic properties of tin by Yang and Li (2007) indicates the need for better understanding of the deformation mechanisms of tin. There is incomplete understanding of slip in Sn, though single crystals have been investigated by several researchers such as Fujiwara and Hirokawa (1986, 1987) , M. Fujiwara (1997), Nagasaka (1999), Ekinci et al. (2003) , Düzgün et al. (1999) , Kouhashi and Koenronbunshu (2000) , Honda (1978,1979), Obinata and Schmid (1933), Polanyi and Schmid (1925) , Lorentz (1968), Fiedler and Lang (1972), Fiedler and Lang (1975) , Vook (1964) , Chu and Li (1979) , Obinata and Schmid (1933), Zhou at al. (2009) Matin et al. (2006) , Sidhu (2008) Chu and Li (1979), Weertman and Breen (1956) , Kirichenko and Soldatov(1982) , Ojima and Hirokawa (1983), Nagasaka (1989), Düzgün and Aytas (1993), Mark and Polanyi (1923), Telang and Bieler (2007, 2009) and Kinoshita et al.(2012) .

There is especially uncertainty about the critical resolved shear stress for different slip systems. Evidence presented by Düzgün et al. (1999, 2003), suggests that the initial critical resolved shear stress is similar on different slip systems, but they have different rates of hardening. In these studies, a limited set of crystal orientations have been investigated using tensile tests, and also the effect of alloying and strain rate is unknown. **Table 2.1** presents an estimate of the relative ease of activating the 10 relevant slip systems based upon an assessment from the literature data.

The schematic of deformation in these slip systems in the tin crystal structure is illustrated in this table. This table which was developed by Fujiwara and Hirokawa (1987) using the etch-pit / hillock study is not extensive. Other studies by Fiedler and Vagera (1975) to find the relative activity of slip systems are based on the minimum dislocation energy criteria which shows that slip systems #1, #2, and #4 in Table1 are the most active slip systems.

In addition to these two methods, other researchers (Matin et al. (2006) and Sidhu and Chawla (2008)) defined a parameter called "effective yield strength" which is the value of the critical resolved shear stress over the Schmid factor for different slip systems. In this method, the authors used values of critical resolved shear stress for pure tin, which can be different from SAC305 due to the effect of alloying elements. Friedel (1964) and Labusch (1970) showed that the critical resolved shear stress increases with alloying elements. Especially, for some slip systems, there are some assumptions made about the values of the critical resolved shear stress that are based on the linear atomic density, which are not experimentally evaluated.

Kinoshita et al. (2012) recently used the first-principles density functional theory to study the activity of slip systems in pure tin. They used the ideal shear resistance as the values of critical resolved shear stress. They employed a computational tensile test study to assess the activity of different slip systems and investigated the effect of crystal orientation on relative activity of slip systems. Zhou et al. (2009) used a methodology based on the Orientation Imaging Microscopy (OIM), and calculated the Schmid factor together with partial observation of slip traces to assess the activity of slip systems on shear deformed samples. Their study implies that slip in [001] and [111] directions is likely, and slip on (010)[101] may contribute significantly.

9

2.1.3 Microstructural considerations

Crystal features such as grain size and morphology have significant effects on mechanical properties and the reliability of sub-mm scale joints. Studies about the microstructure and Sn grain morphologies in lead free solder joints show peculiar microstructures, such as the beach-ball morphology, in which 60° cyclic twins are formed during the solidification (Lehman et al. 2004, 2010). **Figure 2.6** illustrates two solder joints after thermal cycling (Bieler et al. 2008)). A shear band of different orientation is developed in the middle of the left sample, and a bulge is developed in the right sample along the upper edge of the grain boundary, which illustrates heterogeneous deformation in two types of joint morphologies.

In a series of recent studies on the most commonly used lead-free solder joint, SAC305 (Sn-3.0Ag-0.5Cu, wt%), microstructural issues were examined using polarized light image microscopy, and orientation imaging microscopy (OIM), which showed that most joints are single crystals or multicrystals with no more than a few Sn grain orientations (Bieler et al. 2009, 2012, 2011). Using transmission synchrotron x-ray diffraction patterns, this idea was proven by observing that there are usually one or three orientations present in diffraction patterns (Bieler et al. 2009). Alloying affects nucleation of Sn, leading to formation of single crystal or tri-crystals depending on the concentration of Cu and Ag at the point of solidification (Matin et al. 2005, Lehman et al. 2004). In multicrystals, there is usually a solidification twin relationship with about 55 to 65 degree rotations about a common [100] axis (**Figure 2.6**).
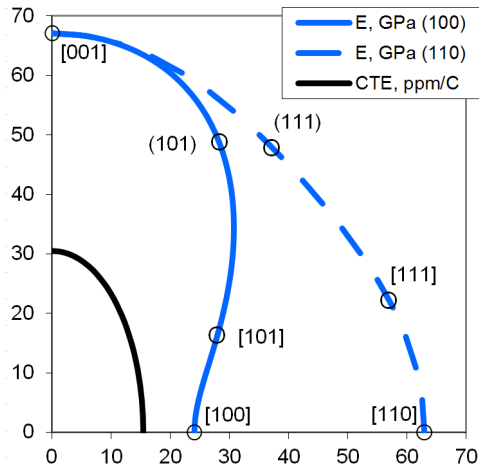
Figure 2.1 Variation of Young's modulus on the (100) plane (solid line) and (110) plane (dashed line), compared with CTE (units are in legend).
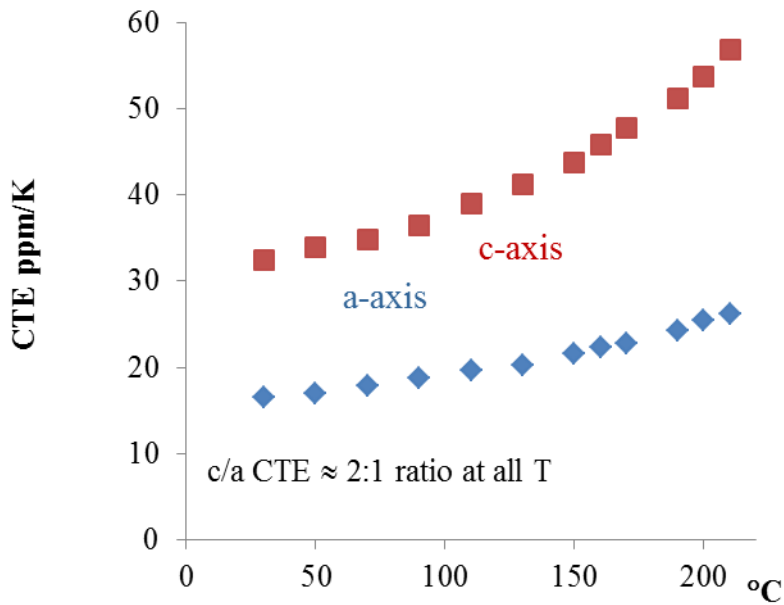
Figure 2. 2 Variation of CTE along the (100) direction and plane and (001) direction (Bieler et al. (2012)).
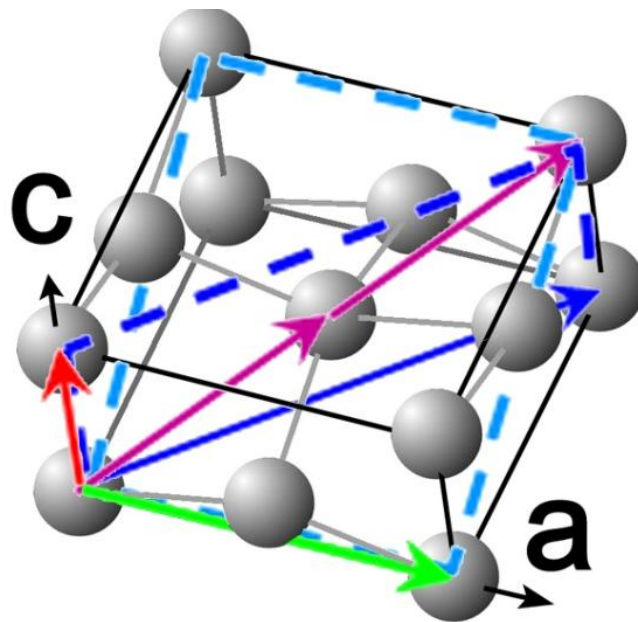
Figure 2.3 Tin unit cell (c/a = 0.5456) (Bieler et al. (2012)).

CTE: ~15ppm/K

CTE: ~30.5 ppm /K   CTE: ~15.4ppm/K
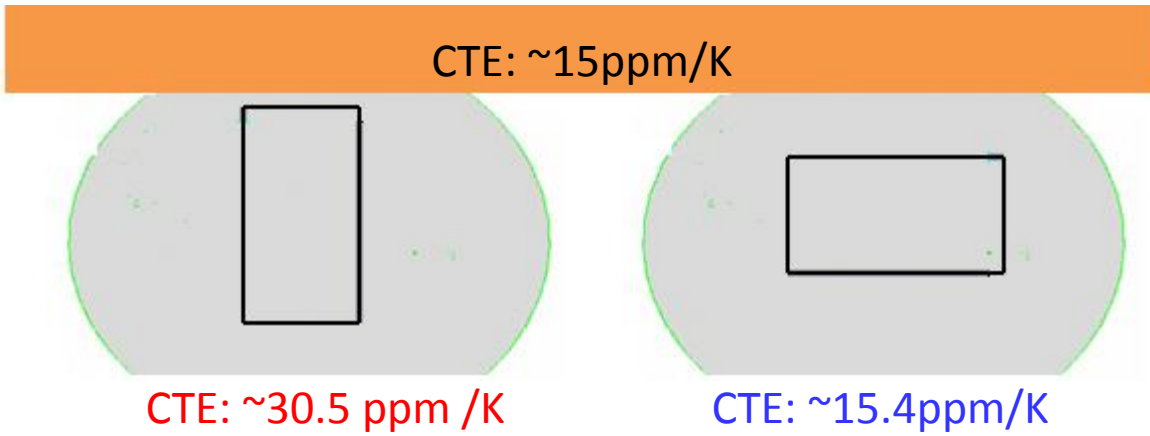
Figure 2.4 Schematic representation of difference between CTE in the interface plane for (a) c-axis parallel to the interface (b) a-axis is parallel to the interface

Table 2.1 Commonly observed Sn slip systems and schematic of slip systems
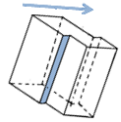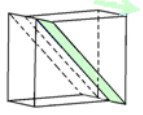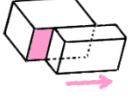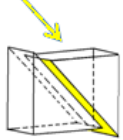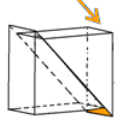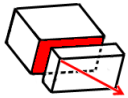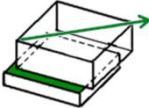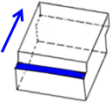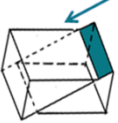
Slip system	Characterization method	Crystal structure	References
Mode 1 {100)<001]	Etch hillock, Energy calculations, Plane trace		Barret, Fujiwara, Obinata and Schmid, Fiedler and Lang, Fiedler and Vagera, Honda
Mode 2 {110)<001]	TEM, energy calculations		Barret, Fujiwara, Chu and Li, , Tyte,Mark and polany Sidhu and Chawla, Matin, Obinata and Schmid , Fiedler and Lang Fiedler and Vagera Honda, Vook
Mode 3 {100)<010]	Plane trace, Energy calculations		Fujiwara, Duzgun ,Ojima, Bausch, Chu and Li, Weertman and Breen, Ojima and Hirokawa, Düzgün et al, Düzgün and Aytaş , Nagasaka , Honda,
Mode 4 {110)<1-11]/2	Energy calculation Etch hillock Plane trace		Barret, Fujiwara, Chu and Li Weertman and Breen , Honda et al., Matin et al., Nagasaka et al., Fiedler and Lang, Fiedler and Vagera, Honda, Zhou et al.
Mode 5 {110)<1-10]	Energy calculation		Weertman and Breen

Table 2.1 (cont'd)

Slip system	Characterization method	Crystal structure	References
Mode 6 {100)<011]	TEM, Plane trace		Vook, Düzgün et al. , Düzgün and Aytaş , Fujiwara and Hirokawa, Nagasaka et al. Fiedler and Vagera, Zhou et al.
Mode 7 {001)<010]	Energy calculations, Plane trace		Schmid, Telang et al. , Fiedler and Vagera, Honda
Mode 8 {001)<110]	Plane trace		Schmid, Telang et al. ,Aytas
Mode 9 {011)<01-1]	TEM, Energy calculations		Barret, , Vook, Sidhu and Chawla, Obinata and Schmid, Fiedler and Vagera , Düzgün and Aytaş
Mode 10 {211)<01-1]	Plane trace		Düzgün et al. (1999), Sidhu and Chawla , Matin et al., Fiedler and Vagera , Düzgün and Aytaş , Zhou
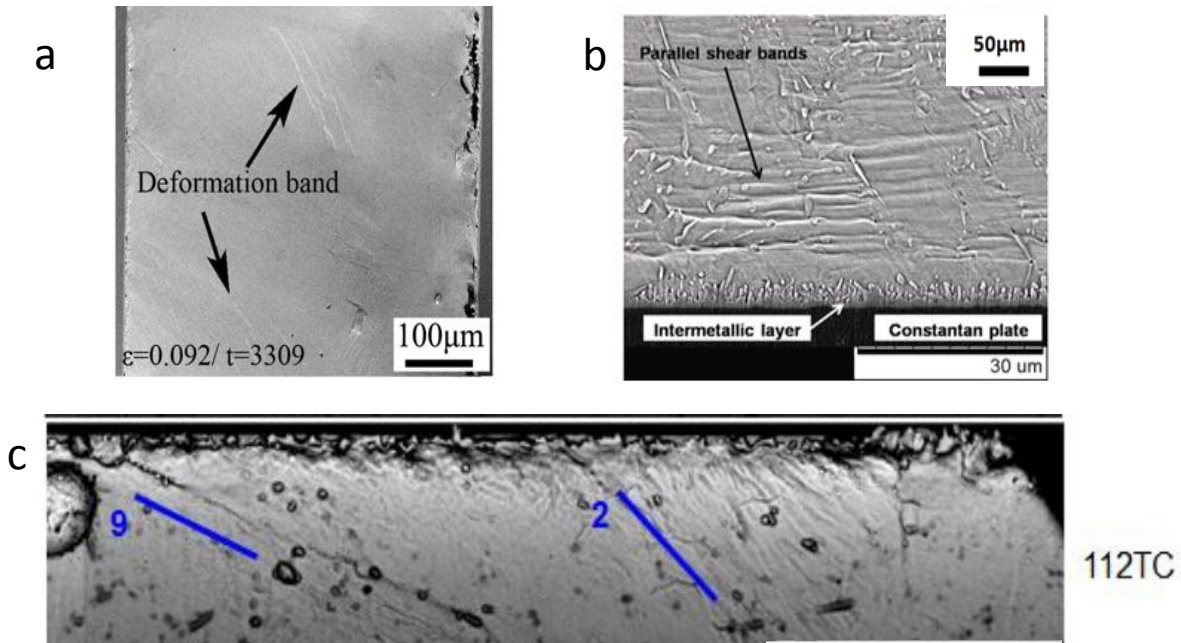
Figure 2.5 (a) Optical micrograph showing the slip trace for a sample that was subjected to creep at 48 MPa (Zhang (2012)) and,(b) BE image of slip traces after 1×10^3/s constant-rate creep test at 50°C to shear strain equals to 0.38 (Hertmeyer et al. (2009)) (c) Magnified micrograph showing slip traces were developed after 112Thermal cycling)) (Zhou et al.(2012))

2.1.4 Importance of slip in SAC 305 alloys

Due to the complexity of the problem arising from the high homologous temperature of tin, anisotropy, and the complexity of loading conditions in real electronic assembly products, it is very difficult to develop a reliable model that takes into account many considerations. Below is a list of important considerations that affect the complex interaction between material properties and loading conditions in real electronic products.

1- Mismatch in the coefficient of thermal expansion along with the high homologous temperature of tin causes the room temperature to be a 'hot' deformation temperature.

Residual stresses caused by this mismatch can produce creep phenomena.

2- Change in the ambient temperature, shutting down, and turning the circuit on and off can produce thermo-mechanical fatigue and recrystallization.

3- The anisotropy in the coefficient of thermal expansion, and elastic properties of tin (that has body centered tetragonal crystal structure), cause the deformation to be quite inhomogeneous.

4- In fact, slip in different slip systems, dislocation climb, sub-grain boundary formation, grain boundary sliding, and grain boundary migration and recrystallization may happen as the result of creep, fatigue, and inhomogeneous deformation.
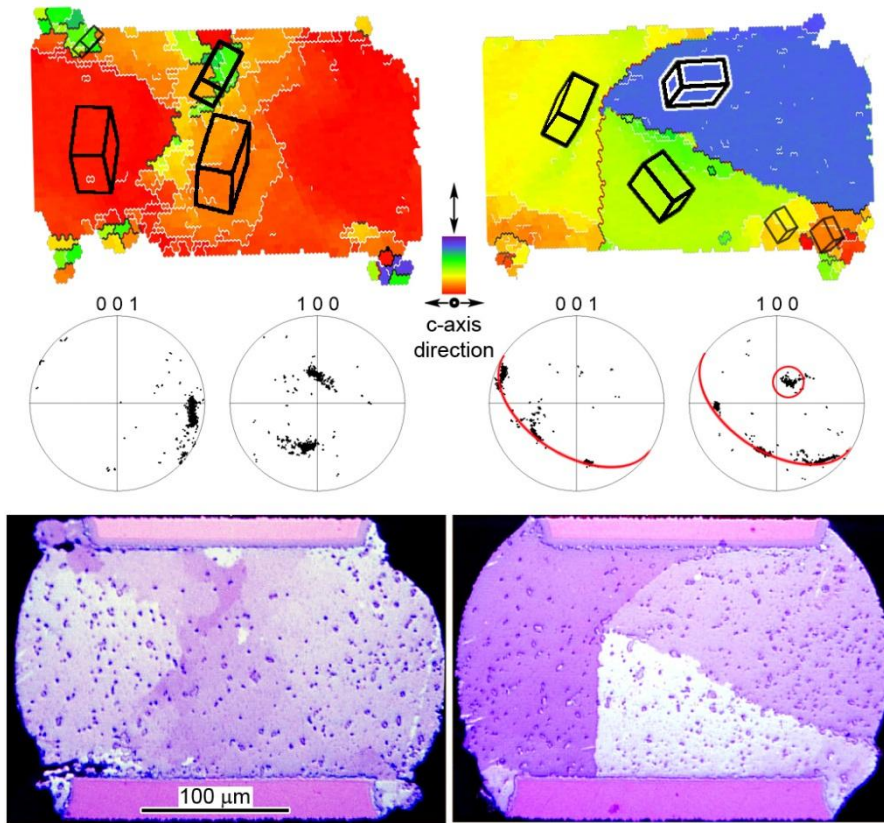
Figure 2.6 Polarized light image and corresponding c-axis orientation maps and pole figures showing a thermo-mechanically cycled single crystal (left), and a tri-crystal showing the 60° about [100] axis twin relationship in SAC305 solder joint (right) . In the single crystal, the white lines delineate low-angle boundaries, and orientation gradients are apparent in the spread peaks on pole figures (Bieler et al. (2008))..

18

Hertmeyer et al. (2009) employed an in-situ optical creep observation of joint-scale SAC 305 alloy shear samples, and observed that dislocation slip can have a large role in the deformation mechanism in SAC 305 alloy at various stress values and temperatures. Zhou et al. (2012) conducted a study under different stress states and showed that the slip phenomena is extremely important in inhomogeneous deformation of particular grains, as well as in developing new grains through gradual lattice rotation during the continuous recrystallization process. Zhang (2012) utilized in-situ tensile creep and electron backscatter diffraction to understand the mechanism of deformation and grain rotation in Sn–4Ag/Cu solder joints during the creep deformation. He observed slip traces on the deformed surface during the primary creep process. Figure 1.5 shows the slip traces that can be observed in different loading condition and temperetures.These studies clearly show that dislocation slip can have a crucial role in thermo-mechanical cycling and creep, and developing a model based on slip mechanism that can define a desirable framework to define a path for further improvement in modeling is necessary.

In reality, due to the large variation in CTE, internal strains arising from both extrinsic (package–board) and intrinsic (anisotropic) CTE mismatches lead to strains on the order of 0.1% or more during the temperature change arising from thermal cycling. However, during the accelerated thermal cycling condition ($\dot{\varepsilon} = 10^{-4}/s$), which is common in the industry, plastic deformation can occur and knowledge about the mechanisms of plastic deformation is important in this regard.

2.1.5 Effect of aging on the mechanical properties of SAC 305 solders

One important aspect of Sn-based solders that has important impact on mechanical properties and stability of the microstructure during service is the presence of intermetallic compounds (IMC). Depending on the composition of minor elements, lead free Sn based solder can contain different IMCs. Generally SAC305 contains Ag_3Sn and Cu_6Sn_5. There are many studies about the role of intermetallics in strengthening the solder matrix. Lee and Subramanian (2005) investigated the impact of Cu_6Sn_5 on the microstructural evolution of Sn based solders. They pointed out that this IMC can pin the Sn grain boundaries.

Kerr and Chawla (2004) examined the influence of micron size Ag_3Sn on the mechanical behavior of Sn based solders and concluded that these IMCs can act as obstacles to reduce the dislocation motion. One important practical aspect of IMCs is that the coarsening of these compounds can degrade mechanical properties of the solder during service conditions.

Due to the anisotropy present in lead free solder balls, which arises from inhomogeneity associated with the crystal structure of tin and large grain microstructures of tin, the macroscopic mechanical response is highly sensitive to the microstructure and geometrical constraints. It should be emphasized that realistic models that can assist in the prediction of the failure location in electronic packages have to consider the unique nature of the stress and strain evolution. This unique stress and strain history is due to the irregular deformation arising from both large grain microstructure of tin and presence of 32 slip systems in the crystal structure of this metal.

Due to the fact that the dimension of a solder BGA ball in the real application is on the order of grain sizes, it is important to examine the mechanical behavior and correlate mechanical

20

properties and the microstructure at the solder ball scale. Therefore information that can be obtained from the bulk material is not necessarily helpful for these applications.

In these size scales, less constrained surface grains deform more easily, and their behavior could be totally different from grains in the bulk materials. Furthermore, a higher cooling rate in the microscale samples leads to different dendritic structure, and creation of different IMC morphologies. Hence, the mechanical response of solder joints to external loading can be different from the bulk solders due to fine microstructure, free surfaces, grain orientation (single grain/ multigrain), and the presence of intermetallic compounds at joint boundaries.

On the other hand, using the assembly level BGA packages as test specimens is not helpful in this regard. The mechanical response which can be obtained using these samples represents the average behavior of an array of many, and is very difficult to correlate the microstructure and mechanical properties in this condition. However, one can still obtain some ideas about the kinematic of deformation and activity of different slip systems using this test configuration.

In addition to the anisotropy, isothermal aging is another parameter that has significant impact on mechanical properties of lead free solder joints during service conditions. This mechanism can reduce the strength and degrade the reliability of solder joints. This issue was examined by several researchers:

Coyle, et al. (2000) reported 20% reduction in shear strength of BGA solder joints after 240 hours of aging at room temperature.

Ding, et al. (2007) studied the effect of aging on fracture behavior of Sn-Ag solder using tensile tests. They showed that the tensile strength is reduces dramatically after aging at 180 ºC for 120 hours.

Ma, et al. (2006) investigated the effect of different aging conditions on Young's modulus, yield strength, and ultimate tensile strength of SAC305 and SAC405 solder alloys. They showed that the strength decreased dramatically in the first 20 days for both room temperature and elevated temperature aging. After 20 days of aging, the properties changed slowly.

Zhang, et al. (2008) also studied the aging effects on tensile properties of SACN05 (SAC105, SAC205, SAC305 and SAC405) series solders for different amounts of aging at temperatures between 25-125 ºC. They demonstrated that the mechanical properties degraded more dramatically when the aging temperature was increased. The data also showed that the degradation becomes linear with longer aging time.

Cai, et al. (2010) also indicated that aging effects are significant for lead free solders for room temperature aging as well as elevated temperature aging. They have also shown that the aging effects can be reduced by using certain dopants (e.g. Bi, In, Ni, La, Mg, Mn, Ce, Co, Ti, Zn, etc.) to SAC solder alloys to enhance the reliability of lead free solders.

Isothermal aging effects have also been reported to lower the strength and to reduce the reliability of solder joints. Li, et al. (2002) studied the elevated temperature aging effects on flip-chip packages with SAC solders. They suggested that the shear strength of solder bumps subjected to aging at 80ºC can decrease gradually with aging. Also, for aging temperatures of 150 ºC and 175 ºC, the degradation of shear strength of the bumps were much faster.

22

Darveaux (2005) indicated that after 24 hours of aging at 125 °C, all alloys showed a 10% to 30% reduction in solder joint strength. All solder joints failed within the bulk solder and exhibited high ductility. In addition, the ductility of all Pb-free solder joints decreased with increased aging.

Chen, et al. (2006) studied the effects of aging on the solder bump shear strength for both Sn-Pb and Sn-3.5Ag solders. They reported that the shear strength for both solder materials decreases after aging at 150 ℃ for 1500 hours, 8.9% for Sn-Pb solder bumps, and 5.3% for Sn-3.5Ag.

Kim, et al. (2004) obtained similar results in which they reported 5% decrease in the strength of joints in stud bump samples for aging at 150 ℃ for 300 hours.

Lee et al. (2010), indicated that aging degrades the Thermal Cycling Reliability (TCR) of lead free PBGA assemblies subjected to Accelerated Life Testing (ALT) for SAC305 samples, which were subjected to aging at elevated temperature aging (100-150 ℃). Lee, et al. (2012) showed that the lifetime of wafer-level chip scale packages with SAC305 solder interconnects was reduced by 29% for 500 hours of aging at 150 ℃.

Zhang, et al. (2012) studied the effects of aging on the reliability of PBGA components. They showed that for 6 months aging at 125 ℃ the reliability of SAC105 components dropped by 53%.

In summary, the main reason for softening effect after aging is that when the particles are small they can pin the dislocation movement and can act as strengthening mechanisms, however when they grow coarser their strengthening ability is reduced dramatically.

2-2- Characterization techniques

To assess the evolution of Sn crystal orientation during monotonic loading (shear and tension), different characterization techniques were employed in this study.

2.2.1 Polarized Light Microscopy (PLM)

Polarized light microscopy is an optical contrast-enhancing technique that uses **birefringent** (or doubly-refracting) property of non-cubic materials. A polarization filter is introduced into the beam of light before it passes the sample, and a second polarization filter, the analyzer, is put into the beam of light after it passes. In order to be able to conduct the characterization, polarizer and analyzer have to be oriented perpendicular to each other. Anisotropy in the **birefringent** (or doubly-refracting) property of the sample causes bending in some of the plane polarized light, so that it can pass through the analyzer and can be imaged. The amount of the light, which passes the analyzer is dependent on the orientation of the anisotropic structures in the sample in relation to the rotation angle (azimuth) of the polars. By rotating the stage, one can change the relative orientation of near cross-polarized light with respect to the sample and take advantage of birefringent property of tin and distinguish the contrast (Lee et al. (2009)).

Application of this method for characterization of tin has been proved by several prior studies [Bieler et al. (2008), Seo et al. (2009), Seo et al. (2010), Telang et al. (2004), Elmer et al. (2010), Lehman et al. (2004, 2010), Lee et al. (2009), Mattila et al. (2010), Yin et al. (2012), Sundelin et al. (2008), Henderson et al. (2004), Chen et al. (2011), Bieler et al. (2011), and Mattila and Paulasto-Krckel (2011)].

One of the most important applications of PLM in lead free solder joints is discovering the cyclic-twin grain structure (also known as Kara's beachball) in a SAC alloy solder which is

shown in Figure 1.8). Although this method is a useful qualitative method to identify the crystal structure and different grain structures, it does not provide any quantitative information about crystal structures. Therefore, other techniques such as electron backscatter diffraction (EBSD) or X-ray diffraction (XRD) are required to be able to quantitatively identify grain orientations. These methods will be described later.
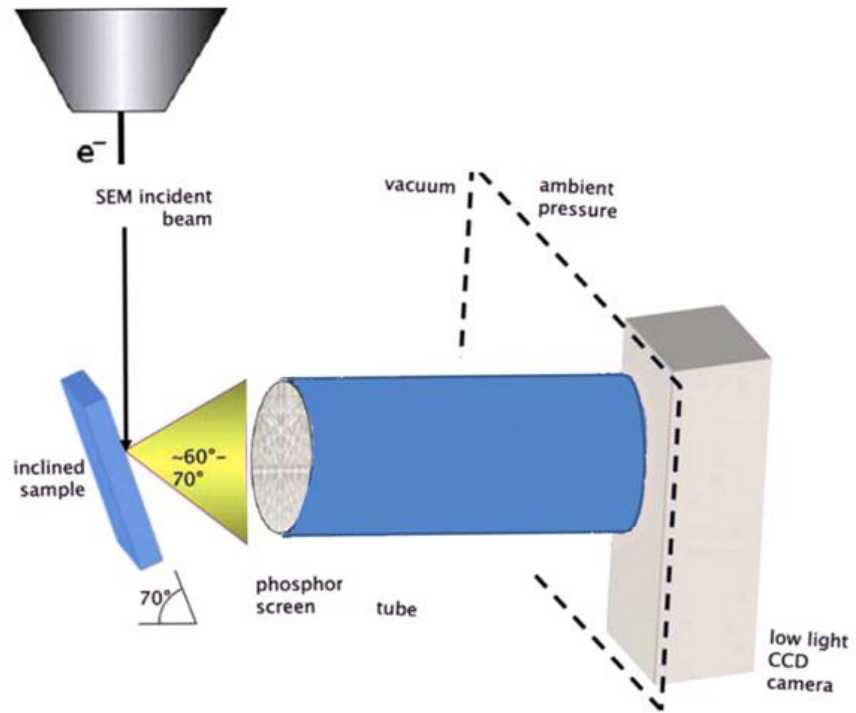
Figure 2.7 Schematic diagrams showing the experimental set up for EBSD observation.
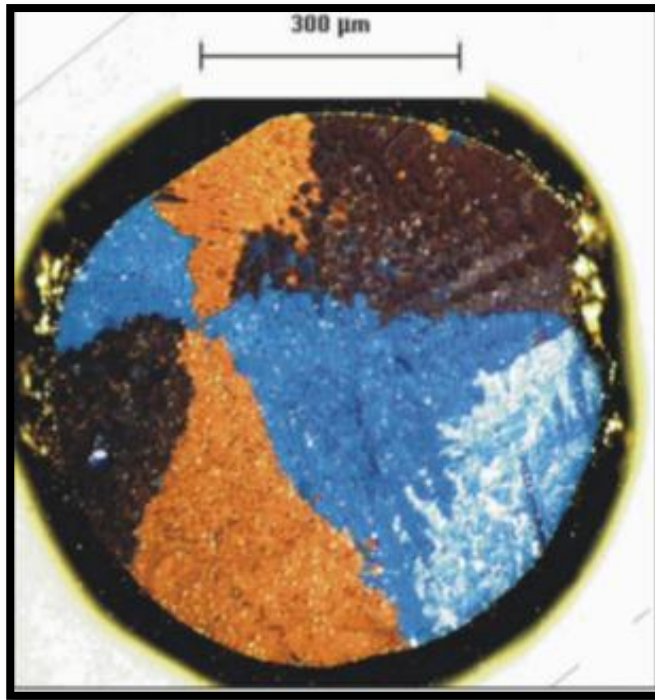
Figure 2.8 Polarized light image showing the application of this method in characterization of grains morphology in lead free solder balls (adapted from Lehman et al. (2010)).

2.2.2 - EBSD and polarized light microscopy

Electron backscatter diffraction (EBSD) is a technique used to examine the crystallographic orientation of crystalline materials. This technique is conducted using a Scanning Electron Microscope (SEM) equipped with an EBSD detector containing a phosphor screen, compact lens and low light CCD camera chip.

For an EBSD measurement, a polished crystalline sample is mounted inside the SEM chamber at a highly tilted angle (~60-70° from horizontal) towards the diffraction camera to increase the contrast in the electron backscatter diffraction pattern. The phosphor screen is located inside the chamber of the SEM at an angle off by approximately 90° from the pole piece, and is coupled to a compact lens which focuses the image from the phosphor screen onto the CCD camera. This configuration is schematically shown in **Figure 2.7**.

In this configuration, some of the electrons which enter the sample will backscatter and exit at the Bragg condition (For a crystalline solid, the waves are scattered from lattice planes separated by the distance *d*). The Bragg condition describes the constructive interference from successive crystallographic planes as:

$$2d sin\theta = n\lambda$$

where n is an integer determined by the order given, λ is the wavelength, d is lattice plane distance, and θ is the scattering angle. Some of these diffracted electrons collide and excite the phosphor causing it to fluoresce. Different crystalline planes diffract different electrons and form a pattern consisting of pairs of white and dark parallel lines known as Kikuchi bands. Each band can be indexed individually, but most commercial systems use look up tables with crystal

data bases to perform indexing. An automatic indexing of these patterns known as Orientation Image Microscopy (OIM) is utilized to obtain a complete description of the crystallographic orientations in polycrystalline materials.

2.2.3 Differential Aperture X-ray Microscopy (DAXM)

Although the EBSD is very helpful and popular in probing the grain orientation, obtaining 3D information using this method is only possible when this tool is combined with the destructive procedures such as serial sectioning or milling with a focused ion beam (FIB). 3D-xray is one of few tools that can probe local grain structure nondestructively.

In the DAXM methods, a pair of elliptical total external reflection Kirkpatrick-Baez (K-B) mirrors focuses a polychromatic x-ray beam to a 0.5 µm×0.5 µm spot on the sample. The sample is mounted on a stage, with the sample normal making an angle of 45° with the incoming x-ray beam. A schematic of the experimental setup is shown in **Figure 2.9**. A charged-coupled device (CCD) detector located above the sample records Laue diffraction patterns generated by volume elements along the x-ray beams. A differential aperture made of a 50 µm platinum wire scans across the surface of the sample and decode the overlapping beams by subtraction of CCD image pairs, which differ only by a small (differential) motion.

A computer program developed at Oak Ridge National Lab determines the positions of Laue diffraction spots in the CCD camera images, indexs the patterns, and calculates the orientation matrix for each 1 µm voxel from which a discernible diffraction pattern could be decoded.

The program first makes a list of possible indices (hkl) for each reflection from the known band pass of the radiation, the known unstrained unit cell parameters, and the angle of reflection. The

29

measured angles between reflections are compared to the angles calculated for an unstrained grain with all possible indices. If the angles are within the expected experimental and strain uncertainty, the indices are assigned to the same grain. These computational procedures are performed using powerful computer servers equipped with multiple processers.
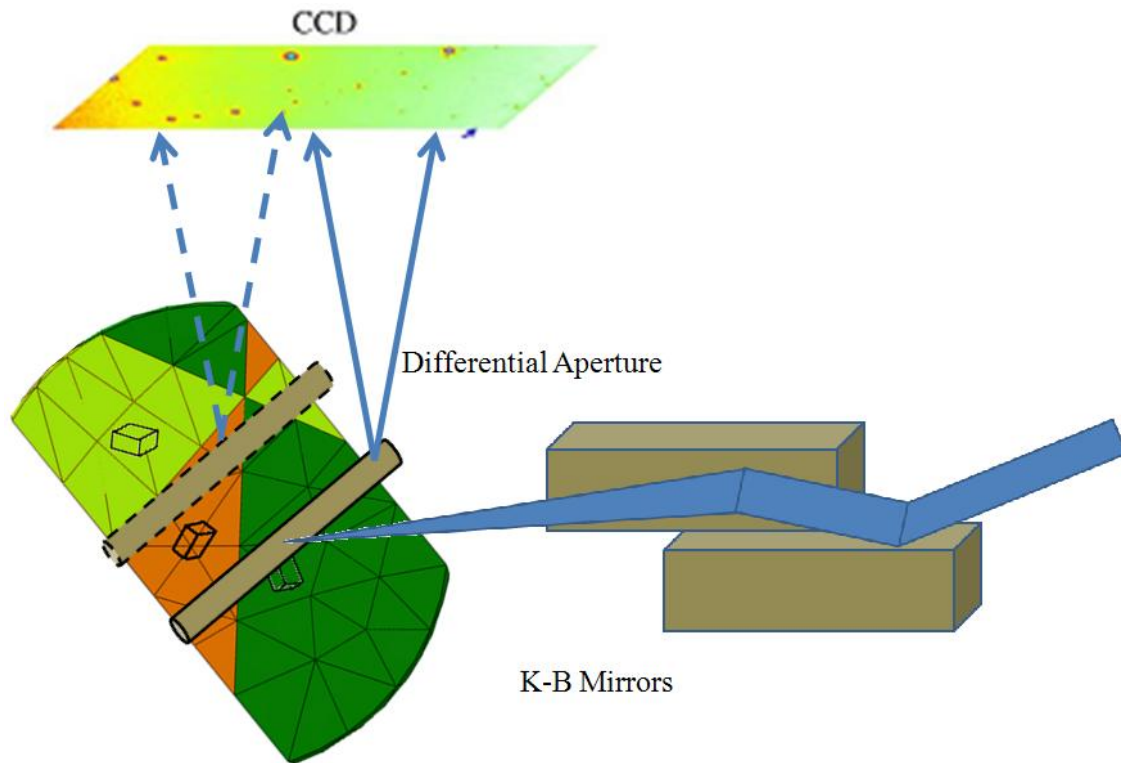
Figure 2.9 Schematic diagram showing the experimental set up for DAXM observation. The incident X-ray beam can have either a polychromatic or monochromatic spectra. A 50 m m-diameter platinum wire is translated near the sample surface to decode the origin of the overlapping Laue patterns.

2.2.4 2-D Radiography

The 2-D radiography which is based on the x-rays shadow microscopy was employed in this study to assess the effect of voids in solder balls on mechanical properties. This method schematically is illustrated in **Figure 2.10**. This technique is based on the idea that different materials within a sample absorb the x-ray diffraction differently depending on their density and atomic numbers. This phenomenon produces a shadow on the detector such that when the material is denser, the shadow becomes darker. Hence, big voids clearly are characterized as brighter areas. The detector creates optical images from the incident x-rays and allows identifiacation of defects in the sample that are larger than the detector pixel size.
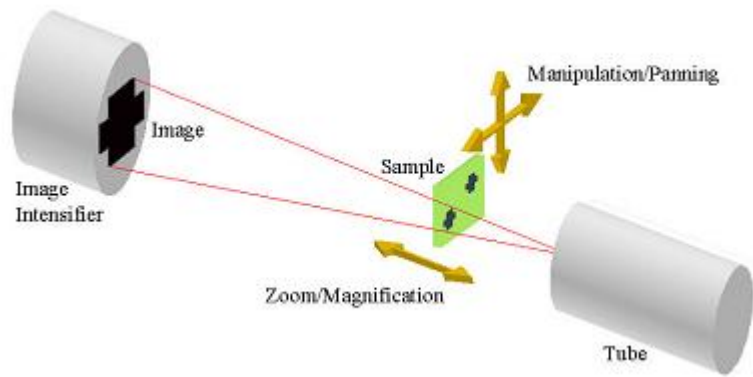
Figure 2.10: Basic 2-D x-ray system configuration (Benard (2003))

2.3 Modeling approaches used in solder joints

There are numerous computational methods that have been utilized to model deformation behavior and damage nucleation in solder alloys. Dong et al. (2005) Gao and et. al (2010) used molecular dynamics simulations to find the atomic scale properties of solders required for multi-scale simulation of damage nucleation and evolution. The disadvantage of this approach is that it is computationally expensive and cannot be used for realistic sample sizes, and these calculations require long periods of time. Due to the fact that dislocation motion is the most significant mechanism in creep (time-dependent) and plasticity (time-independent) deformation, one can develop the same constitutive equation for both creep and plasticity. These types of studies based upon unified creep plasticity (UCP) modeling have been conducted by several researchers.

In the following, some of these models are briefly described. Hart et al. (1976) introduced a model based upon the idea that dislocation pile up occurs in two states, strong (macro plastic) and weak (micro plastic), and one can define a state variable for each case. This model was later employed for solder alloys by Wilcox et al. (1990) ignoring the viscous effect. Although this model was fairly promising in the prediction of several deformation behaviors such as creep, load relaxation, and tensile test, it was quite unsuccessful in predicting the transient behavior such as the Bauschinger effect. Yao and Krempl (1986) proposed a viscoplasticity theory based on overstress (VBO), which was later developed by Tachibana and Krempl (1995, 1997, 1998). This model is essentially based on a viscoplastic flow potential and defines three state variables as overstress (the difference between the actual stress and back stress), kinematic stress for work hardening, and isotropic stress. Maciucescu et al. (1999) employed this model for creep behavior of solder alloys.

Anand (1985) and Brown et al. (1989) developed a model for hot working of metals which was employed for solder joints by Adams (1986), Wilde et al. (2000), Wang et al. (2001), Chen et al. (2005), and Qing et al. (2007). This model is very popular due to using a single scalar state variable to define the deformation resistance. Furthermore, this model is quite successful in describing deformation behaviors such as strain hardening, constant strain rate behavior at different temperatures, steady-state creep, and thermal cycling hysteresis loops. The disadvantages of this model is that the oversimplification arising from defining one state variable makes it very difficult for applications that need more physics based understanding. Busso (1992) introduced a model in which the Bauschinger effect was captured using a back stress. This back stress can be described as an internal stress arising from dislocation pile-ups at barriers. This model was employed for solder deformation by Busso (1992, 1994). McDowell et al. (1994) introduced a thermo-viscoelastic model to simulate the deformation behavior of solder alloys. In their model, the back stress can be written as a summation of short range and long range effects.

A modified, unified creep and plasticity model was developed by Wen et al. (2001, 2002) using a similar framework. Employing different rules of evolution for short-range back stress, in this framework, Bai and Chen (2009) could model uniaxial tensile tests, strain rate jump tests, short term creep tests with stress jumps, and uniaxial ratcheting tests. The governing equations of the last four models are reported in **Tables 2.2.**

Bodner and Partom (1975) presented a set of constitutive equations to describe the elastic-viscoplastic strain-hardening behavior for large deformation and arbitrary loading. They used the additive decomposition to divide the total plastic strain into elastic and inelastic strains. The inelastic strains follow the Prandtl-Reuss flow law, which is independent of any yield criteria or loading and unloading conditions. There are two state variables in this model; one corresponds to isotropic hardening and the other is related to directional hardening. Skipor (1996), Whitelaw et al. (1999), and He et al. (2006) used this model to explain the deformation behavior of different solder alloys. Johnson and Cook (1983) presented a phenomenological model to describe the strain rate- and temperature-dependent response of metals. Fei et al. (2008) used this model to consider the effect of strain rate for lead-free solder joints to simulate the board level drop impact test deformation and damage. Xuming et al. (2011) presented a modified Johnson Cook constitutive equation to model the damage evolution in these alloys.

There are other unified constitutive models that have been introduced for solders. A temperature dependent yield function was developed by Desai et al. (1997). Ju et al. (1996) proposed a scalar function to obtain the inelastic strain rate. Qian and Liu (1997) used the back stress to represent the transient stage of a stress–strain curve in a unified constitutive model for tin–lead solder. In an attempt to measure the mechanical properties for SAC305, a parametric study was conducted by Chawla et al. (2005) to simulate the lap-shear test using a simple isotropic constitutive equation. Recently, Lederer et al. (2012) proposed a constitutive model for plasticity and damage of solder joints. This model shows better agreement with experimental results for ultimate tensile strength of solder joints with various thicknesses.

The models discussed above generally lack anisotropic material behavior, so the sophistication in these formulations are based upon the assumption that there are sufficient numbers of grains that anisotropic behavior can be homogenized. The next set of models are simpler but contain the important anisotropic property considerations.

Matin et.al (2005) used a simple linear elastic constitutive equation to study the role of intrinsic anisotropy of Sn on the thermal fatigue damage in real microstructures and grain orientations. Similar study was conducted by Park et al. (2008). Although Matin's and Park's studies were very important for understanding the effect of real microstructure and grain boundaries in strain localization, they assumed very simple elastic models. In order to examine the solder deformation, one has to understand the evolutions of plastic stress and strain as well as microstructural changes arising from the plastic deformation.

Gong et.al (2007) used the crystal plasticity finite element developed by Huang (1991) and incorporated a visco-plasticity constitutive equation in that model. Although they could realistically simulate the response of a solder joint under thermal-cycling loading condition, they did not incorporate the elastic and thermal expansion anisotropy in this model.

Bieler and Telang (2005, 2009) performed modeling of a shear test using the Visco-Plastic Self-Consistent (VPSC) polycrystal plasticity model developed by Lebensohn and Tomé (1993). Using some assumptions about the activity of slip systems, they were able to achieve excellent agreement with measured texture evolution from an OIM data set.

Zamiri et al. (2009) used an anisotropic elastic-plastic finite element model with phenomenological flow models for slip systems based upon semi quantitative information

available in the literature. Using a set of simulations, they were able to correlate changes in the crystal orientation to the internal elastic energy of the system.

The main limitation of crystal plasticity models that are developed so far (models which were used by Gong, Bieler, and Zamiri) is that they did not validate their model by comparing the stress response with experimental data. Table 2.3 shows a comparison between these models and phenomenological models.

2.3.1 Comparison of the phenomenological basis for different models

The phenomenological basis for most of the proposed models can be explained by Kocks' discussion of the thermodynamics of slip (Kocks 1987). Hart proposed a unified viscoplasticity model based on these principles. He started his derivations based on the existence of barriers to dislocations and suggested the existence of two stresses: one due to the pile-up of these dislocations at barriers and the other due to glide resistance to dislocation movement within barriers. Anand's model also was based on the same physics. He defined averaged isotropic resistance that can represent strengthening mechanisms such as dislocation density, solid solution strengthening, and sub-grains. In the hardening formulation, the effect of static recovery was taken into account. Busso, used a single state variable that is derived from the physical basis of dislocation pile-ups at barriers that create a back stress. The Krempl and McDowell models clearly differ from the other three models. The main difference is that they define the viscoplastic flow potentials and a lack of thermodynamic activation energy associated with the plastic strain rate. Bower and Wininger (2004) proposed a two dimensional FE model that could simulate the constitutive response and microstructure evolution of polycrystals during high temperature plastic deformation. Their model takes into account the effects of grain boundary

38

sliding, grain boundary diffusion, grain boundary migration, surface diffusion, as well as thermally activated dislocation creep within the grains.

The ability to relate the microstructure to the macroscopic mechanical properties is important from the materials design point of view, and crystal plasticity assists in conducting the microstructure sensitive design for crystalline materials. The mechanical modeling of single crystal behavior is well established (Taylor and Elam, (1923), Asaro (1983), Hill and Rice (1972), Mandel, (1965)). However, the efficiency of numerical modeling is still a controversial subject especially when these algorithms are used as tools to design industrial products using FEM codes. In this context, development of numerical integration algorithms with improved efficiency, speed and accuracy is of great importance.

Regarding the numerical algorithms behind the crystal plasticity, two issues are important. The first one is how to integrate the set of highly non-linear constitutive equations and the second one is how to resolve the ambiguity arising from non-uniqueness in the activity of slip systems.

In order to solve this set of non-linear equations, several incrementally based numerical algorithms have been proposed. These numerical schemes can be classified into three main families: explicit algorithms based on a forward Euler scheme, implicit algorithms based on a backward Euler scheme, and semi-implicit algorithms.

2.3.2 -Explicit integration algorithms:

Developing explicit algorithms is straightforward, but it generally requires very small times or loading increments to avoid numerical instabilities. This numerical scheme was employed by Nemat-Nasser and Amirkhizi,(2007), Anand and Kothari (1996), Ben Bettaieb (2006),

39

Knockaert et al. (2000), Kuchnicki et al. (2006), Maniatty et al. (1992), Mathur and Dawson (1989), Peirce et al.(1982), Zamiri et al. (2007), Zamiri and Pourboghrat (2010), and Rossiter et al. (2010). The critical resolved shear stresses and the crystal rotation are assumed to be constant over the time increment and chosen to be equal to their values at the beginning of the time step.

2.3.1 -Implicit integration algorithms:

The implementation of implicit schemes is more complicated than for explicit ones. In the implicit family, critical shear stresses and the rotation of the crystal lattice are unknown, producing a set of nonlinear equations. This set has to be solved by traditional iterative methods (generally those such as the Newton–Raphson procedure or the fixed point method). Kalidindi et al. (1992) used this method of solving crystal plasticity finite element simultions.

2.3.3 -Semi-implicit integration algorithms:

In this class of numerical schemes, the crystal lattice rotation is evaluated at the beginning of the time increment, whereas, the computation of critical resolved shear stresses is based on an implicit scheme. McGinty and McDowell (2006) and Watanabe et al. (2010) employed the iterative resolution of the consistency conditions to solve the non-linear constitutive equations. Débordes et al. (2005) incorporated the linearization of the hardening law over each time step into semi-implicit scheme.

The second difficulty in numerical algorithms is related to the non-uniqueness of active slip systems. Several researchers tried to solve this problem using two distinct procedures. The first method that is based on the thermodynamic motivation was first proposed by Taylor (1923). One of the fundamental assumptions of the Taylor theory is that among the many possible slip

combinations that can achieve the prescribed crystallographic strain, the combination that produces the minimum amount of internal work is the set that is activated (Taylor and Elam (1923)).

Renouard and Wintenberger (1981), Van Houtte (1988), and recently Hamelin et al. (2011) developed a first order selection criterion, based on the minimization of the change in the internal work with respect to von-Mises strain. Driver et al. (1984), Fortunier and Driver (1987) and Skalli et al. (1985) examined this method for aluminum single crystals.

Franciosi and Zaoui (1991) used a criterion based upon the minimization of the hardening in order to select the set of active slip systems.

Raabe et. al (2001) implemented a local Taylor factor schemes using the local stress tensor to determine the local Taylor factor, to better track heterogeneous deformation evolution, and this matched experiments better than using a global Taylor factor approach.

On the other hand, several researchers tried to use a rate-dependent formulation based on power-type laws without differentiation of slip systems into active and inactive sets (Asaro and Needleman, (1985), Mathur and Dawson, (1989), Peirce et al. (1982, 1983)). This method has attracted attention since the empirical equations can be easily incorporated in this framework using formulations that define the relationship between the dislocation density, velocity, and shear strain rate.

Anand and Kothari (1996) and Knockaert et al. (2000), employed the well-known singular value decomposition (SDV) method (which projects the deformation rate on the set of positive slip rates. Schröder and Miehe (1997) and Miehe and Schröder (2001) proposed an alternative general inverse method where the reduced space is obtained by dropping columns of the local

Jacobian associated with zero diagonal elements within a standard factorization procedure. All these models attempt to use the Schmid law and define multi-surface yield functions.

Many other authors (Gambin (1991, 1992), Montheillet et al. (1985), Toth et al. (1991), Van Houtte (1987), Guan et al.(2007), Zamiri et al. (2007)) proposed robust schemes based upon defining smooth yield surfaces to solve the ambiguity in defining the active slip systems. The derivative of this yield function with respect to the shear stress can define the strain rate. Recently, Zamiri and Pourboghrat (2010) developed an effective methodology to define a smooth yield function based on the logarithms of the Schmid law for all slip systems and incorporating a regulation parameter which will be described later.

Table 2.2 Summary of the main phenomenological equations used in solder joints

Original Model --Application to Solder	Forms of Important Constitutive Relations	Definition of variables
1. Hart (1976) -- Wilcox et. al. (1990)	$\ln(\dfrac{s_1}{\sigma_{a1}}) = (\dfrac{\varepsilon_1}{\dot{\alpha}_1})^{\lambda_1}$ $\dot{\varepsilon}^*_1 = (\dfrac{s_1}{G})^{m_1} f_1 \exp(-\dfrac{Q}{RT})$ $d\ln(s_1)/dt = h(\sigma_{a1}, s_1)\dot{\alpha} - r(s_1, T)$ $h = (\dfrac{\sigma_{a1}}{s_1})^{\frac{\beta}{s_1}} (\dfrac{\beta}{s_1})^{\delta}$ $s_2 = \sigma_{a2} e^{-C\sigma_{a2}}$	$\lambda_1, f_1, Q, \beta, \delta, C : Materials\ parameters$ $R : Boltzmann's\ constant$ $s_1, s_1, h : hardening\ variable$ $r : recovery\ variable$ $\alpha_1, s_1 : macro\ strain\ and\ hardening$ $\alpha_2, s_2 : micro\ strain\ and\ hardening$
2. Anand (1982) --Adams (1986), --Wilde et al. (2000), --Wang et al. (2001)	$\sigma = cS$ $c = \dfrac{1}{\zeta} \sinh^{-1}[\dfrac{\varepsilon^p}{A} \exp(\dfrac{Q}{RT})^m]$ $\dot{\varepsilon}^p = A\exp(-\dfrac{Q}{RT})\sinh(\xi\dfrac{\sigma}{s})^{\frac{1}{m}}$ $\dot{s} = h(\sigma, s, T)\dot{\varepsilon}^p - \dot{r}(s, T)$ $\dot{s} = h_0 \left|1 - \dfrac{s}{s^*}\right|^a sign(1 - \dfrac{s}{s^*})\dot{\varepsilon}^p$ $s^* = s[\dfrac{\dot{\varepsilon}^p}{A} \exp(\dfrac{Q}{RT})]^n$	$\xi, Q, A, m : Materials\ parameters$ $R : Boltzmann's\ constant$ $s : hardening\ variable$ $r : recovery\ variable$ $s^* : saturated hardening\ variable$

43

Table 2.2 (cont'd)

Original Model --Application to Solder	Forms of Important Constitutive Relations	Definition of variables
3. Krempl(1985) --Maciucescu et al. (1999)	$x = \sigma - B$ $\Phi = \left(\dfrac{g}{m+1}\right)\left(\dfrac{\bar{x}}{\bar{\sigma}}\right)^m \dfrac{x}{\bar{x}}$ $\bar{x} = \sqrt{(3/2)tr(x.x)}$ $\dot{\varepsilon}^p = \dfrac{3}{2} g(\dfrac{\bar{x}}{\bar{\sigma}})^m \left(\dfrac{x}{\bar{x}}\right)$ $\dot{B} = \Psi\dot{\theta}\sigma + \Psi\dot{\sigma} + E\Psi\dot{p}(\dfrac{x}{\bar{x}} - \dfrac{B-f}{A})$ $\dot{f} = \dfrac{2}{3} E_t \dot{\varepsilon}^p = E_t \dot{p} \dfrac{x}{\bar{x}}$ $\dot{A} = -\beta(\dfrac{A-A_2}{A_2})$ $\dot{p} = \sqrt{(2/3)tr(\dot{\varepsilon}^p.\dot{\varepsilon}^p)}$	$E, E_t, m, \bar{\sigma}, \beta, : Materials$ parameters $g :$ Equilibrium stress $B : Backstress$ $f : Kinematic$ stress $A : Isotropic$ stress $A_2 :$ Initial isotropic stress $\Psi :$ dimensionless shape constant

44

Table 2.2 (cont'd)

Original Model --Application to Solder	Forms of Important Constitutive Relations	Definition of variables
4. McDowell(1994) --Bai,Chen (2009)	$\dot{\varepsilon}^{in} = \sqrt{\dfrac{3}{2}} A(\dfrac{\langle S_v \rangle}{D})^n \exp((B\dfrac{\langle S_v \rangle}{D})^{n+1})\theta N$ $S_v = (3/2)^{1/2}\|s-\alpha\| - Y$ $\theta = \exp(\dfrac{-Q}{RT}) \; for \quad T \geq \dfrac{T_m}{2}$ $\theta = \exp(\dfrac{-2Q}{R\,T_m}[\ln(\dfrac{T_m}{2T})+1]) \; for \quad T \leq \dfrac{T_m}{2}$ $N = \dfrac{s-\alpha}{\|s-\alpha\|}$ $\dot{\sigma} = C(T):(D^n - D^{in} - \alpha_k T) + C^{-1}:\sigma:\dfrac{\partial C}{\partial T}\dot{T}$ $\dot{\alpha} = G\|\dot{\varepsilon}^{in}\|N - \beta\alpha$ $Y = Y_{in} + Y_0$	$A,Q,G,B,\beta,Y_0 :$ $Materials$ parameter $S_v :$ over stress $Y : Yield$ stress $\alpha : Backstress$ $R :$ Boltzmann's constant $D :$ Darg stress

Table 2.2 (cont'd)

Original Model --Application to Solder	Forms of Important Constitutive Relations	Definition of variables
5. Huang(1991) --Gong(2007)	$$\dot{\varepsilon} = C_1 sign(C_2\bar{\sigma})^n \exp(\frac{Q}{RT})$$ $$\dot{\varepsilon} = \dot{\varepsilon}_e + \dot{\varepsilon}_c$$ $$\dot{\sigma} = C : \dot{\varepsilon}_e$$ $$\dot{\varepsilon}_c = \sum_{i=1}^{N} \dot{\gamma}.P^\alpha$$ $$P^\alpha = \frac{1}{2}(m^\alpha \otimes n^\alpha + n^\alpha \otimes m^\alpha)$$ $$\dot{\gamma}^\alpha = A_\alpha sign(\tau^\alpha) \exp(\frac{Q}{RT})$$ $$\tau^\alpha = \sigma : P^\alpha$$ $$\dot{\varepsilon} = C_1 sign(C_2\bar{\sigma})^n \exp(\frac{Q}{RT})$$	$C_1, C_2, Q, A, m, C :$ *Materials* parameter R : Boltzmann's constant s : *hardening* var *iable* r : *recovery* var *iable* s^* : *saturatedhardening* var *iable* n^α : Plane normal m^α : Slip direction τ^α : Re *solved* shear stress

46

Table 2.3 Summary of different modeling approaches that employed to model the mechanical behavior of lead free solders

Original Model	Application to Solder	#S.V.*	#M.P.s*	Prediction Capability	Limitations
Hart (1976)	Wilcox (1990)	2	18	Cyclic tests, transient effect	primary creep, Strain rate jump
Anand (1990)	Maleki (2011)	1	9	Strain rate jump, Steady state creep	primary creep
Busso (1992)	Busso (1994)	1	10	Isothermal tests	validated test
Krempl (1986)	Maciucescu (1999)	3	9	Baushinger effect, Fatigue life	validated test
McDowell (1994)	Bai (2009)	2	10	Strain rate jump, Ratcheting test	primary creep
Tome(1993)	Bieler (2009)	1	7	Texture evolution	stress-strain validation
Zamiri (2009)	Zamiri (2009)	1	7	Damage evolution	stress-strain validation
Huang (1991)	Gong (2008)	1	7	Possible multi-scale modeling	validated test

* #S.V.: numbers of state variables, * #M.P.s: number of material parameters

2.4. Summary of the literature review

Anisotropy is of significant importance in all structural metals, but this characteristic is unusually strong in Sn, making Sn based solder joints one of the best examples for studying the influence of anisotropy. This anisotropy is due to the crystal structure of tin and the existence of coarse grain microstructures that are observed in sub-mm solder balls.

Studies about the microstructure and Sn grain morphologies in lead free solder joints show peculiar microstructures, such as the beach-ball morphology, in which 60° cyclic twins can be formed during solidification.

Understanding the slip activity in tin provides valuable insights into the understanding of plastic anisotropy. There is incomplete understanding of slip in Sn, though single crystals have been investigated. There is especially uncertainty about the critical resolved shear stress for different slip systems in SAC alloys.

The majority of previous studies are based on the isotropic plasticity models, which may be useful for polycrystals but for lead-free solder joints that are inherently either single crystal or multi-crystals, using isotropic plasticity models is not physically sufficient.

The purpose of this study is to develop a model to correlate the microstructure to the mechanical properties. Due to significant effect of anisotropy arising from the slip activity combination of CPFE and materials characterization methods was employed to propose a microstructure sensitive material model.

CHAPTER 3

CRYSTAL PLASTICITY MODEL DESCRIPTION

A velocity gradient in plastic deformation in the material coordinate system can be decomposed into a rate of deformation and a spin tensor as :

$$L^{\mathrm{P}} = D^{\mathrm{P}} + W^{\mathrm{P}} \tag{5.1}$$

An elasto-plastic problem is usually defined as a constrained optimization problem aimed at finding the optimum stress tensor and internal variables for a given strain increment. In such a problem, the objective function is defined based on the principle of maximum dissipation and is made of terms describing the incremental release of elastic strain energy and the dissipation due to the incremental plastic work and the constraint is the yield function

$$\left(\sigma_{j+1}, q_{j+1}\right) = \begin{cases} \mathrm{Min}[l(x) = \left(\sigma_{j+1}^{\mathrm{trial}} - \Sigma\right) : C^{-1} : \left(\sigma_{j+1}^{\mathrm{trial}} - \Sigma\right) + \left(q - q_{\mathrm{j}}\right) : E^{-1} : \left(q - q_{\mathrm{j}}\right)] \\ \qquad\qquad\qquad \text{Subjected to} : f(\Sigma, q) \leq 0 \end{cases}$$

$$\tag{5.2}$$

where Σ is the design variable (stress tensor) to be found, q is a vector containing the internal variables such as strain hardening and kinematic hardening variables to be found, C is the material stiffness matrix, $f(\Sigma, q)$ is the yield function, and E is the so-called matrix of generalized hardening moduli. One of the solutions to the above problem is the following equation for the plastic rate of deformation

$$D^{\mathrm{p}} = \lambda \frac{\partial f(\sigma, q)}{\partial \sigma} \tag{5.3}$$

In a crystal plasticity problem, the deformation is defined by several yield surfaces, and the number of yield functions depends on the number of slip systems in a crystal. Assuming the validity of the Schmid law for the plastic deformation of a single crystal, then for any slip system a yield function can be defined as:

$$f_\alpha(\sigma, q) = \frac{|\sigma : P^\alpha|}{\tau_y^\alpha} - 1 \tag{5.4}$$

The constraints of problem (2) can be combined and replaced by an equivalent single constraint defined as:

$$f(\sigma, q) = \frac{1}{\rho} \ln \left[\sum_{i=1}^{m} exp \left[\left(\rho \frac{|\sigma : P^\alpha|}{\tau_y^\alpha} - 1 \right) \right] \right] \tag{5.5}$$

Where τ_y^α is the critical shear stress on slip plane α, and P^α is the symmetric part of the Schmid tensor, I^α, describing the orientation of a slip system, defined as:

$$P^\alpha = \frac{1}{2} [(I^\alpha) + (I^\alpha)^T] = \frac{1}{2} \left(m^\alpha \otimes n^\alpha + (m^\alpha \otimes n^\alpha)^T \right) \tag{5.6}$$

where n^α is a unit normal to the slip plane, and m^α is a unit vector denoting the slip direction. The plastic deformation matrix can be expressed as

$$D^P = \sum_{\alpha=1}^{N} \dot{\gamma}^\alpha P^\alpha \tag{5.7}$$

where $\dot{\gamma}$ are the slip rates.

And spin tensor, which represents the material axis rotation, can be expressed as:

$$\Omega^p = \sum_{\alpha=1}^{N} \dot{\gamma}^\alpha \, w^\alpha \qquad (5.8)$$

where w^α matrix is the anti-symmetric part of I^α, defined as:

$$w^\alpha = \frac{1}{2}\left(m^\alpha \otimes n^\alpha - (m^\alpha \otimes n^\alpha)^T\right) \qquad (5.9)$$

It can be shown that during the plastic deformation of a single crystal the slip rate on any slip system could be expressed by:

$$\dot{\gamma}^\alpha = \lambda \frac{\dfrac{\mathrm{sgn}(\sigma:P^\alpha)}{\tau_y^\alpha}\exp\left[\left(\dfrac{\rho}{m}\dfrac{|\sigma:P^\alpha|}{\tau_y^\alpha}-1\right)\right]}{m\sum_{\beta=1}^{N}\exp\left[\left(\dfrac{\rho}{m}\dfrac{|\sigma:P^\alpha|}{\tau_y^\alpha}-1\right)\right]} \qquad (5.10)$$

where m and ρ are material parameters that control the shape of the single-crystal yield surface, and been shown to have a direct relationship with the stacking fault energy (SFE) of the material as following:

$$\rho = \frac{5\Gamma}{Gb} \times 10^{-3} \qquad (5.11)$$

Where Γ is the SFE of the material, G is the shear modulus, and b is the magnitude of Burgers vector. For most materials $m = 1$ Parameter λ is a Lagrange multiplier which has been shown to be a measure of the rate of plastic work in a crystal,

The generalized Schmid factor can be found for each slip system α by finding the scalar product of the normalized stress tensor (using the Frobenious norm) and the Schmid matrix.

In order to define the resistance against the shear, Hill (1966) and Asaro and Needleman (1985) proposed the following formulation:

$$\dot{\tau}^\alpha = \sum_{\beta=1}^{N} h^{\alpha\beta} |\dot{\gamma}^\beta|$$

(5.12)

where $|\dot{\gamma}^\beta|$ is the plastic slip rate on the active slip system β, and $h^{\alpha\beta}$ are the components of the hardening matrix $h^{\alpha\alpha}$ are known as the self-hardening moduli while $h^{\alpha\beta}$ for $\alpha \neq \beta$ are known as the latent-hardening moduli. Hutchison (1976) proposed the following model for evolution of the components of hardening matrix

$$h^{\alpha\beta} = h^\beta [q + (1-q)\delta^{\alpha\beta}]$$

(5.13)

Here q is the so-called latent-hardening ratio, which is the hardening on a secondary slip system caused by slip on a primary slip system (Kapoor and Nemat-Nasser (1999)) and can be measured by the ratio of the latent-hardening rate to the self-hardening rate of a slip system with typical values in the range of $1 < q < 1.4$. The parameter q can be considered as 1 for coplanar slip systems and 1.4 for non-coplanar slip systems. There are different kinds of hardening models presented by researchers for the evolution of h^β (so-called self-hardening). One of the most well-known formulations is:

$$h^\beta = h_0 \left|1 - \frac{\tau_y^\beta}{\tau_s}\right|^a \text{sgn}\left(1 - \frac{\tau_y^\beta}{\tau_s}\right)$$

(5.14)

where h_0, a, and τ_s are slip system hardening parameters, which are considered to be identical for all slip systems. h_0 denotes the initial hardening rate, τ_s the saturation value of the slip resistance, and a the exponent describing the shape of the stress-strain yield function. These parameters can be obtained by fitting the model to experimental data.

Finite element software ABAQUS is utilized as a tool to build the geometric shape of grains (single crystal or cyclic twining morphologies) and to conduct the FEM solution. ABAQUS provides a special interface, called user subroutine VUMAT, which allows the user to define the mechanical behavior of a material and to interface with any externally defined programs.

If timestep=0 then

Set $\sigma_{i+1}^{ave} = 0 \; and \; K = 1$

1.1-Build Q using Equation 5-38

1.2. Calculate P^α and W^α using m^α and s^α:

$$P^\alpha = \frac{1}{2}(m^\alpha \otimes n^\alpha + (n^\alpha \otimes m^\alpha)^T) \tag{5.15}$$

1.3. Initialize the critical resolve shear stress:

$$\tau_o^\alpha = \tau_c^\alpha \text{ For } \alpha = 1, \dots, N \tag{5.16}$$

EndIf

Else

Rotate $\sigma, \Delta\varepsilon$ from the global coordinate system to crystal coordinate system using the following equations:

$$\acute{\sigma} = Q \, \sigma Q^T \tag{5.17}$$

$$\acute{\varepsilon} = Q \, \Delta\varepsilon Q^T \tag{5.18}$$

A-Calculate the trial stress, initial resolved shear stress, Initial Lagrange multiplier and shear strain as following:

$$\sigma_{i+1} = \sigma_i + C : \Delta\varepsilon \tag{5.19}$$

$$\tau_o^{\alpha\,(0)} = \tau_c^{\alpha} \tag{5.20}$$

$$\Delta\lambda_{i+1}^{(0)} = 0 \tag{5.21}$$

$$\Delta\gamma_{i+1}^{(0)} = 0 \tag{5.22}$$

Find the initial incremental rotation of the grain using:

$$\Delta Q^{(0)} = \exp\left(\Omega\Delta t\right) \tag{5.23}$$

Find the stress tensor for current crystal axes:

$$\sigma_{i+1}^{(0)} = \Delta Q^{(0)} \sigma \Delta Q^{T(0)} \tag{5.24}$$

Calculate $f_{i+1}^{(j)}$ If $f_{i+1}^{(j)} \leq 0$ go to A

Calculate the incremental spin tensor using the following equation:

$$\Omega_i^P \Delta t = \sum_{\alpha=1}^{N} \Delta\gamma_i^{\alpha} \, w_i^{\alpha} \tag{5.25}$$

Compute the rotation of grain at current iteration:

$$\Delta Q^{(i)} = \exp\left(x\Omega_i^P \Delta t\right) \tag{5.26}$$

Rotate the stress tensor to the crystal coordinate system

Find the increment of plastic consistency parameter:

$$\Delta\lambda_{i+1}^{(n)} = \frac{f_{i+1}^n}{\frac{\partial f_{i+1}^{(n)}}{\partial\sigma}:C:\frac{\partial f_{i+1}^{(n)}}{\partial\sigma} - \sum_{\alpha=1}^{N}\sum_{\beta=1}^{N} h^{\alpha\beta}\frac{\partial f_{i+1}^{(n)}}{\partial\tau^\beta}\cdot\frac{\partial f_{i+1}^{(n)}}{\partial\tau^\alpha}} \tag{5.27}$$

Compute the stress, shear strain slip systems hardening increment and shear resistance using plastic corrector

$$\sigma_{i+1}^{n+1} = \sigma_{i+1}^{n} - \Delta\lambda_{i+1}^{n}C:\frac{\partial f(\sigma_{i+1}^{n})}{\partial\sigma} \tag{5.28}$$

$$\Delta\gamma^{\alpha}{}_{i+1}^{n+1} = \Delta\lambda_{i+1}^{n}C:\frac{\partial f(\sigma_{i+1}^{n})}{\partial\tau^\alpha} \tag{5.29}$$

$$\Delta\tau^{\alpha}{}_{i+1}^{(n)} = \sum_{\beta=1}^{N} h^{\alpha\beta(n)}\left|\Delta\gamma^{\beta}{}_{i+1}^{(i)}\right| \tag{5.30}$$

$$\tau^{\alpha}{}_{i+1}^{(n+1)} = \tau^{\alpha}{}_{i+1}^{(n)} + \Delta\tau^{\alpha}{}_{i+1}^{(n)} \quad \text{For)the st} \tag{5.31}$$

Update the increment of incremental slip rate:

$$\Delta\gamma^{\alpha}{}_{i+1} = \Delta\gamma^{\alpha}{}_{i+1} + \Delta\gamma^{\alpha}{}_{i+1}^{(n+1)} \quad \text{For the inc} \tag{5.32}$$

Set i←i+1

$$\Omega_i^P\Delta t = \sum_{\alpha=1}^{N} \Delta\gamma_{i+1}^{\alpha} w_i^{\alpha} \tag{5.33}$$

Knowing the orientation matrix Q_i at the beginning of increment, update the orientation matrix as:

$$\Omega_i^P \Delta t = \sqrt{(\Omega_i^P \Delta t : \Omega_i^P \Delta t)/2} \qquad (5.34)$$

$$\exp(x\Omega_i^P \Delta t) = I - \frac{\sin(\Omega_i^P \Delta t)}{\Omega_i^P \Delta t}(\Omega_i^P \Delta t) + \frac{1-\cos(\Omega_i^P \Delta t)}{(\Omega_i^P \Delta t)^2}(\Omega_i^P \Delta t)^2 \qquad (5.35)$$

$$Q_{i+1} = \exp(e\Omega_i^P \Delta t)Q_i \qquad (5.36)$$

Rotate the updated stress tensor back to the reference coordinate system

$$\sigma_{i+1} = Q_{i+1}^T \acute{\sigma} Q_{i+1} \qquad (5.37)$$

3.1. Orientation matrices in crystal structures:

Orientation of a crystal can be defined either by three Euler angels ($\varphi_1, \Phi, \varphi_2$) or for calculation purposes using, different orientation matrices. According to Kocks et al (2000) three kinds of conventions to define the crystal orientations are: Bunge, kocks, and Roe.

Bunge defined the orientation matrix as:

$$Q(\phi, \psi, \theta) =$$
$$\begin{bmatrix} \cos\varphi_1 \cos\varphi_2 - \sin\varphi_1 \sin\varphi_2 \cos\Phi & \sin\varphi_1 \cos\varphi_2 + \cos\varphi_1 \sin\varphi_2 \cos\Phi & \sin\varphi_2 \sin\Phi \\ -\cos\varphi_1 \sin\varphi_2 - \sin\varphi_1 \cos\varphi_2 \cos\Phi & -\sin\varphi_1 \sin\varphi_2 + \cos\varphi_1 \cos\varphi_2 \cos\Phi & \cos\varphi_2 \sin\Phi \\ \sin\varphi_1 \sin\Phi & -\cos\varphi_1 \sin\Phi & \cos\Phi \end{bmatrix}$$

$$(5.38)$$

Kocks defined the crystal orientation by three Euler angles $\phi\psi\Theta$ as:

$$Q(\phi, \psi, \Theta) = \begin{bmatrix} -\sin\psi\sin\phi - \cos\psi\cos\phi\cos\Theta & \cos\psi\sin\phi - \sin\psi\cos\phi\cos\Theta & \cos\phi\cos\Theta \\ \sin\psi\sin\phi - \cos\psi\cos\phi\cos\Theta & -\cos\psi\cos\phi - \sin\psi\sin\phi\cos\Theta & \sin\phi\sin\Theta \\ \cos\psi\sin\Theta & \sin\psi\sin\Theta & \cos\Theta \end{bmatrix}$$

$$(5.39)$$

and finally Roe presented the crystal orientation as:

$$Q(\phi, \psi, \Theta) = \begin{bmatrix} -\sin\psi\sin\phi + \cos\psi\cos\phi\cos\Theta & \cos\psi\sin\phi + \sin\psi\cos\phi\cos\Theta & -\cos\phi\cos\Theta \\ -\sin\psi\sin\phi - \cos\psi\cos\phi\cos\Theta & \cos\psi\cos\phi - \sin\psi\sin\phi\cos\Theta & \sin\phi\sin\Theta \\ \cos\psi\sin\Theta & \sin\psi\sin\Theta & \cos\Theta \end{bmatrix}$$

$$(5.40)$$

CHAPTER 4

EXPERIMENTAL PROCEDURES

4.1. Single joint tensile samples

4.1.1. Sample preparation for joint level tensile test samples:

The specimen preparation procedures are intended to duplicate the structure (grain size and orientation) which is observed in the actual solder joints. For fabrication of 6 tensile samples a piece of 0.55 mm diameter copper wire with a thin lacquer insulation layer was cut into 25mm pieces. A jig was designed and fabricated to hold the samples during the polishing and solder fabrication processes. A schematic diagram of this jig is illustrated in Figure 4.1 where copper wires are placed in the jig and fixed. Polishing of the ends of the copper wires that were intended to be in contact with solder balls was conducted until a sufficient surface finish was obtained. In the next step, the copper wires were cut in the middle, and then flipped around so the polished sides faced each other in the jig. By leaving a particular distance between polished sides of the copper wire, it was possible to place a solder ball in the gap, to complete the fabrication of the tensile testing sample. Small pieces of Si sheets were utilized to prevent contact between the solder and the copper jig. Flux was applied on the ends of copper wires to allow the activation of solder. Lead-free SAC 305 (Sn-3.0Ag-0.5Cu (wt.%)) solder balls approximately 550 micron diameters were placed on the copper ends as shown in Figure 4.2 The assembly was heated on a hot plate with a thermocouple monitoring the temperature, to make the solder joint, and then cooled on an aluminum plate. The heating and cooling profile is shown in Figure 4.3. After the fabrication of the solders, the samples were aged for 500 hours at 150 ℃.

X-ray characterization of the joints were performed at the Argonne National Laboratory using beamlines 34 and 6 to obtain the crystallographic orientation before and after tensile deformation to just after maximum load. Radiographic evaluations were also made to assess the effects from porosity and voids in solder joints, on the mechanical properties of the samples.

4.1.2.Tensile test set up

Mechanical characterization of single solder balls were carried out using a Rheometric Solid Analyzer (RSA-III). Figure 4.4.a shows the setup which was utilized to conduct the mechanical testing. Single solder ball samples were subjected to tensile deformation at 25 ℃ with the displacement rate of 0.003mm/s. Force and displacements were recorded using the data acquisition software, and after the test stress relaxation data were also recorded.

Optical microscopy, radiography, and orientation x-ray characterization were conducted before and after the tensile test to identify changes in geometry and identify fraction locations.
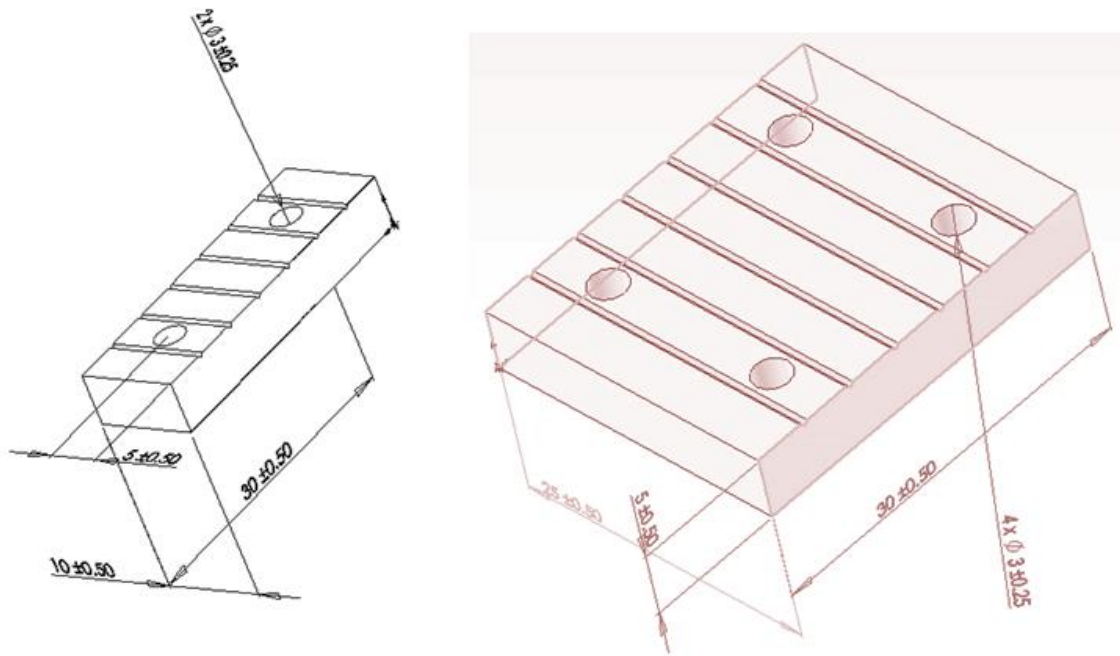
Figure 4.1 Schematic diagrams and dimensions of the jig used for polishing and fabrication of joint level tensile samples.
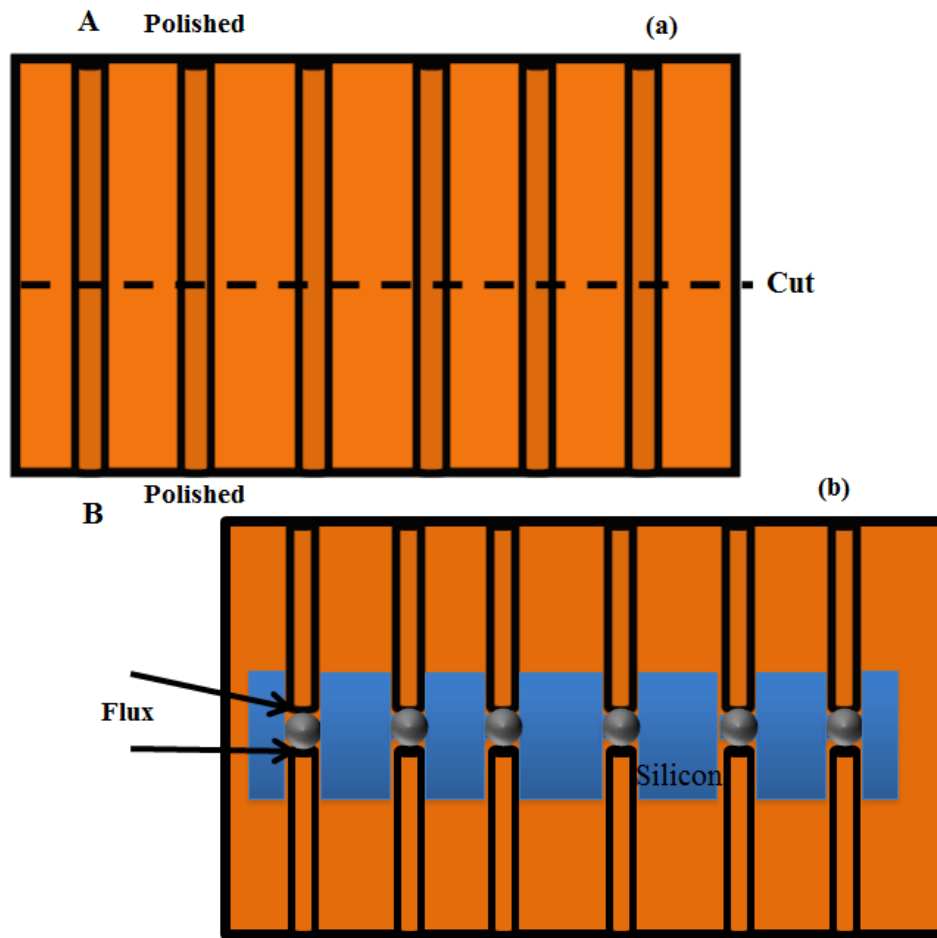
Figure 4.2 Schematic configurations of tensile samples inside the miniature jig (a) locations of polishing and cutting of copper wires are illustrated, (b) configuration of solder inside the jig and on silicon plates.
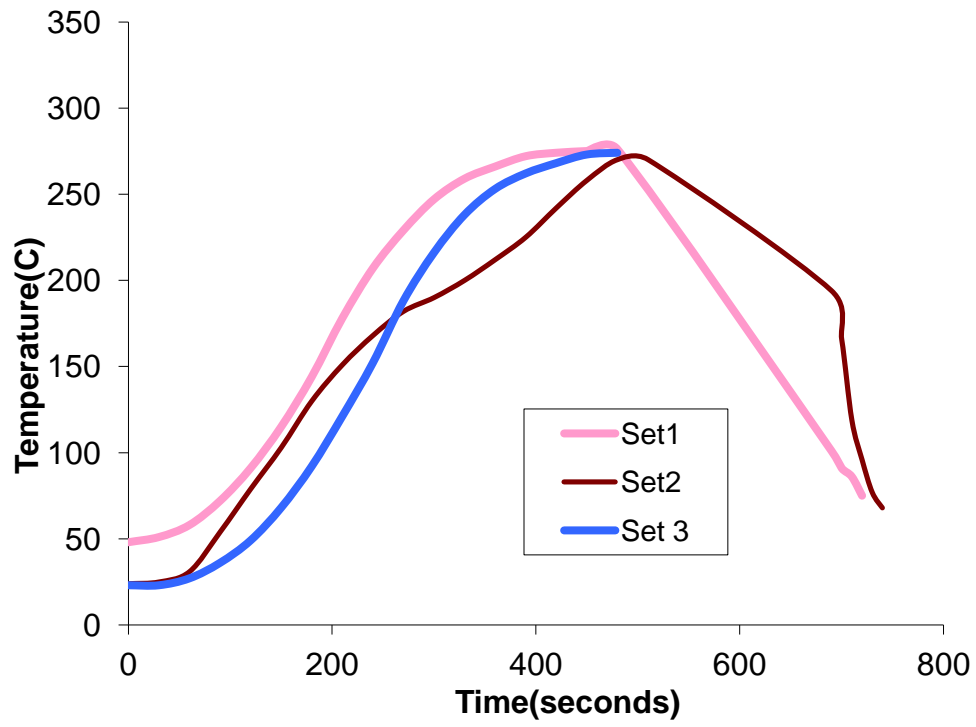
Figure 4.3 Temperature profiles used for fabricating solder joints
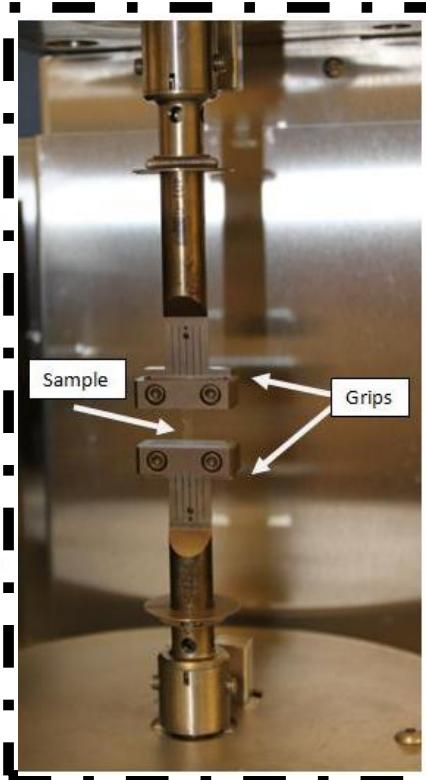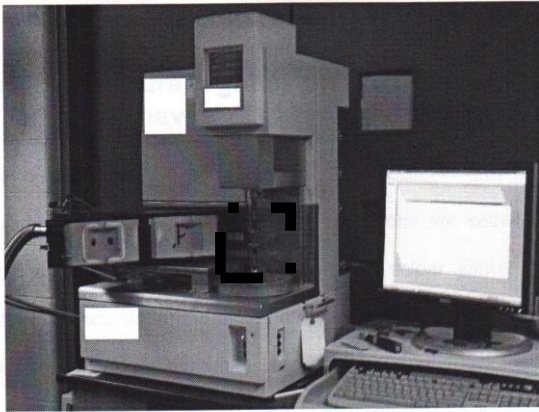
Figure 4.4 Set up employed for tensile testing, (a) RSA III equipment.

4.2.1 Shear samples

Eight (8) specially prepared samples of a 4×4 ball grid array (BGA) were cut from a 15 mm × 15 mm body-size plastic ball grid array (PBGA) package with Sn-3.0Ag-0.5Cu (wt.%) solder joints. Four (4) samples were aged at 100ºC for 500 hours. The samples were sectioned and carefully polished so that the plane of shear at the center of the joint could be observed on one set of four balls before and after shear displacements. Due to the path dependency in plasticity, the total displacement was applied in three steps in order to obtain the information about the shape change and crystal rotation during the shear deformation. A fixture was used to impose a two-dimensional shear strain, so that small out of the plane variations of shear resulting from local strain effects could be detected topographically on the previously polished surface. Figure 4.5 shows the schematic of the apparatus in this experiment. To permit accurate orientation measurements, samples were lightly re-polished to improve surface cleanliness after optical observations, and before orientation imaging microscopy (OIM) measurements. Optical microscopy, analysis of polarized light microscopy, OIM, and SEM were conducted initially, and after each deformation step.

4.3 Procedure for OIM characterizations:

The resin surrounding the balls and the package was carefully painted over with carbon paint to cover the nonconducting surfaces. Also, the polished samples were covered by copper tape away from the solder joints to provide a conductive path, and to prevent the charging effect which causes image distortion or beam drift.

OIM data were obtained in a CamScan 44FE electron microscope. The digital image resolution of this microscope is 640×480 pixel size, and the accelerating voltage was set to be 20 kV and
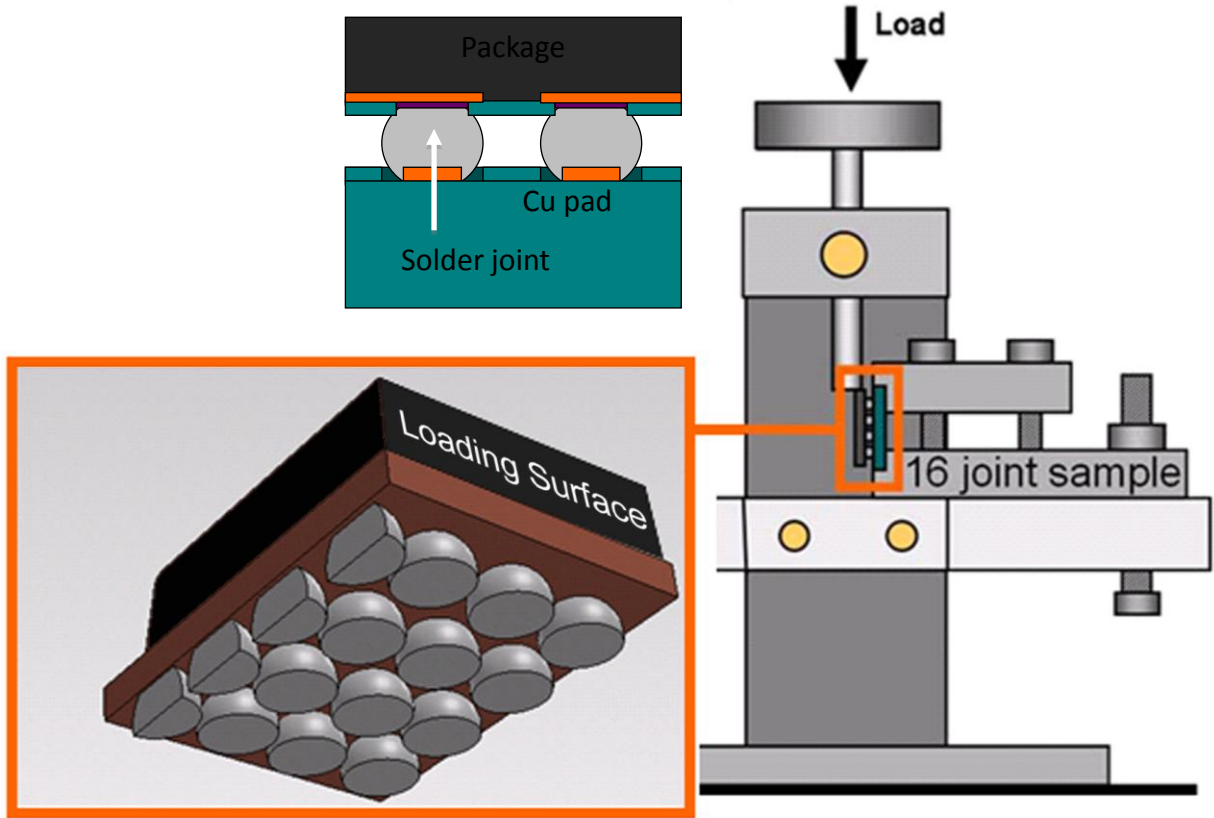
Figure 4.5 Schematic diagrams of a 4 × 4 solder joint array sectioned from a PBGA package. The solder ball assembly geometry and shear test apparatus is also shown.

the working distance was 33 mm. A TSL EDAX system with a Digiview SEM detector was utilized. An acquisition speed of 15-20 points per second was obtained using 2×2 binning setting. EDAX TSL OIM Analysis software was used to generate the orientation maps.

Maps were cleaned up using the neighbor confidence index (CI) correlation to replace pixels that had low CI with their neighbors having a high CI. This step is required to remove the minority data points coming from un-indexed or wrongly indexed patterns. In the neighbor-confidence-index-correlation method, a datum point having a low CI is replaced with the neighboring point that has the highest CI value

A user defined orientation map was employed to correlate the orientation of Sn c-axis [001] with respect to solder/package interface. For this orientation map, a graded 5 color scale (Purple-blue-green-yellow-red) was used to represent the orientation of the c-axis with respect to the solder/package interface. When the c-axis is on the interface plane, the orientation is expressed as "red" while when the c-axis is perpendicular to the surface the orientation is "purple". Other colors (blue, green and yellow) fill in the rest of the orientation space. Figure 4.6 shows the general procedure for OIM analysis.

4.4 X-ray diffraction

4.4.1- Beamline 34-ID-E

Synchrotron X-ray microdiffraction experiments were conducted on beamline 34-ID-E at the Advanced Photon Source (APS) at Argonne National Laboratory. The experimental set-up is illustrated in Figure 4.7 and described in chapter 2. A white beam with an energy range of 7-30 keV was used in the microdiffraction experiment with a beam size of approximately

5μm×0.5μm. The scanning step-size was set to be 1μm in a non-depth-resolved surface area-scan (in the horizontal X and vertical H directions as defined in their coordinate system). Fifteen (15) joint level tensile samples were characterized using beamline 34-ID-E before deformation. Two (2) sides of each sample were scanned by the X-ray beam. For each step along the scan, the diffraction pattern provided information from about 100 μm in depth along the incident beam direction.

4.4.2- Beamline 6-ID-E

Characterization of Sn crystal orientation in joint level tensile samples using a high energy monochromatic X-ray beam was accomplished at beamline 6-ID-D at the Advanced Photon Source (APS) at the Argonne National Laboratory. A 2048 × 2048 pixel PerkinElmer XRD 1621 AN/CN area detector was employed to collect the diffraction patterns. To extract accurate intensities from the detector, dark current images without the beam were used as the background. Subtraction of background from the diffraction patterns were conducted automatically using the acquisition software. To calibrate the beam diffraction, patterns from a silicon powder standard was used, which resulted in calibration wavelength of 0.12492 A˚ and ''distance to detector'' of 1112.75 mm. Fit2D software was utilized to integrate and analyze the diffraction peaks from selected portions of the pattern.
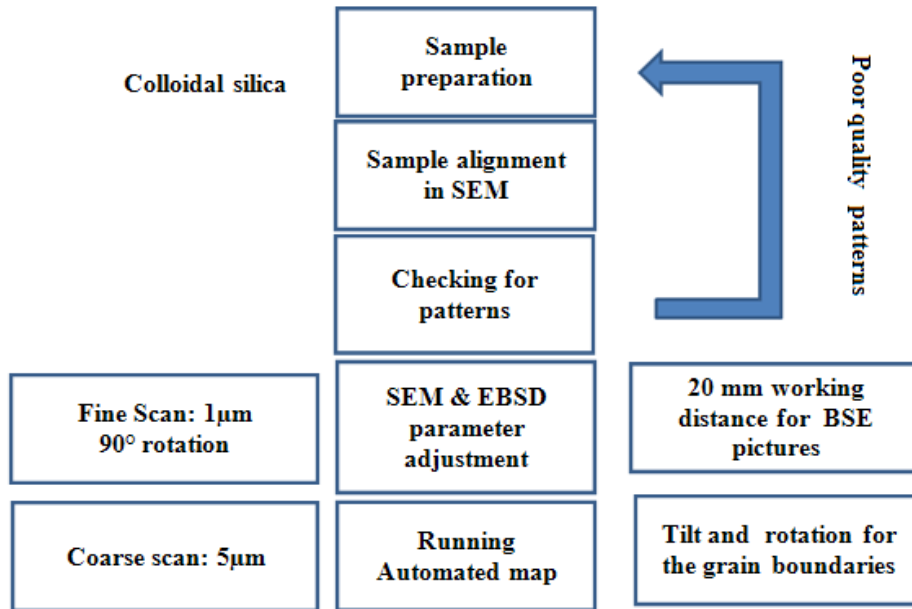
Figure 4.6 General procedures for conducting the EBSD analysis.
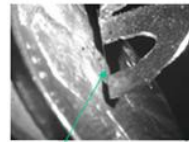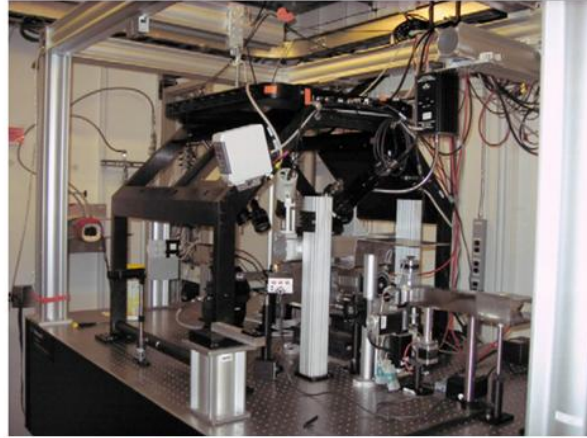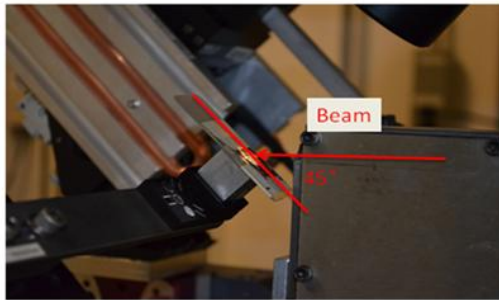
Figure 4.7 Experimental setup at synchrotron beamline 34-ID-E for conducting the characterization of joint level tensile samples (a) platinum wire used as a differential aperture. (b) Experimental station for conducting the synchrotron X-ray microdiffraction (c) sample stage 45º inclined with respect to beam direction.

CHAPTER 5

CRYSTAL PLASTICITY FINITE ELEMENT ANALYSIS OF DEFORMATION BEHAVIOR IN MULTIPLE-GRAINED LEAD-FREE SOLDER JOINTS

5.1 Introduction

Anisotropy is of significant importance in all structural metals, but this characteristic is unusually strong in Sn, making Sn based solder joints one of the best examples of the influence of anisotropy. The fracture probability in lead-based solder alloys is quite different from lead-free solder alloys, mostly because of anisotropy present in the tin phase [House(1960)]. While in lead-tin based solder alloys, the location in the solder area that is most prone to the failure can be predicted, the crystal structure of tin in lead-free solder alloys can highly affect the damage initiation and evolution. This is because the coefficient of thermal expansion (CTE) plays an important role in thermo-mechanical loading of solder joints, leading to significant axial as well as shear strains acting on joints [Bieler et.al (2008)]. Also, the residual stresses that are generated during the initial cooling and thermal-cycling can cause dislocation motion.

Crystal features such as grain size and morphology have significant effects on the mechanical properties and reliability of sub-mm scale joints. Some studies about the microstructure and Sn grain morphologies in lead free solders joints show peculiar microstructures, such as the beach-ball morphology, in which 60° cyclic twins can be formed during the solidification.

There are a few papers about using the crystal plasticity to model the slip behavior in lead free solder joints. The majority of previous studies are based on the isotropic plasticity models which may be useful for polycrystals but for the lead-free solder joints that are inherently either single crystal or multi-crystals, using just the anisotropic plasticity models is not physically sufficient.

In this type of analysis it is very important to take into account both spatial (effect of particular morphologies) and orientation space (effect of grain orientation and its consistency with morphology).

Incompatibilities along grain boundaries arise in lead-free solder joints from the anisotropy in the CTE in the specific configuration of grains in the microstructure, which increases the complexity of the problem and makes using the CPFE necessary for understanding of the deformation behavior. One of the advantages of crystal plasticity modeling is its ability to solve mechanical problems under the complicated external and internal constraints imposed by inter and intra-grain slip mechanisms. Using microstructural scale CPFE is of great importance because at these scales experimental boundary conditions are very difficult to control and monitor. In such cases experimental results will be very difficult to interpret without the assistance of a model with similar complexity. Miniaturization is a very important issue in solder joints because the dimension in the joint is in the range of the grain scale. The design of solder joints will increasingly require consideration of grain scale anisotropy.

Since there is a lack of consistent data available to establish models for dislocation slip activity, this work will examine the effects of grain geometry and orientation using overly simple models. Thus, this work will establish a basis for comparison that can be used with future refinements in the models that can be developed once sufficiently detailed experimental data sets are established for comparison. This will provide a basis for assessing the ability of better models to make better predictions. Furthermore, establishing this simple model will also assist in the interpretation of experimental characterization. As there is little experimental work that can be

easily compared with a CPFE simulation in detail, this work will consider partial agreement with experimental observations as a success to be improved upon. Thus, this work provides a basis for an integrated incremental model development strategy based upon experiments, modeling and comparative analysis.

A crystal plasticity model developed by Zamiri and Pourboghrat (2010) which is implemented into ABAQUS finite element software was used to analyze the elastic–plastic deformation in the tin phase.

The finite element analysis was performed using commercial finite element code ABAQUS. The crystal plasticity material model was implemented using a user material subroutine in FORTRAN (VUMAT). Solid works was used to make the model of a tri-crystal shown in Figure 5.1 and ABAQUS was used to create the finite element mesh with the assignment of the boundary conditions shown in Figure 5.2, and building the input parameters for the analysis. Element types and number of elements used in CPFE are shown in Table 5.4. The elements are 8-node linear bricks with reduced integration and hourglass control. Hourglassing can be a problem with first-order, reduced-integration elements (CPS4R, CAX4R, C3D8R, etc.) in stress/displacement analyses. Since the elements have only one integration point, it is possible for them to distort in such a way that the strains calculated at the integration points are all zero, which, in turn, leads to uncontrolled distortion of the mesh. First-order, reduced-integration elements in ABAQUS include hourglass control, but they should be used with reasonably fine meshes. Hourglassing can also be minimized by distributing point loads and boundary conditions over a number of adjacent nodes. The elastic constants for tin and copper are known
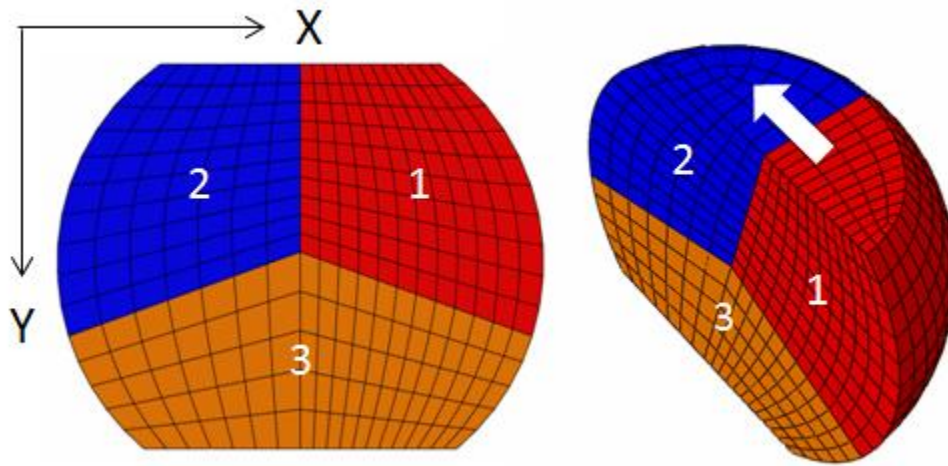
Figure 5.1 Simplified model of a of tri-crystal microstructure in half-joint configuration, with coordinate system used for Euler angles.

74
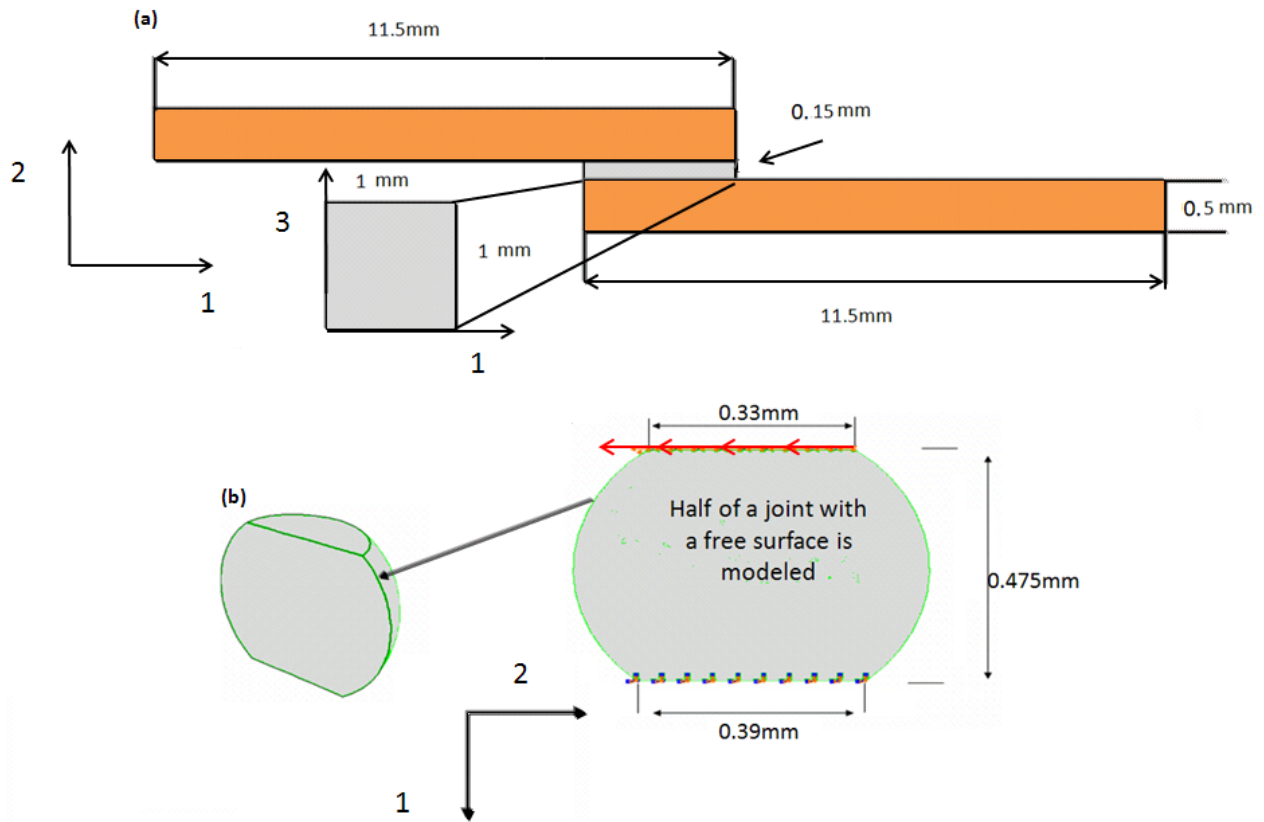
Figure 5.2 Geometry and dimensions of (a) lap-shear samples, and (b) solder balls used in this study. The sense of shear is to the left on the upper surface of the joint.

and tabulated in Tables 5.1, and 5.2, respectively. The parameters used for hardening in Table 5.4 were chosen so that they generated trends that are commonly observed in polycrystal or multi-joint experiments (Darveaux et. al (2005)) and various single crystal experiments (Zhou et. al (2009), Bieler et al (2012)).

5.2 Single shear lap simulations

Single lap-shear samples with different crystal orientations were computationally deformed to identify how the shear stress-shear strain behavior depends on crystal orientation. The behavior of one element in the center of the joint is illustrated in Figure 5.3 for five different crystal orientations. In each computation, all elements in the joint started with the initial crystal orientation indicated by the Bunge Euler angles φ_1-Φ-φ_2. Deformation of the orientation 75°-45°-0° showed a smooth response similar to measured data from shear-lap samples consisting of a group of joints (Darveaux et. al (2005)). Hardening parameters were adjusted to the values in Table 5.4 so that this orientation matched the Darveaux data, as illustrated in Figure 5.3. These hardening parameters for the slip system flow curves were used for all subsequent simulations in this chapter. It is interesting that based upon these hardening parameters, the response of the joint varied with different initial orientations; some provided higher stress-strain behavior, others lower. A couple of the orientations had changes in the flow behavior at different places along the stress-strain curve (Figure 5.3). The parameters for these phenomenological flow curves (Table 5.4) are considered estimates that serve as a starting point for iterative development of improved model parameters, as comparisons between experimental data and simulations of these experiments progress.

Table 5.1 Elastic C onstants (GPa) of Tin used in numerical analysis

Parameter	C11	C22	C33	C44	C55	C66	C12	C13	C23
	72.3	72.3	88.4	22.0	22.0	24.0	59.4	35.8	35.8

Table 5.2 Elastic constants (GPa) of Cu.

C11	C12	C44
178	76	45

Table 5.3 Hardening parameters of tin for different slip systems used in numerical analysis

Parameter	τ_0	τ_s	h_0	a	q	m	ρ
	23(for all sets)	40(for all sets)	100 for sets(1,2,5,7,)	2.0(for all sets)	1.4	1	60
			150 for sets(3,4,6,8,9,10)				

Table 5.4 Element Types and number of elements used in CPFE.

Material	No. of elements	Type of element
Tin in lap-shear	360	C3D8R
Cu in lap-shear	2780	C3D8R
Tin in solder ball	494	C3D8R
Tin in Tri-Crystal	1065	C3D8R
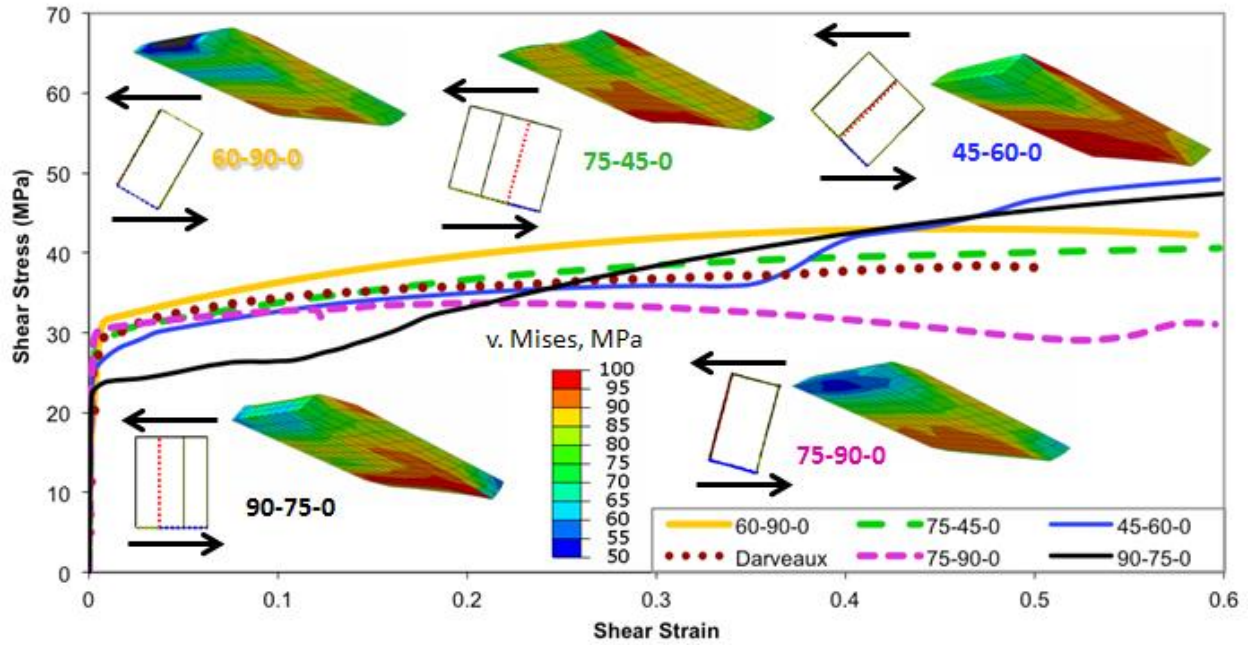
Figure 5.3 The orientation φ_1-Φ-φ_2 = 75°-45°-0° was used to estimate crystal plasticity model parameters using experimental data of Darveaux et al. (2005). Using these model parameters, other orientations deformed differently in simulated single shear lap deformation. The distributions of von Mises stress in the joint are shown to illustrate effects of orientation on stress distribution.

78

The shear strain on the most active slip systems that contribute to the shear stress-shear strain behavior in Figure 5.3 are plotted in Figure 5.4. The effect of conjugate slip systems is evident in Figure 5.4, as there are four slip systems where the plane normal and slip directions are perpendicular to each other, so they have the same Schmid factors. For example, the slip system (001)[100] and (100)[001] have the same Schmid factor, but the (100)[001] is expected to be more facile and is frequently observed, due to a smaller Burgers vector. Slip on the (001)[100] system has been observed (Zhou et. al (2009)), but less frequently. Thus, as the hardening parameters for Sn are refined, it is expected the (001)[100] should have greater slip resistance than (100)[001], but at this point they are made equal (there are similar conjugate systems on (010) planes and [010] directions, too). The other two pairs of conjugate slip systems, e.g. $(101)[10\bar{1}]$ and $(10\bar{1})[101]$ should truly be equally balanced, as they are members of the same family (#9 in Table 1.1, and similarly for (011) planes and [011] directions).

As can be seen for orientation 75-45-0 in Figure 5.4, there are more slip activity on $(10\bar{1})[101]$ than any other slip system throughout the deformation. There is some shear strain developing on $(110)[1\bar{1}1]$ and $(1\bar{2}0)[\bar{1}01]$ slip systems, but their magnitudes are small and therefore have a small impact on the evolution of the shear stress. The combined effect of slip activities on these systems leads to a smooth and moderate hardening behavior that is expected for predominantly single slip orientation with some activity on secondary slip systems. In contrast, the 45-60-0 orientation had four slip systems with similar activity at the early stage of strain, and the least active of these top four became the most active at larger strains. With four systems initially favored, the yield stress was low, but the initial hardening rate was high. The stress-strain plot shows several changes in the slope that reflects changes in the dominant contribution of different
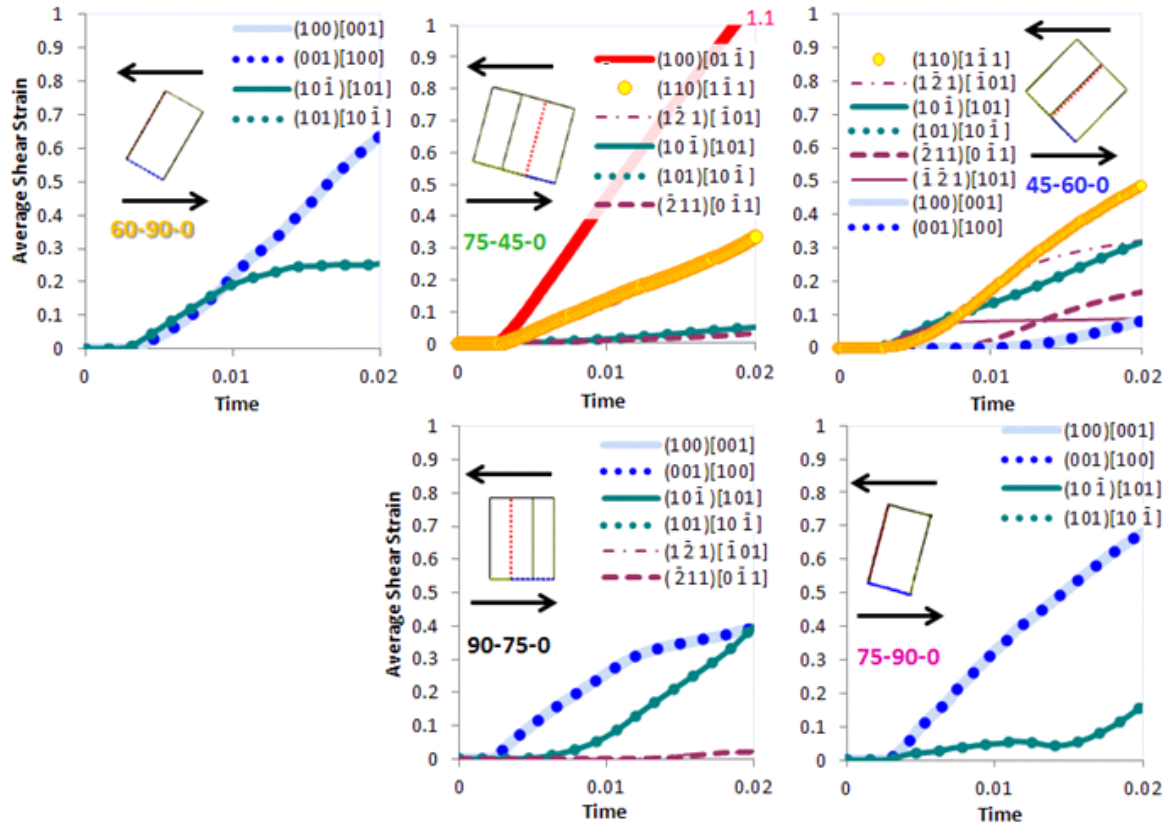
Figure 5.4 Shear strain in one element in the middle of the joint in the single shear lap geometry. Some slip systems have conjugate partners that are 90° apart, and have the same Schmid factors; these two distinct systems are illustrated with lines and overlaid dots.

slip systems and jumps in flow stress, where some latent systems became hardened when they were favored at larger strains.

For the 90-75-0 orientation, two pairs of conjugate slip systems contributed to the hardening process, and changed the slope, but one pair dominated in the beginning, (100)[001], and later, the second pair, $(10\bar{1})[101]$, gradually became favored. As this second system became active, the flow stress and hardening rate started to increase at a strain of about 13%. In contrast, for the 60-90-0 orientation, the same two pairs of slip systems were both active in the beginning, and (100) [001] became favored with increasing strain. The operation of all four at the beginning led to the highest initial flow stress, and as the $(10\bar{1})[101]$ pair became less active, the hardening rate decreased. In the 75-90-0 orientation, the $(10\bar{1})[101]$ pair was not very active until much later, resulting in a low initial hardening rate that led to softening, presumably due to rotation to a more favorable orientation with a lower Schmid factor, but eventually, the $(10\bar{1})[101]$ pair became more active, and led to hardening at large strain.

5.3. Tri-crystal simulations

Tri-crystals having a triple junction in the center of the joint were computationally deformed, using orientations defined in Figure 5.1 and **Table 5.5**. These orientations are all related by 60° rotations about the crystal [100] axis to provide misorientations across grain boundaries that are similar to beach ball morphology, but geometrically simpler; similar geometries are sometimes observed. The computational model was deformed to a simple shear strain of 0.84. The average shears on active slip systems for all elements in each initial orientation in Samples A, B, and C are laid out for comparison in Figure 5.5, where each column represents a different orientation set permutation, and each row represents the same crystal orientation. The colors of lines are

Table 5.5. Bunge Euler Angle values for different tri-crystal sets

	1 (φ1 Φ φ2) °	2 (φ1 Φ φ2) °	3 (φ1 Φ φ2) °
A	120,90,0	180,90,0	240,90,0
B	240,90,0	120,90,0	180,90,0
C	180,90,0	120,90,0	240,90,0
D	150,90,0	30,90,0	90,90,0

coded to the slip systems used in Table 1.1. Activity of multiple members of a slip system family are given the same color, but have different line thicknesses and dashes for specific systems as indicated in the legends.

Study of the shear response in each row shows that the shear deformation behavior in position 1 (along the diagonal) differs from the activated systems when the crystal is in one of the other two positions. This shows that the activation of slip systems depends on both the geometrical position and the orientation of neighboring orientations. For example, in the first row of Figure 5.5, for orientation 120-90-0, the activity of the $(10\bar{1})[101]$ exceeds the other slip systems substantially in position 1, whereas in the same orientation in positions 2 and 3 still show this system as most active, but there is more balanced activity on several other similar slip systems. In the third row, for orientation 180-90-0, (100)[001] is dominant when this orientation is in position 1, but not when it is in position 2 or 3. These observations indicate that the deformation kinematics of position 1 differs significantly from positions 2 and 3.

The activated slip systems in Figure 5.5 commonly show activity on slip system 9,$< 101]\{10\bar{1}]$, but this system is generally thought to be less easily activated than other slip systems. Thus the yield stress for activation of this slip system was increased by a factor of 10, and the same deformation path was imposed, and the difference in activity of slip systems is shown in Figure 5.6. By suppression of the slip on system #9, slip on systems 4 <111>{110) and 10 $<$ 211]$\{\bar{1}01]$ were more highly activated. Figure 5.7 illustrates a different permutation (D) of the crystal orientations where the first Euler angles were all smaller by 90° from the (B) orientation

set for the two conditions described above. Suppression of slip system 9 clearly requires greater activity on slip systems 4 and 10, and this figure makes it easier to see this comparison.

Figure5.8 shows the distribution of von-Mises stress in different tri-crystals at a shear strain of 0.84. The distribution of von-Mises stress at upper left corner of the solder balls is strongly affected by the crystal orientation; orientation sets B and C have the same orientation in the upper left, and both show greater resistance to shear deformation. Elsewhere, the von-Mises stress distribution is not much different for different orientation sets, though there are discontinuous stress jumps across the upper grain boundary for cases A and D. The effective stress value averages out heterogeneous deformation conditions if the magnitudes of strains are similar on different systems, and from the perspective of understanding slip behavior, it does not reveal much insight.

However, following the experimental observations by (Bieler et.al (2009)), it is likely that slip on both systems 9 and 10 are less easily activated, so von Mises stress plots for deformation with slip system 9 suppressed in Figure 5.9 at a lesser shear strain of 0.5 shows stresses that are a bit more heterogeneous, as less favorable slip systems need to be activated. With the additional suppression of slip system 10, the von Mises stress in Figure 5.9 at a shear strain of 0.5 is distributed much more heterogeneously, and the stresses are very large. There are bands of high stress in orientation sets B and C, and large stress discontinuities are evident at the triple point and along the lower right grain boundary in orientation sets C and D. Also, differential deformation in grains with different orientations is much more apparent (compare the right side of orientations A and C in Figure 5.10 with the right side of the tricrystal in Figure 5.3). As a
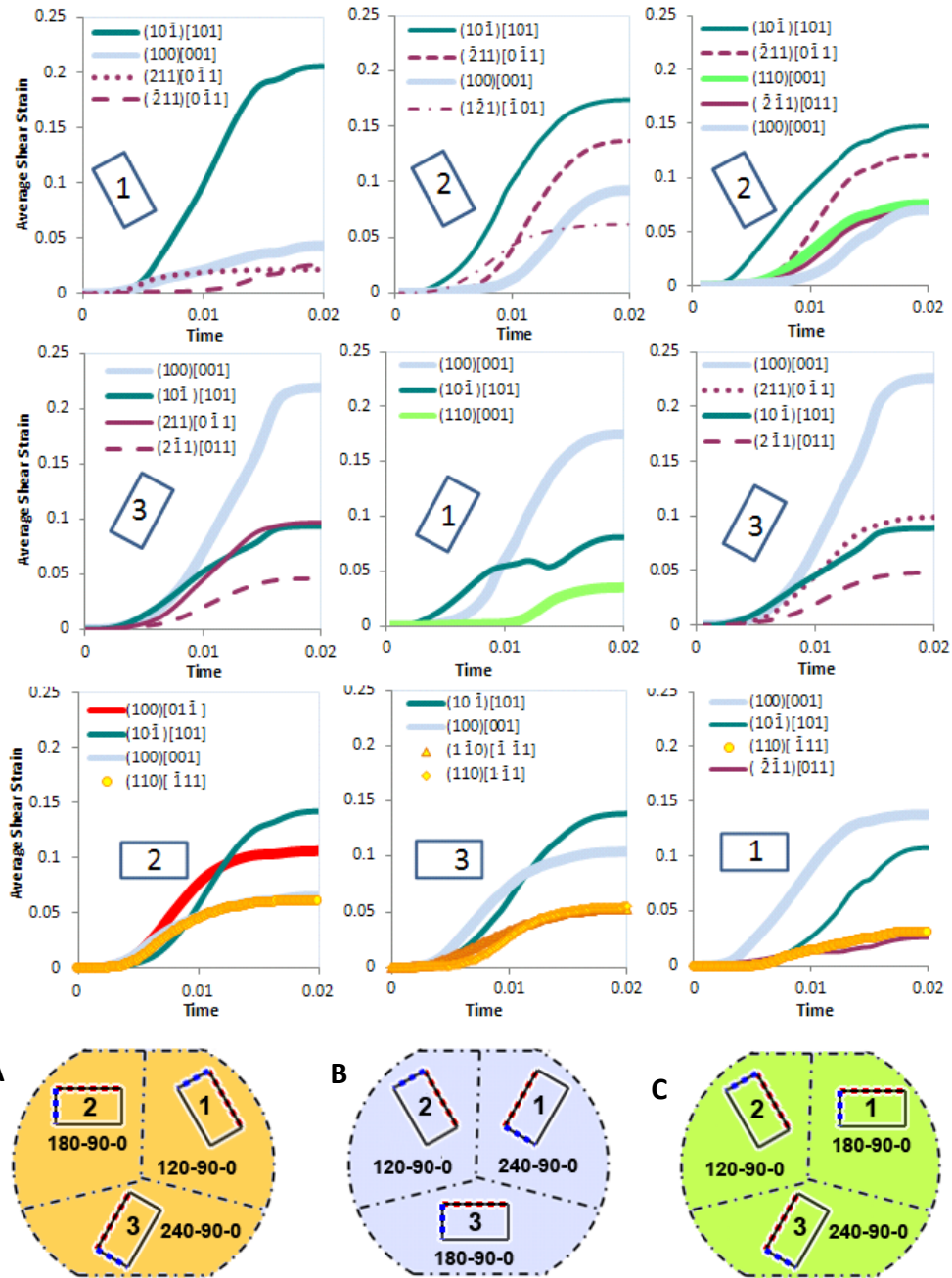
Figure 5.5 Average shear strain on the most active slip systems are compared in different orientation sets A, B, C, to illustrate the effects of location and interaction between different orientations. Slip system facility is based upon Table 2.1 Each row has the same crystal orientation (Table 5.4), but in a given row, the upper right grain (position 1, on the diagonal), exhibits different strain evolution than when the same orientation is in the other two positions.
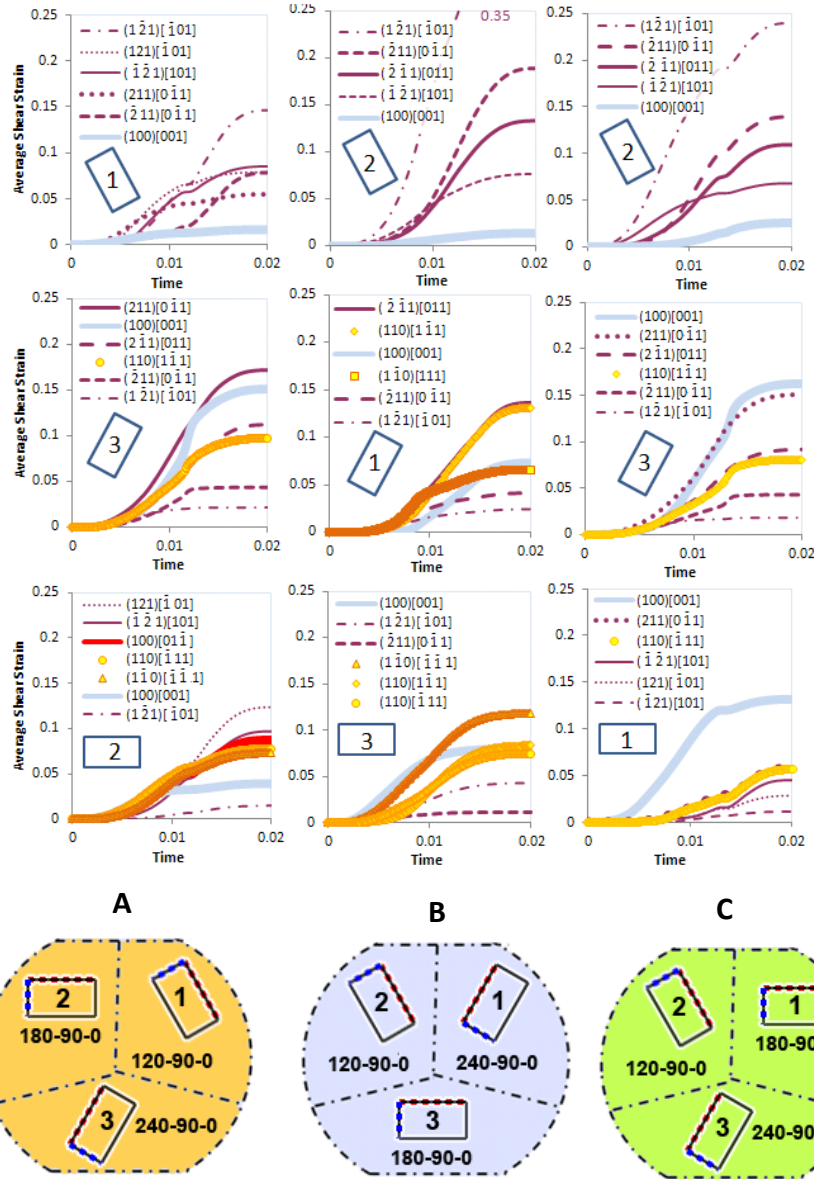
Figure 5.6 Average shear strain on the most active slip systems are compared in different orientation sets A, B, C, to illustrate the effects of location and interaction between different orientations. Slip system facility is based upon Table 5.3, but slip system 9 is suppressed. Each row has the same crystal orientation (Table 5.5), but in a given row, the upper right grain (position 1, on the diagonal), exhibits different strain evolution than when the same orientation is in the other two positions.

86
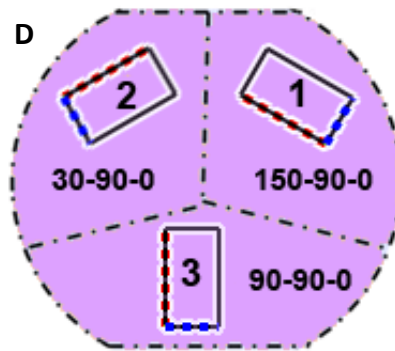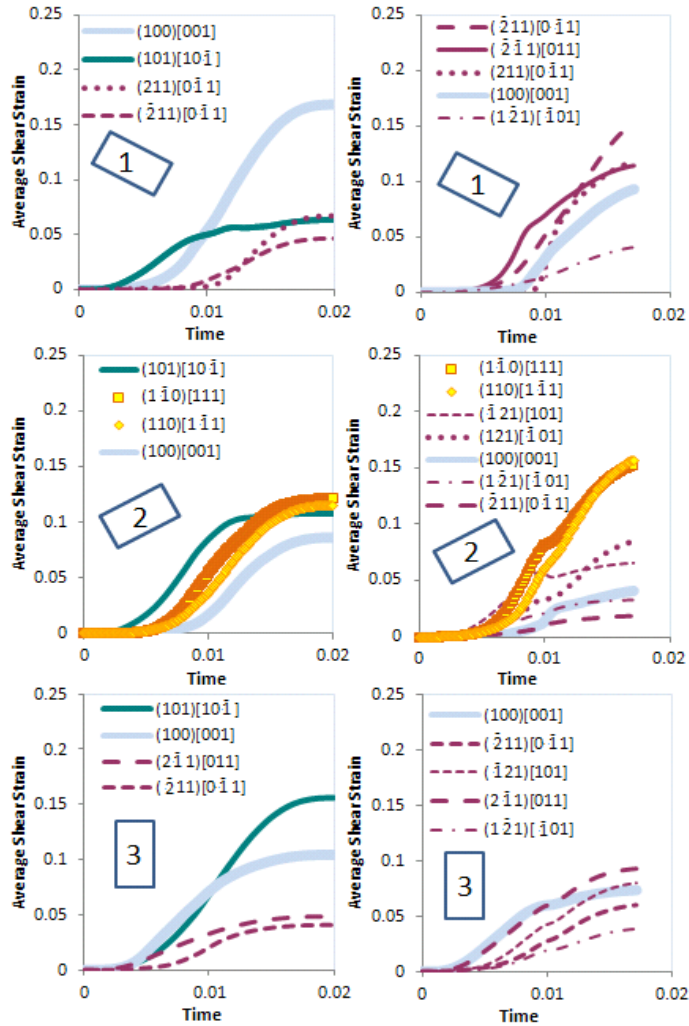
Figure 5.7 When slip system 9 <101]{10-1) is suppressed, to be more consistent with experimental observations (Zhou et al (2009)), activation on slip systems 4<111>{110) and 10 <211]{-101) increases.
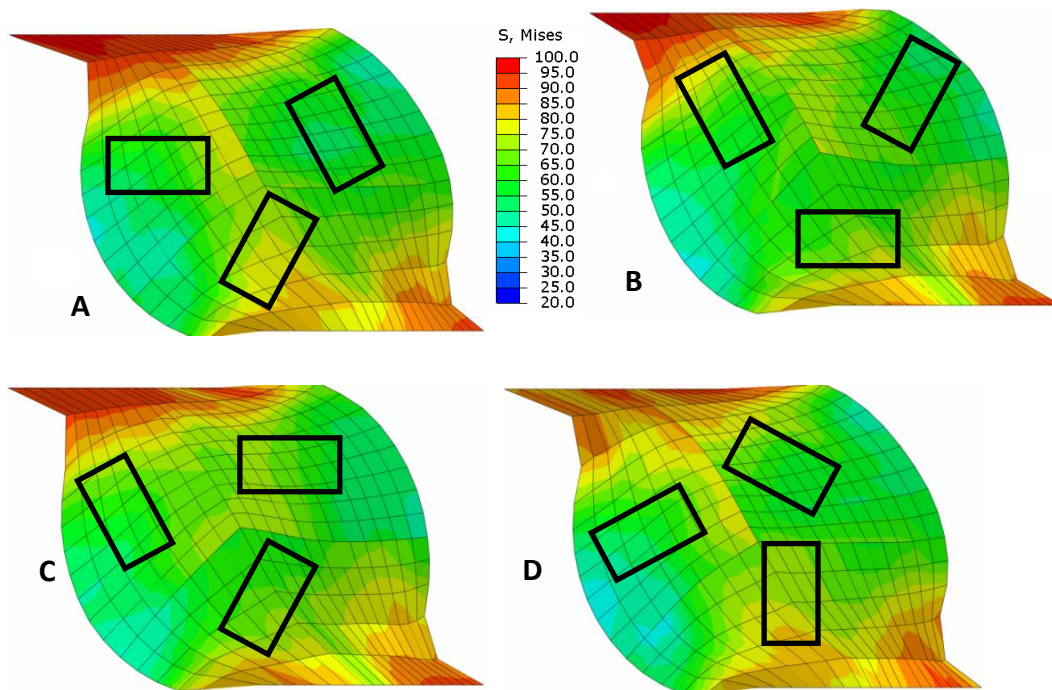
Figure 5.8 Distribution of von-Mises stress in different tri-crystals deformed to a simple shear strain of 0.84 with orientations defined in table 5.5 is rather similar. The grain orientation 120-90-0 in the upper left position resists shear more effectively than other orientations.
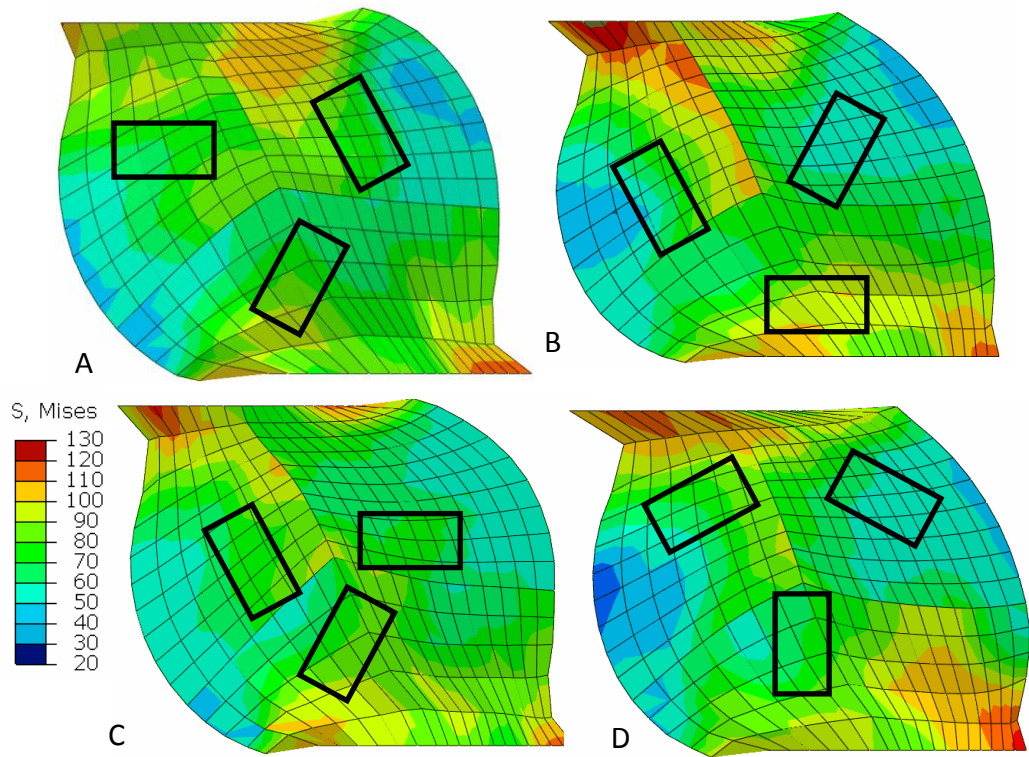
Figure 5.9 Distribution of von-Mises stress at a strain of 0.5 in different tri-crystals with orientations defined in table 5.5 differs when slip system 9 is suppressed. The grain orientation 120-90-0 in the upper left position in orientation sets B and C resists shear more effectively than other orientations.

higher stress is the outcome of more hardening, this implies higher total shear strain activity in the band of elements with higher stress. Such shear banding is occasionally observed in joints, especially in the form of orientation gradients surrounding a shear band.

One way to illustrate the presence of an orientation gradient is to plot the generalized Schmid factor based upon the local stress tensor for the most active slip systems in elements that go across the shear band. Figure 5.11 shows how the generalized Schmid factor varies spatially; an increase in the Schmid factor in one slip system and a corresponding decrease in another slip system shows that a substantial orientation gradient developed in regions of high stress. Under such conditions, it is not as meaningful to plot average shear for all elements in each grain orientation (as was done in Figures 7-9) due to the heterogeneous deformation. Indeed, shear activity plots from the dozen elements in the upper left corner in the simulation shown in Figure 5.8 differs substantially from the average (not shown). The degree of heterogeneous strain in Figure 5.10 is more dramatic than is commonly observed in solder joints, such as Figure 2.6 or shear deformation samples described in references (Bieler et.al (2009)), so complete suppression of slip systems 9 and 10 is probably too extreme, as reference (Bieler et.al (2009)) shows evidence for some activity on systems 9 and 10. Further optimization of model parameters using comparisons with experiments will be needed to identify more suitable rules for stress evolution among the 10 slip systems in Sn, and this will be addressed in future chapters. However, it is clear that the crystal plasticity finite element approach will be able to capture realistic heterogeneous deformation phenomena, and provide a means to predict slip behavior in SAC solder joint in a form that can be used with computational models.
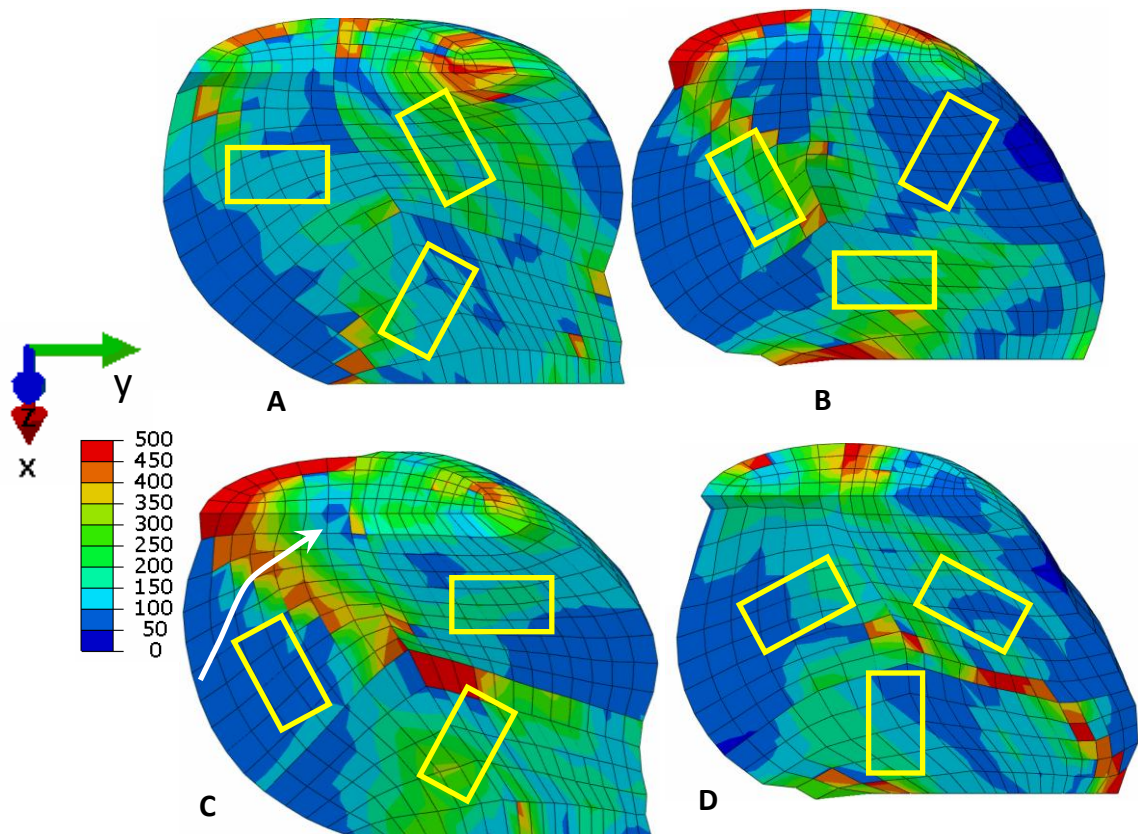
Figure 5.10 .Shear deformation to a simple shear strain of 0.42 where slip systems 9 <101]{10-1} and 10 <211]{-101) are suppressed to be more consistent with experimental observations (Zhou et.al (2009). Differential strains at the grain boundary on the right are evident in orientation sets A and C (compare with Figure 2.6)
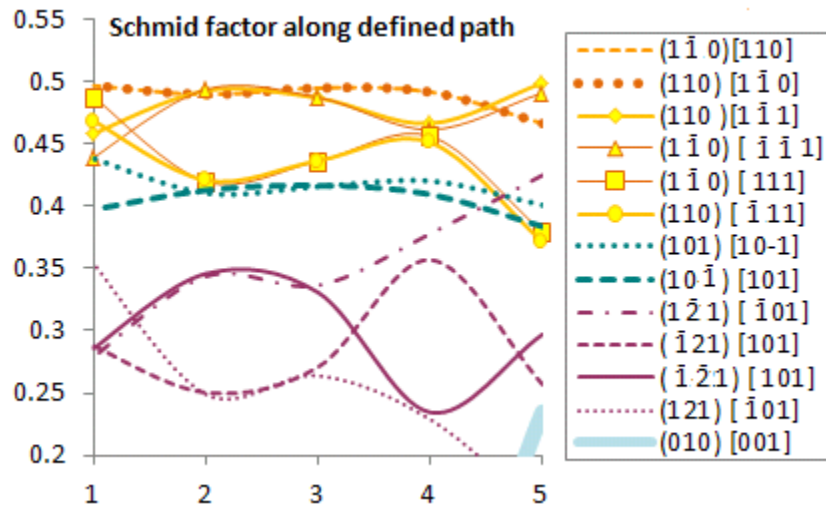
Figure 5.11 The generalized Schimd factor (computed from the stress tensor in each element) varies substantially with the crystal orientation in the elements along the line in the upper left grain orientation in orientation set C in Figure 5.10. Slip system 4<111>{110) has the greatest resolved shear stress and is greater than on suppressed slip systems 9, <101]{10-1), and 10 <-101]{121).

5.4 Summary

Crystal features such as special morphology as well as anisotropy present in lead free tin based solder joints have significant effects on the mechanical properties of sub-mm solder joints. CPFE models can solve the mechanical problems under complicated external and internal constraints imposed by grain morphology. In this study the effects of both anisotropy and grain morphology are examined using a very simple phenomenological constitutive model. Hardening behavior based upon information in the literature was used to simulate several different geometrical morphologies with different crystal orientations (Table 1.1). Comparison of tri-crystals with different permuted sets of orientations shows that the activity of slip systems depends on both position and orientations of neighboring grains. The simulations showed deformation characteristics similar to experimental observations when less facile slip systems were suppressed. For example, shear bands and orientation gradients are observed in von-Mises stress contours and Schmid factor calculations. While the qualitative behavior of the model is realistic, further improvements to the model require optimization based upon direct comparison with well characterized specific experiments.

CHAPTER 6

CRYSTAL PLASTICITY FINITE ELEMENT STUDY OF DEFORMATION BEHAVIOR IN COMMONLY OBSERVED MICROSTRUCTURES IN LEAD FREE SOLDER JOINTS

As it was discussed in chapter 2, the strongly anisotropic elastic modulus and coefficient of thermal expansion (CTE) play an important role in thermo-mechanical loading of solder joints, leading to complex heterogeneous stress states acting on joints [Bieler et. al (2008)]. Due to this anisotropy, crystal features such as grain size and grain morphology have significant effects on the mechanical properties and reliability of sub-mm scale joints. There are very few prior studies about modeling the real microstructure in lead free solders. Park et al. (2008) used an anisotropic linear elastic constitutive model in an FEM simulation to simulate three-dimensional elastic strains measured experimentally in lead-free solder balls. Although they could predict the location of damage near the grain boundary, the observation of plastic deformation by Bieler et al. (2012) in the samples that experience thermo-mechanical loading suggests that application of more sophisticated plastic constitutive models are required for prediction of damage evolution in lead free solders that fail by ductile fracture caused by plastic deformation.

More recently, Maleki et al. (2013) used a J2 plasticity constitutive model to investigate the effect of aging conditions on deformation behavior of the eutectic micro-constituent in SnAgCu lead-free solder. Although their study accurately modeled the geometry of Sn grains and intermetallic, the isotropic plasticity associated with J2 model is unrealistic and oversimplified.

Darbandi et al. (2013) used a crystal plasticity model to investigate the effect of grain orientation and its relationship with morphology (grain position within a simplified geometry of solder ball microstructure). Specifically, this study investigated the complex interaction between the

activity of slip systems, location of a particular grain within the solder ball and orientation of different grains.

Miniaturization is a very important issue in solder joints because the dimension of a joint is similar to the size of the Sn grains. The design of solder joints will increasingly require considering the grain scale anisotropy. Since the damage evolution highly depends on stress, strain, and the activity of slip systems, providing a model that can predict the local stress and strain state will be helpful from both a scientific and industrial point of view. Furthermore, the use of a microstructure scale FE mesh in a crystal plasticity finite element (CPFE) model is also important for interpreting experimental measurements, because at these scales experimental boundary conditions are very difficult to measure or monitor.

In this study, a CPFE model is used to account for deformation mechanisms of, and anisotropy associated with the slip phenomena in Sn to compare with corresponding experimental characterization of shear deformation, to assess the capability of the CPFE model to predict the kinematics of plastic deformation and evolution of microstructural features in different solder joints. Firstly, two different single crystal orientations were investigated to evaluate the capability of CPFE to predict the kinematic plastic deformation. Next, the beach-ball microstructure which is commonly observed in lead free solder was investigated, in two different samples to evaluate the reliability of CPFE model to predict the plastic deformation in lead free solders. Thus, this work provides a basis for an integrated incremental model development strategy based upon experiments, modeling and comparative analysis.

Four specially prepared samples of a 4×4 ball grid array (BGA) were cut from a 15 mm x 15 mm body-size plastic ball grid array (PBGA) package with Sn-3.0Ag-0.5Cu (wt.%) solder joints. The solder joints were approximately 0.5 mm in diameter. The samples were aged at 100°C for

500 hours, sectioned, and carefully polished (without metallurgical mounting) so that the plane of shear at the center of the joint could be observed on one set of four balls. A fixture shown in Figure 6.1 was used to impose a shear strain, so that evidence of local strain effects could be detected topographically by small variations in out-of-plane shear on the previously polished surface.

Optical microscopy, analysis of polarized light microscopy, and orientation imaging microscopy[TM] (OIM), were conducted initially, and after the deformation. To permit accurate orientation measurements, samples were lightly re-polished after the deformation to improve surface smoothness. The resin in the package and board were carefully painted with carbon paint to cover non-conducting surfaces. Also, copper tape was used to provide a conductive path to prevent the charging that causes image distortion.

OIM data were obtained using a CamScan 44FE electron microscope. The accelerating voltage was 20 kV and the working distance was 33 mm. A TSL EDAX OIM system with a digiview SEM detector was utilized to generate the orientation maps. Maps were cleaned up using the neighbor confidence index (CI) correlation to replace pixels that had low CI with their neighbors having a high CI. This step is required to remove the minority data points coming from un-indexed or wrongly indexed pixels, typically arising from intermetallic phases, which were not considered in this work. A user defined crystal orientation map was employed to correlate the orientation of the Sn c-axis with respect to solder/package interface. For this orientation map 5 colors (Purple-blue-green-yellow-red) were used to represent the orientation of the c-axis with respect to the solder/package interface. When the c-axis is on the interface plane, the orientation is expressed as "red", and when the c-axis is perpendicular to the surface the orientation is "purple". Other colors (blue, green and yellow) fill the rest of the c-axis orientation space.
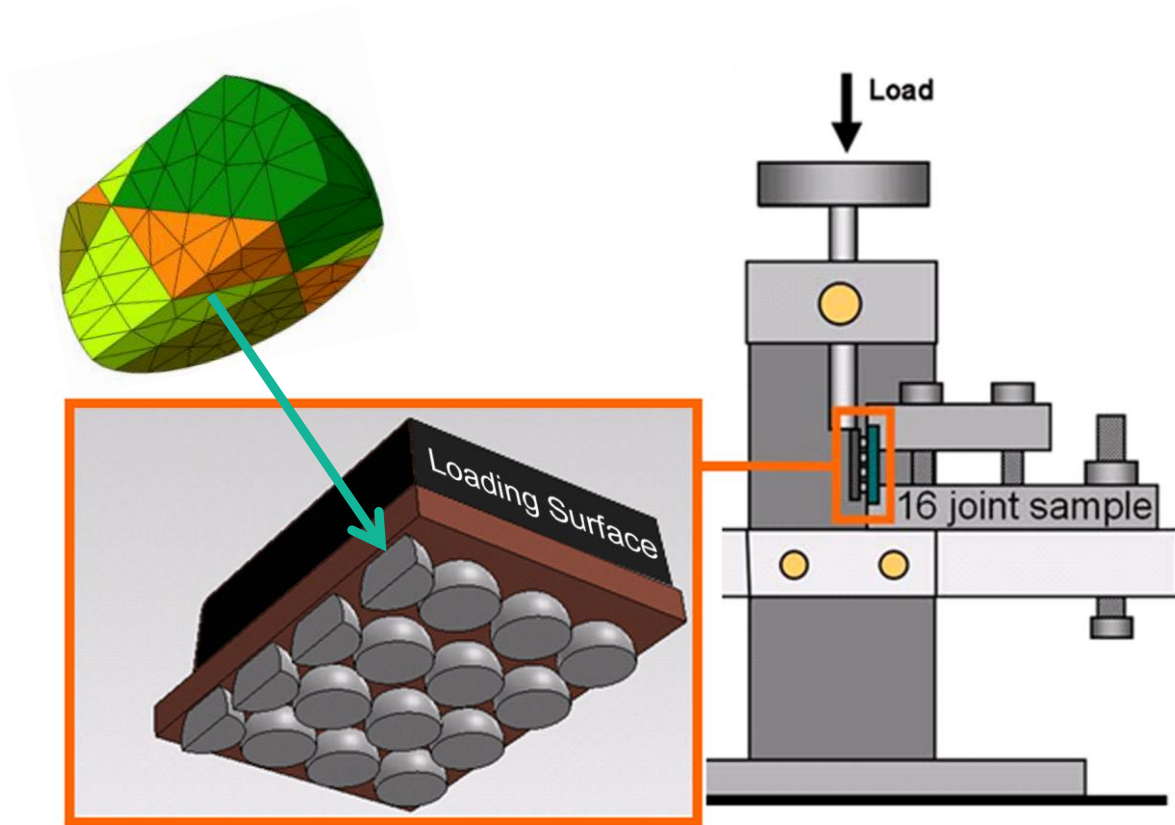
Figure.6.1 Schematic diagrams of a 3-D visualization of the CPFE mesh located in a 4×4 solder joint array sectioned from a PBGA package. The solder ball assembly geometry and shear test apparatus is also shown.

The finite element analysis was performed on four samples using the commercial finite element code ABAQUS. The crystal plasticity material model was implemented using a user material subroutine in FORTRAN (VUMAT). Details of the model can be found in Darbandi et al. (2013). The joints were modeled as asymmetrically truncated spheres to correspond with measured cross sections. Element types and number of elements used are described in captions of relevant figures. The material parameters used are shown in Tables 5.1 and 5.3.

A 3-D visualization of the CPFE mesh is presented in Figure 6.1, showing the position of one of the joints analyzed with respect to the rest of the package.

Two different single crystal joints (Figures 6.2-6.4) and two different beach ball morphology joints (Figures 6.5-6.7) were studied to investigate the capability of CPFE to model the kinematics of deformation and microstructural features. The two single crystals were subjected to 0.65 mm displacement. One of the beach-ball solder balls was subjected to 0.1mm shear displacement, and the second one was displaced by 0.4 mm.

In order to reconstruct the real microstructure of a joint with beach ball morphology from OIM and polarized light microscopy measurements, one can assume that the beach ball microstructure is part of a sphere that is equally divided by three planes into six parts with the same volume. Due to the fact that the beach ball microstructure can be produced by 60° rotations about an <a> axis, the cutting plane can be assumed to be a plane with its normal parallel to a common <100} <a> axis. This modeling method allows the morphology to be correlated appropriately with crystal orientations. (The morphology obtained using the polarized light microscopy is not sufficient to reconstruct the microstructure because it does not give the orientation of the common <a> axis required to determine the geometrical inclination of the grain boundary through the depth of the solder balls).

6.1. Modeling of single crystal solder balls using CPFE

Figure 6.2(a, b) shows two different undeformed single crystal joints. The crystal orientations overlaid on the figures in (c, d) show that the c-axis is nearly parallel to the interface according to the c-axis color code. While both of these joints have a 'red' orientation, the c-axis direction differs with respect to the plane of shear. (The top of the map in both joints is exaggerated in the vertical direction due to the topographic effects of the polish and the 70° tilt of the sample during the measurement). The optical images in Figure 6.2(e, f) show that deformation was concentrated in the upper part of the joint, where the cross sectional area was the smallest. The OIM maps for the samples after deformation in Figure 6.2 (g, h) show that the orientation of the c-axis with respect to the interface did not change much (same color), but rotation is observed in both samples about the c-axis, especially in the highly deformed area near the top.

In both joint orientations, the crystal rotated about the c-axis in the direction of shear about an axis near the [001] direction. In Figure 6.2(g), the c-axis is inclined to the plane of shear, and the rotation axis is close to the c-axis. In Figure 6.2(h), the c-axis rotation axis is nearly perpendicular to the plane of shear. In both cases, modest rotations about an axis near (001) imply that slip on the (110) plane is facile and stable.

For the simulation, optical micrographs (Figures 6.2(a, b)) were used to define the geometry for CPFE analysis. The initial orientations were used to establish the basis for the kinematics of plastic deformation (Figure 6.2 (c, d)). The simulations also show that large amounts of deformation took place in the upper right area indicating the localization of plastic deformation in these regions in Figure 6.3. The deformation simulated by the CPFE model compared closely to the deformed shapes observed in the optical microscopy micrographs. This shows that the
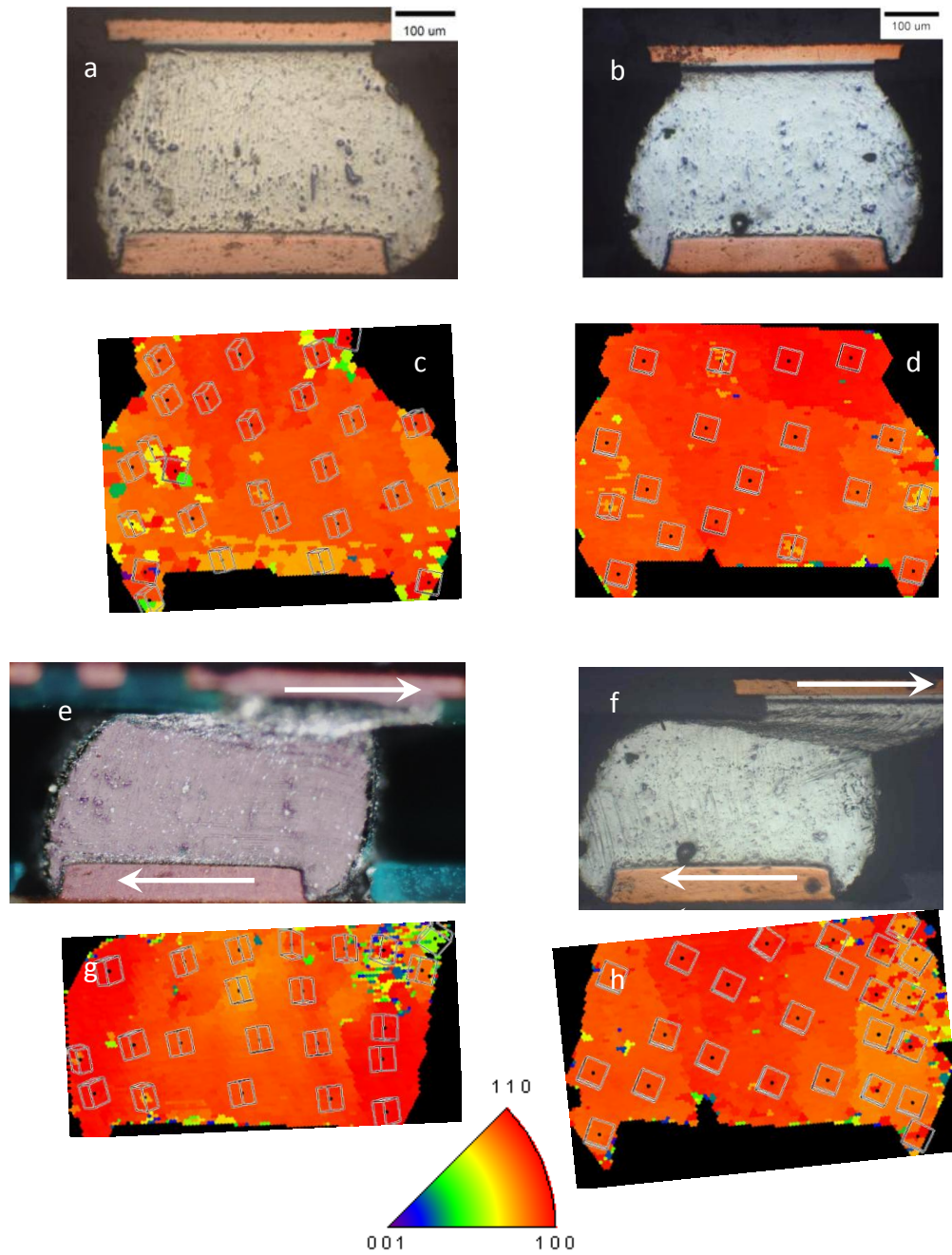
Figure 6.2 Optical micrographs of 2 different solder balls with corresponding c-axis orientation maps with respect to the substrate normal direction, before (a-d) and after (e-h) 0.65 mm shear displacement. After shear, strains are concentrated in upper right regions. The c-axis orientation was retained (no color change) as the crystal rotated about the c-axis (note overlaid unit cell prisms) it during shear.
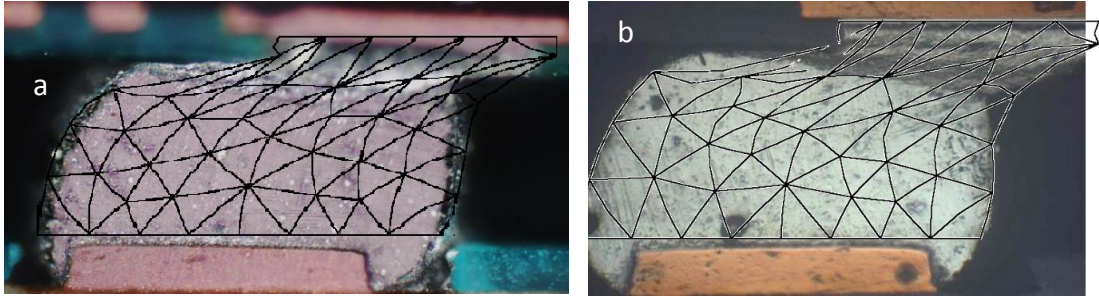
Figure.6.3. Comparison of simulation and experimental results for single crystal deformed solder joints illustrated in Figure 6.2. 565 C3D10M elements were used in (a) and 569 C3D10M elements were used in (b).

crystal plasticity model can accurately predict the kinematics of plastic deformation due to the shear loading.

Figure 6.4 shows the surface features on the previously polished surface of the joint in Figure 6.3(b). The micrograph shows different plane traces on the sample surface in different locations. Using plane trace analysis based upon local orientations measured after deformation (details in Zhou et al.(2009)), slip on {110)* planes is dominant, The complimentary shear strains required for shear deformation are apparent in the perpendicular {110) slip traces. The highest Schmid factors (*m*, based upon a pure shear stress assumption) are for slip in <110] directions, but they are also high for slip in <111> directions. The most active slip systems in the simulation in Figure 6. 4(b) also indicates that the most active slip systems are those with high Schmid factors.

To assess the most active slip systems from experimental measurements, rotation axes can indicate which of the four slip directions on a {110) plane was the most active using the orientation map data in Figure 6.2(d,h). The rotation axes were determined between the initial and final orientations in nine locations evenly distributed in a 3x3 grid (after correcting for the sample alignment in the measurements). In each of the nine locations, the rotation angle was 5.4°, about an average rotation axis of <-15±4.5 -6.5±3.7 100]. This is an average of 5.4±4° from the <-15 -15 100] rotation axis that is 90° from the {1-10)<111] slip plane normal and slip directions. As the <-15 -15 100 axis is 21° from the [001] axis, the measured rotation axes are much closer to the expected rotation axes for <111> slip than the [001] rotation axis for <110] slip (these vectors are illustrated in Figure 6.4(b)). This indicates that the <111> slip system is much more active than the <110] slip direction. Furthermore this indicates that one of the <111> directions is strongly favored, because equal amounts of slip in the two <111> directions in the

* Mixed {) and <] for planes and directions recognize the symmetry of the tetragonal crystal structure.
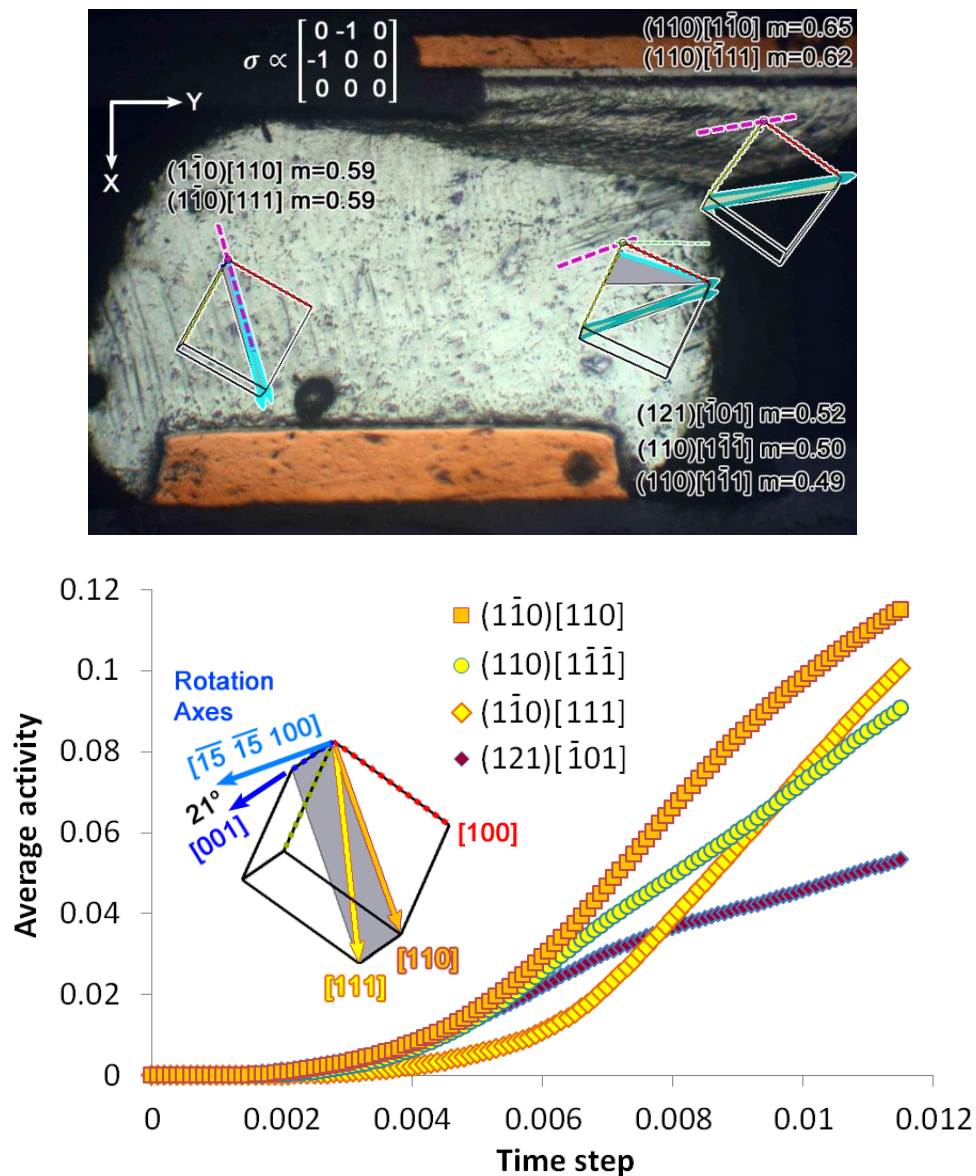
Figure 6.4   (a) Optical image of joint b in Figures 6.2 and 6.3, showing local unit cell orientations with shaded slip planes and corresponding plane traces, and slip vectors (blue lines) with high Schmid factors (there is some evidence for (121) slip in the highly sheared upper right part of the joint). Red and yellow-green edges of the unit cells represent the crystal x and y axes, respectively. (b) Comparison of the average activity in the simulation of the four most active slip systems at each integration point in the single crystal joint.

103

same {110) plane will give the equivalent of <110] slip. Figure 6.4(b) shows the average amount of shear on the four most active slip systems obtained from CPFE model (which is based on the average initial orientation).   This simulation shows that (1-10)[110] slip is dominant, which is not what the experiment shows, but this is a consequence of no significant difference in the initial slip resistance on the various slip systems used in the simple material model used . This experiment and others like it will lead to future refinements in the model. Nevertheless, even this overly simple material model is able to effectively capture the kinematics of deformation.

6.2. Modeling of heterogeneous plastic deformation in Beach-ball microstructure of solder joints
In order to simulate the behavior of solder balls in different locations and at different stages of thermo-cycling in a real ball grid array package, the behavior of solder balls subjected to both small and large shear displacements have been investigated. From examination of incremental strains resulting from small to larger shear displacements, it is apparent that orientations near the center of the ball do not change very much, so the final orientation in the central area can be used as a good approximation for the initial crystal orientation. This allows analytical comparison with prior characterization studies where grain orientations were characterized only after the deformation. Two cases are presented: the first, where the orientation was measured before and after a small shear displacement (Figures 6.5 and 6.6), and second, a sample characterized in prior work where solid modeling of the beach ball and sectioning based upon orientations in the center of the deformed sample were used to identify a highly probable initial microstructure condition (Figures 6.5 and 6.7).
Figure 6.5 shows the measured tricrystal orientations in pole figures, and the microstructure, mesh, and deformed mesh for the two joint samples studied. The c-axis OIM map for a beach ball sample before and after 0.1 mm shear displacement is shown in Figure 6.6 (a,b).   A
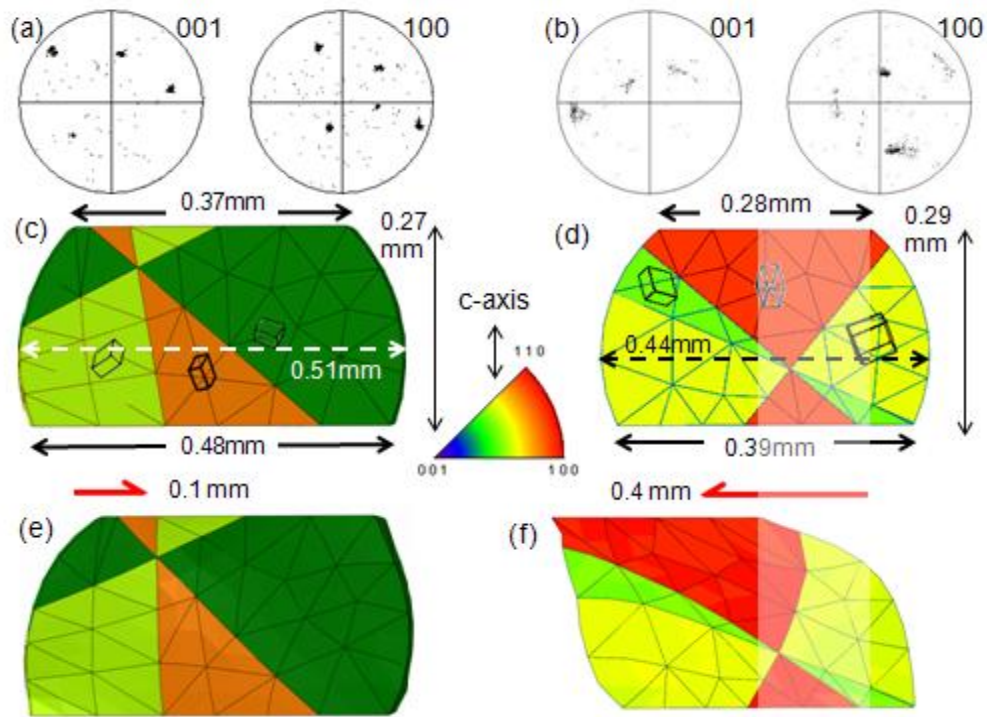
Figure 6.5 Pole figures obtained from OIM for two solder joints with beach ball microstructure (a, b), FE meshes colored according to the c-axis color scale in the vertical direction before deformation (c, d) and after deformation, (e, f) showing shape after indicated displacements were imposed and released. 2550 C3D10M elements were used in (c, e) and 2600 C3D10M elements were used in (d, f).
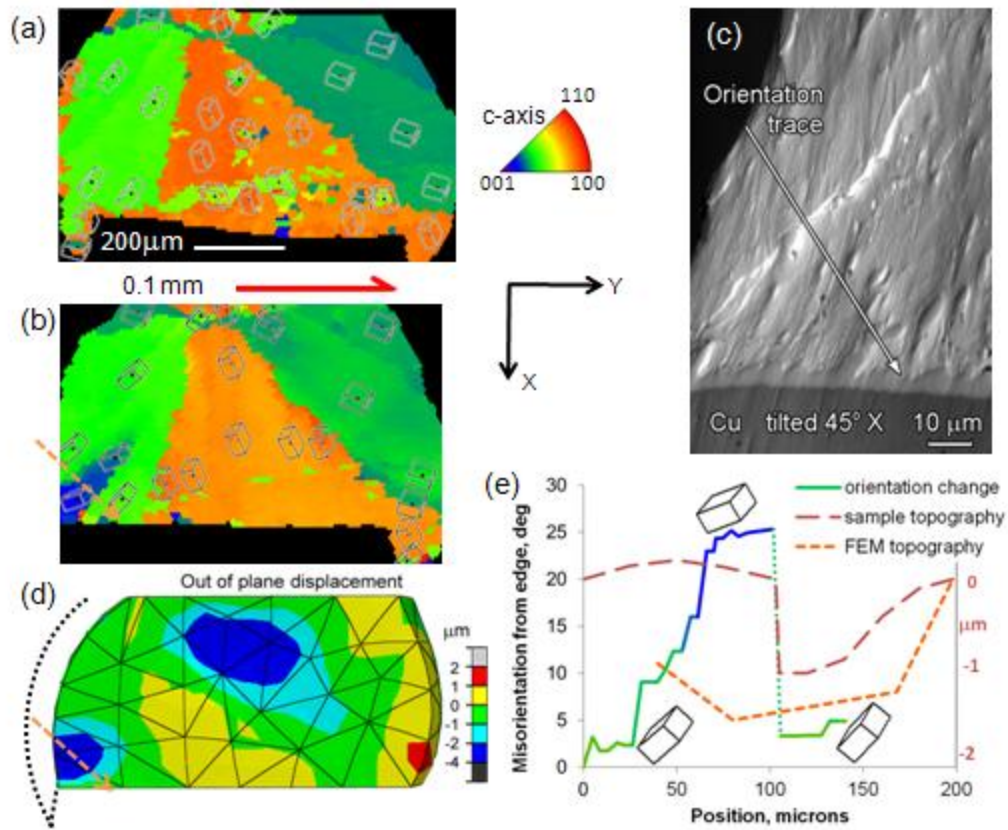
Figure.6.6 (a) X direction c-axis orientation maps for beach ball microstructure before deformation and, (b) after 0.1mm shear, backscattered SEM image tilted -45° about X axis showing a ledge in the lower left area (c), and a path along which misorientation and topography are traced in the experiment (b). A similar trace in the CPFE simulation (d), is plotted with experimental data in (e). The CPFE model is geometrically simpler and does not include the material indicated by the dotted line in (d), but it is able to semi-quantitatively capture the localized deformation observed experimentally in the lower left corner.
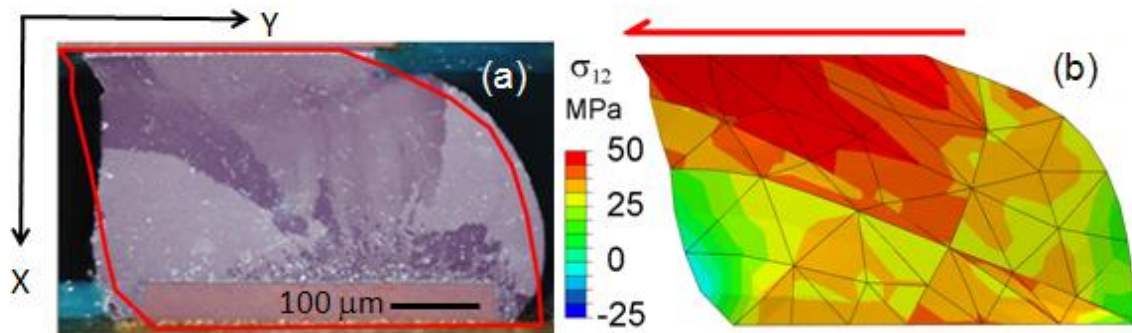
Figure.6.7. Polarized light micrograph (a) of beach ball microstructure that experienced a large shear displacement of 0.4 mm (red line), deformed solder ball predicted by CPFE illustrating distribution of shear stress in the 1-2 plane indicating a higher stress due to more shear localization in the upper area.

comparison of the c-axis map before and after deformation reveals the most noteworthy change to take place in the crystal orientation due to localized plastic deformation in the lower left corner of the c-axis map. In this area, the orientation color changed from green to blue, as made evident by overlaid prisms. A corresponding backscattered electron micrograph in Figure 6.6(c) indicates the formation of a ledge in the lower left corner area, where significant local orientation changes were measured with OIM. The image of the surface in Figure 6.6(c) is tilted so that it makes the ledge easier to see. The tilted image was one of a stereo pair from which it was possible to prove that the material to the right of the ledge was at a lower elevation than the material to the left.

Figure 6.6(e) illustrates the change in surface topography obtained using the CPFE analysis. It is apparent that the CPFE model was able to predict a negative displacement from strain localization similar to what happened in the real experiment. Figure 6.6(e) compares the orientation and topography along a diagonal path that crosses the region where the topographic

107

features were observed (diagonal lines in Figures 6.5(d, c)). As shown in Figure 6.6 (e), the crystal orientation changed along this path by about 25° from the outer edge of the sample, and the surface elevation dropped by 1 micron at the ledge, and then came back up to the original height at the copper interface. The path in the CPFE simulation also shows a similar trend, though the large size of the elements makes for a rough representation of the topography. Also, because the CPFE model was geometrically simpler, without modeling the shape of the Cu pad around which the solder flowed, the experimental geometry has more solder in the perimeter region. However, when the trace covers similar paths with respect to the corner of the copper pad, the surface topography from the CPFE matches the experimental trends reasonably closely (noting that a ledge cannot be predicted by the model).

Figure 6.7 shows a simulation of the microstructure of a different deformed sample for which the initial condition was not measured. With computational deformation, the distribution of strain is quite similar to the observed strain in the real microstructure. The differences in shape made evident by overlaying the shape of the CPFE model on the experimentally deformed sample may arise from the fact that initial solder joints are not always perfect truncated spheres (that were modeled), so it is not possible to assess the differences between the model and the experiment quantitatively. In particular, the localization of shear strain in the upper grain, which is a "red" orientation (where the orientation of the c-axis is parallel to the interface) shows consistency with the real microstructure where the greatest amount of shear occurs in the "red" orientation. This is an outcome of slip along the c-axis, which is known to be a facile slip system (Bieler et. al (2012)).

6.3. Summary

In this chapter, the capability of CPFE modeling was examined using shear deformation applied on real microstructures of SAC305 solder balls. The simulation results clearly show the capability of crystal plasticity model to predict the heterogeneous strain that is observed in correlated physical samples. The models used estimates of material properties that are considered to be reasonable based upon limited prior study of slip behavior in Sn. In addition to the kinematics of plastic deformation, more details can be predicted using this model, such as accurate prediction of some of the microstructural features such as formation of ledges as well as activity of slip systems. Therefore, this model can be used as a useful tool to predict damage, as the damage phenomena is controlled by the plastic deformation, and it can be further refined with constraints obtained by detailed comparisons with experimental data.

CHAPTER 7

SLIP SYSTEM ACTIVITIES OF SAC305 SOLDER BALLS UNDERGOING SIMPLE SHEAR DEFORMATION

As discussed in chapter 2, since the anisotropy in plastic deformation emerges naturally from the activity of slip systems, and due to the fact that plastic deformation is the main mechanism responsible for fracture in ductile metals in different strain rates and temperatures, understanding of the relative activity of different slip provides valuable insights into the inhomogeneous deformation of interconnections in electronic industry. It also can help us to develop more reliable modeling tools based on crystal plasticity finite element modeling.

A review about the plastic properties of tin by Yang and Li (2007) indicates the need for better understanding of the deformation mechanisms of tin. There is incomplete understanding of slip in Sn, though single crystals have been investigated by several researchers. There is especially uncertainty about the critical resolved shear stress for different slip systems. Evidence presented by Düzgün et al. (1999, 2003) suggests that the initial critical shear stress is similar on different slip systems, but they have different rates of hardening. In these studies, a limited set of crystal orientations have been investigated using tensile tests, and also the effect of alloying and strain rate were not considered. **Table 2-1** presents an estimate of the relative ease of activating the 10 relevant slip systems based upon an assessment from literature data. This table which was developed by Fujiwara and Hirokawa (1987) based upon the etch-pit / hillock study is not extensive. In addition to this method, other researchers (Matin et al. (2006) and Sidhu and Chalwa (2008)) defined a parameter called "effective yield strength" which is the value of critical resolved shear stress over the Schmid factor for different slip systems. In this study, the authors used values of the critical resolved shear stress of pure tin, which can be different from

SAC305 due to the effect of alloying elements. Friedel (1964) and Labusch (1970) showed that the critical resolved shear stress increases with alloying elements. However, for certain slip systems some assumptions based on the linear atomic density were made to calculate the critical resolved shear stress, which are not experimentally validated.

Kinoshita et al. (2012) recently used the first-principles density functional theory to study the activity of slip systems in pure tin. They used the ideal shear resistance for calculation of the critical resolved shear stress. They employed a tensile test study to assess the activity of different slip systems and investigated the effect of crystal orientation on relative activity of slip systems. Zhou et al. (2009) used a methodology based on the OIM and calculating the Schmid factor together with partially observing slip traces to assess the activity of slip systems on shear deformed samples. Their study implied that slip in [001] and [111] directions is likely, and slip on (010)[101] may contribute significantly.

In this chapter the activity of slip systems has been discussed using the shear test studies on lead free solder joints in different orientations by applying shear deformation in three separate steps. OIM and SEM were utilized to understand how the crystal rotates during the plastic deformation after each deformation step.

In addition, using optical microscopy and polarized light microscopy, plane traces were analyzed to understand the activity of slip systems. Thirty two solder balls were analyzed to provide enough information to sort out the slip systems in terms of activity. Also, the activities of slip systems were categorized based on the crystal orientation, in order to show the effect of the crystal orientation on facilitating the operation in different slip systems.

7.1. Experimental procedures

Eight specially prepared samples of a 4×4 ball grid array (BGA) were cut from a 15 mm x 15 mm body-size plastic ball grid array (PBGA) package with Sn-3.0Al-0.5Cu (wt.%) solder joints. Four (4) samples were aged at 100°C for 500 hours. The samples were sectioned and carefully polished so that the plane of shear at the center of the joint could be observed on one set of four balls before and after shear displacements.

Due to the path dependency of plasticity, the total displacements were applied in three separate steps in order to obtain the information about crystal rotation during the shear deformation. A fixture was used to impose a two-dimensional shear strain, so that small variations out of the plane of shear resulting from local strain effects could be detected topographically on the previously polished surface. The loading conditions and pre-aging history of each sample is reported in Table 7.1. Figure 4.4 shows the schematic of the apparatus which was utilized in this experiment. To permit accurate orientation measurements, samples were lightly repolished to improve surface cleanliness. Optical microscopy, analysis of polarized light microscopy, orientation imaging microscopy (OIM) and SEM were conducted initially and before and after each deformation step. The resin surrounding the balls and the package was carefully painted with carbon paint to cover the non-conducting surfaces. Also samples were covered by the copper tape to provide a conductive path and to prevent the charging effect which causes image distortion.

OIM data were obtained in a CamScan 44FE electron microscope. The accelerating voltage was set to be 20 Kv and the working distance was 33 mm. A TSL EDAX system with digiview SEM detector was utilized. Acquisition speed of 15- 20 points per second was obtained using 2×2 binning setting. In order to generate the orientation maps, EDAX TSL OIM Analysis software

112

Table 7.1 Test conditions for performing the simple shear tests.

Sample	Initial condition	Deformation Temperature	Displacement(mm)		
			Step-1	Step-2	Step-3
1	Aged	Room Temperature	0.1	0.45	0.72
2	Aged	100°C	0.1	0.25	0.28
3	Aged	Room Temperature	0.1	0.45	0.62
4	Aged	100°C	0.1	0.25	0.41
5	Non-Aged	Room Temperature	0.1	0.45	0.83
6	Non-Aged	100°C	0.1	0.42	0.64
7	Non-Aged	Room Temperature	0.1	0.55	0.7
8	Non-Aged	100°C	0.1	0.35	0.58

was employed. Maps were cleaned up using the neighbor confidence index (CI) correlation to replace pixels that had low CI with their neighbors having a high CI. This step is required to remove the minority data points coming from un-indexed or wrongly indexed patterns. In the neighbor-confidence-index-correlation method, a datum point having low CI is replaced with neighboring points that have the highest CI value. In the presentation of results, Sn unit cells were overlaid on OIM maps.

A user defined orientation map was employed to correlate the orientation of Sn c-axis [001] with respect to solder/package interface. For this orientation map, 5 colors (Purple-blue-green-yellow-red) were used to represent the orientation of the c-axis with respect to the solder/package

interface. When the c-axis is on the interface plane the orientation is expressed as "red", while when the c-axis is perpendicular to the surface the orientation is "purple". Other colors (blue, green and yellow) fill the rest of the orientation space.

7.2. Slip-trace analysis and Schmid factor calculation

Activity of slip systems can be correlated with microstructure and grain orientation using calculation of Schmid factor and plane trace analysis. One can represent the crystal orientation using three (Bunge) Euler angles φ_1, ϕ, φ_2.

Using the concept of the rotation matrix (g) in linear algebra, three basic rotation matrices rotate vectors about the x, y, or z axis to be able to relate the crystal coordinate system to the global coordinate system using the definition of Euler angles defined by Bunge (1982) as follows:

$$g_{\varphi_1} = \begin{bmatrix} \cos\varphi_1 & -\sin\varphi_1 & 0 \\ \sin\varphi_1 & \cos\varphi_1 & 0 \\ 0 & 0 & 1 \end{bmatrix} \tag{7.1}$$

$$g_{\phi} = \begin{bmatrix} 1 & 0 & 0 \\ 0 & \cos\phi & -\sin\phi \\ 0 & \sin\phi & \cos\phi \end{bmatrix} \tag{7.2}$$

$$g_{\varphi_2} = \begin{bmatrix} \cos\varphi_2 & -\sin\varphi_2 & 0 \\ \sin\varphi_2 & \cos\varphi_2 & 0 \\ 0 & 0 & 1 \end{bmatrix} \tag{7.3}$$

And general rotation matrix can be expresses as:

$$g = g_{\varphi_1} g_\phi g_{\varphi_2} \qquad\qquad\qquad (7.4)$$

The slip plane normal and slip direction can be expressed by Miller indices as (h k l) and [u v w] respectively. Since slip traces are observed using the optical or electron microscopes, the slip plane and direction have to be represented in global coordinate system using the general rotation matrix. Due to the fact that the plane trace is the intersection between a slip plane and the plane of a sample that the trace is observed, plane traces can be calculated as a cross product of slip plane normal (in the global coordinate system) and normal to the sample surface.

Calculation of the Schmid factor depends on the stress definition, but generally this parameter has to be calculated in the local coordinate system. For a particular slip system with the normalized plane normal and slip direction defined respectively as $\hat{n}$ and $\hat{b}$, the Schmid factor can be expressed as:

$$m = \hat{n}\, g^T \sigma g\, \hat{b} \qquad\qquad\qquad (7.5)$$

Evidence for operation of slip systems based on the calculation of Schmid factor can be assessed using optical images and orientation maps.

In order to sort the activity of slip systems, observation of the plane trace and Schmid factor calculation have to be accomplished to rank the slip systems in terms of slip activity. A Matlab program based upon the global stress boundary condition of pure shear was utilized for this purpose.

Figures 7.1 and 7.2 show the load displacement curves for step-2 and step-3 of deformation respectively. It is important to point out that since these curves reflect the hardening of 16 (4×4) solder balls it is not possible to correlate the deformation behavior of each solder to the loading history. As it is apparent, general values of force for a particular displacement are higher for unaged samples. Finer and more intemetallic particles were formed in SAC alloys, and they strengthened the alloys by hindering the movement of dislocation. After aging by coarsening of these particles their efficiency in pining and blocking the dislocations decreases and strength of the solders decreases (Ding et al (2007)). Therefore, it is observed that for aged samples the plastic deformation (non proportionality in the curves) starts at smaller values of displacements in both step-2 and step-3.

On the other hand comparison between figures **7.2 (a), 7.2(b), 7.3(a) and 7.3 (b)** reveals the strong influence of deformation temperature on the hardening of SAC 305 alloys. This impact corresponds to thermally activated phenomena which are more dominant at 100º C.

Figures 7.4 and 7.5 show optical micrographs of aged and unaged shear deformed samples at various deformation steps. Considerable changes in morphology of grains as well as slip plane traces are observed at large plastic deformations (step-2 and step-3). Cross-polarized light images for different shear deformed samples are shown in **7.6 and 7.7.** These micrographs qualitatively show the existence of single crystals or multi-crystals in these sets of samples.

In order to quantify the extent of grain rotation during the plastic deformation one can use the OIM characterization method. To conduct these investigations more effectively one can

116
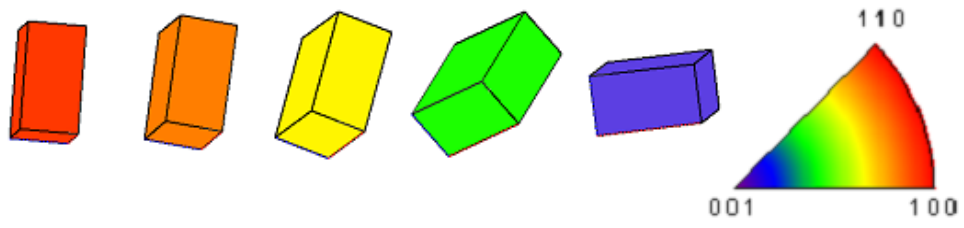
Figure 7.1 Sn grain orientation color code used with OIM c-axis maps to identify the c-axis inclination from the interface.
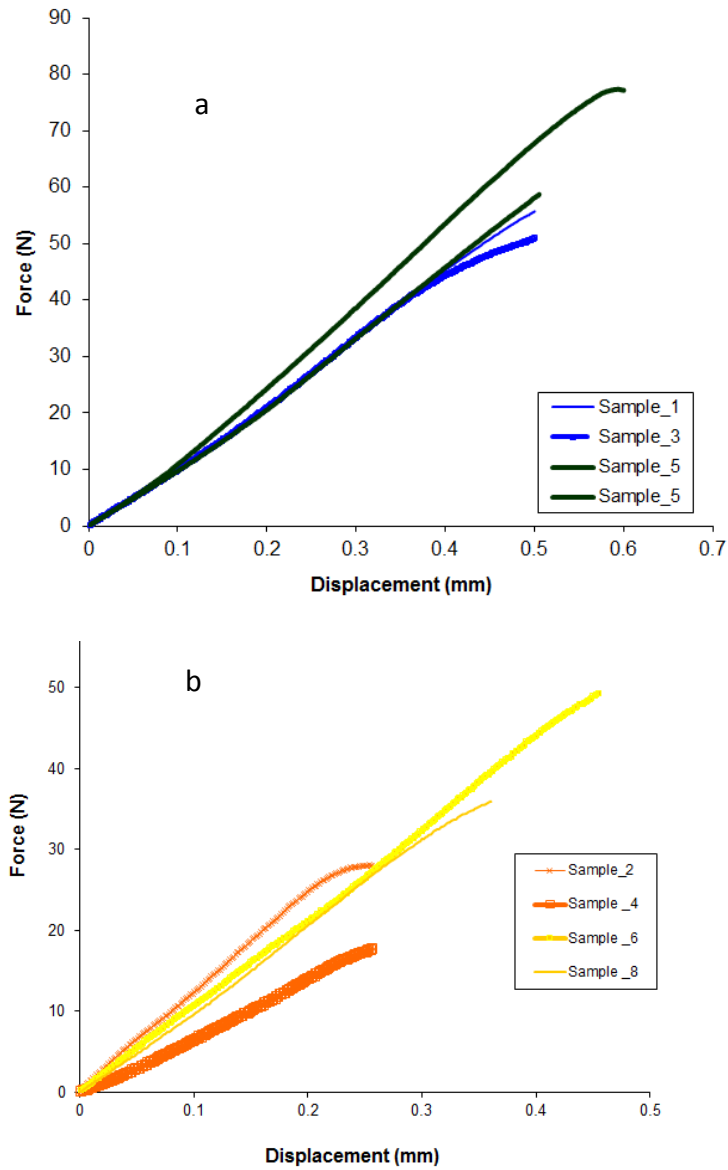
Figure 7.2 Load displacement diagrams for step 2 of shear deformations at (a) room temperature (samples 1 and 3 are aged and samples 5 and 7 are non-aged) for (b) aged samples 100ºC (samples 2 and 4 are aged and samples 6 and 8 are non-aged).
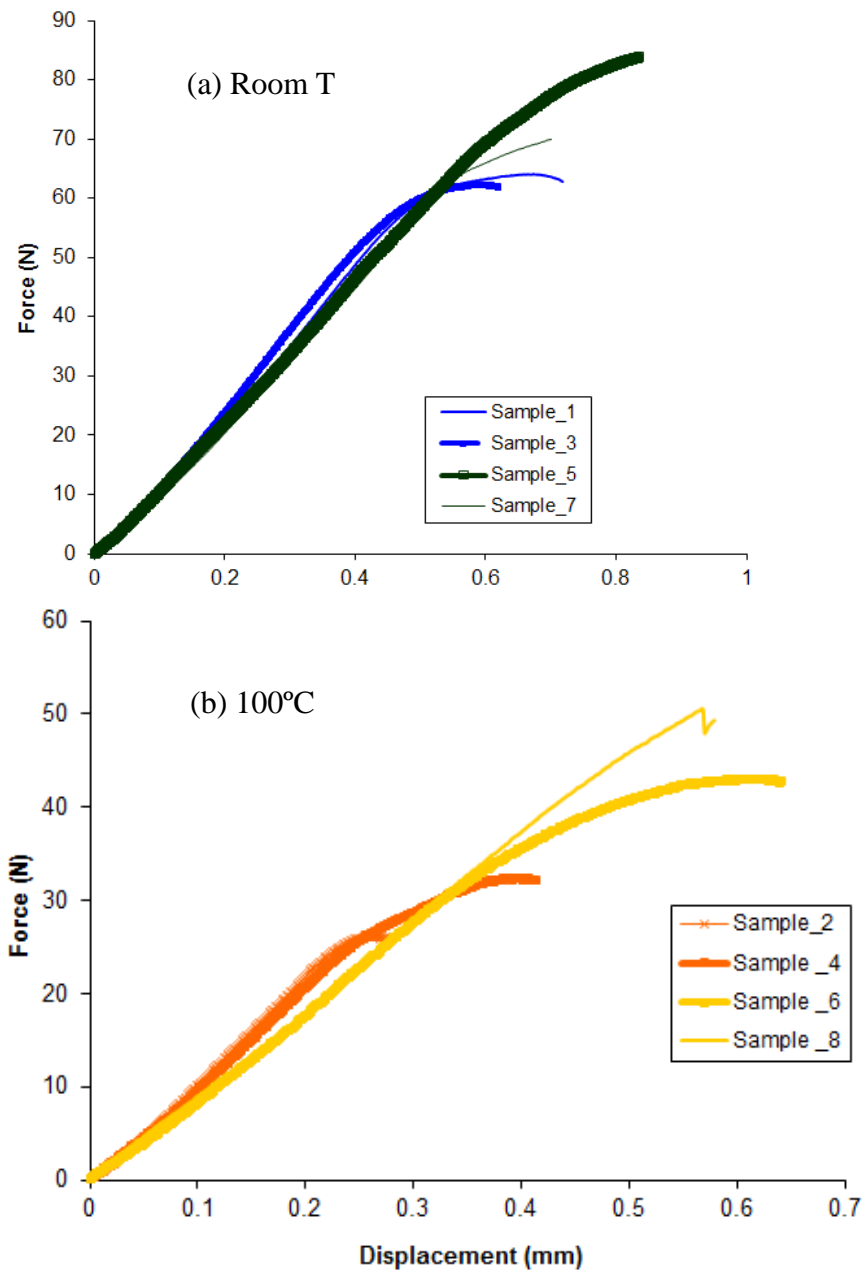
Figure 7.3 Load displacement diagrams for step 3 of shear deformation at (a) room temperature (samples 1 and 3 are aged and samples 5 and 7 are non-aged), and for (b) aged samples 100ºC (samples 2 and 4 are aged and samples 6 and 8 are non-aged).

Figure 7.4 Optical micrographs of 4 cross sectioned samples in in the pre-aged condition, showing the deformation in three steps at room temperature (a,c) and at 100ºC (b,d).

Figure 7.5 Optical micrographs of 4 rows of cross sectioned samples in the unaged condition, showing the effects of deformation in three steps at room temperature (a,c) and at 100°C (b,d).
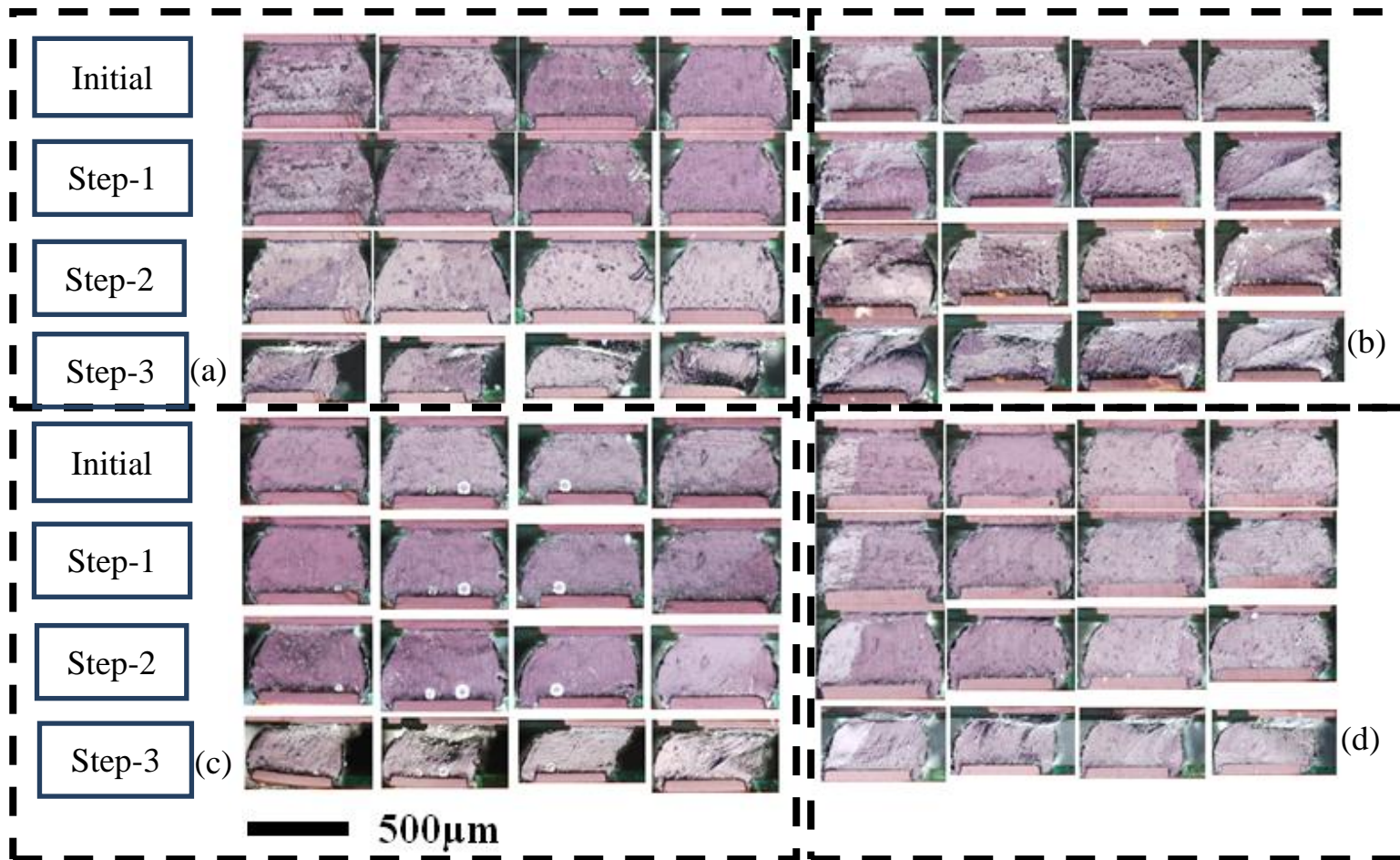
Figure 7.6 PLM micrographs of 4 rows of cross sectioned samples in the pre-aged conditions, showing the effects of deformation in three steps at room temperature (a, c) and at 100°C (b, d).
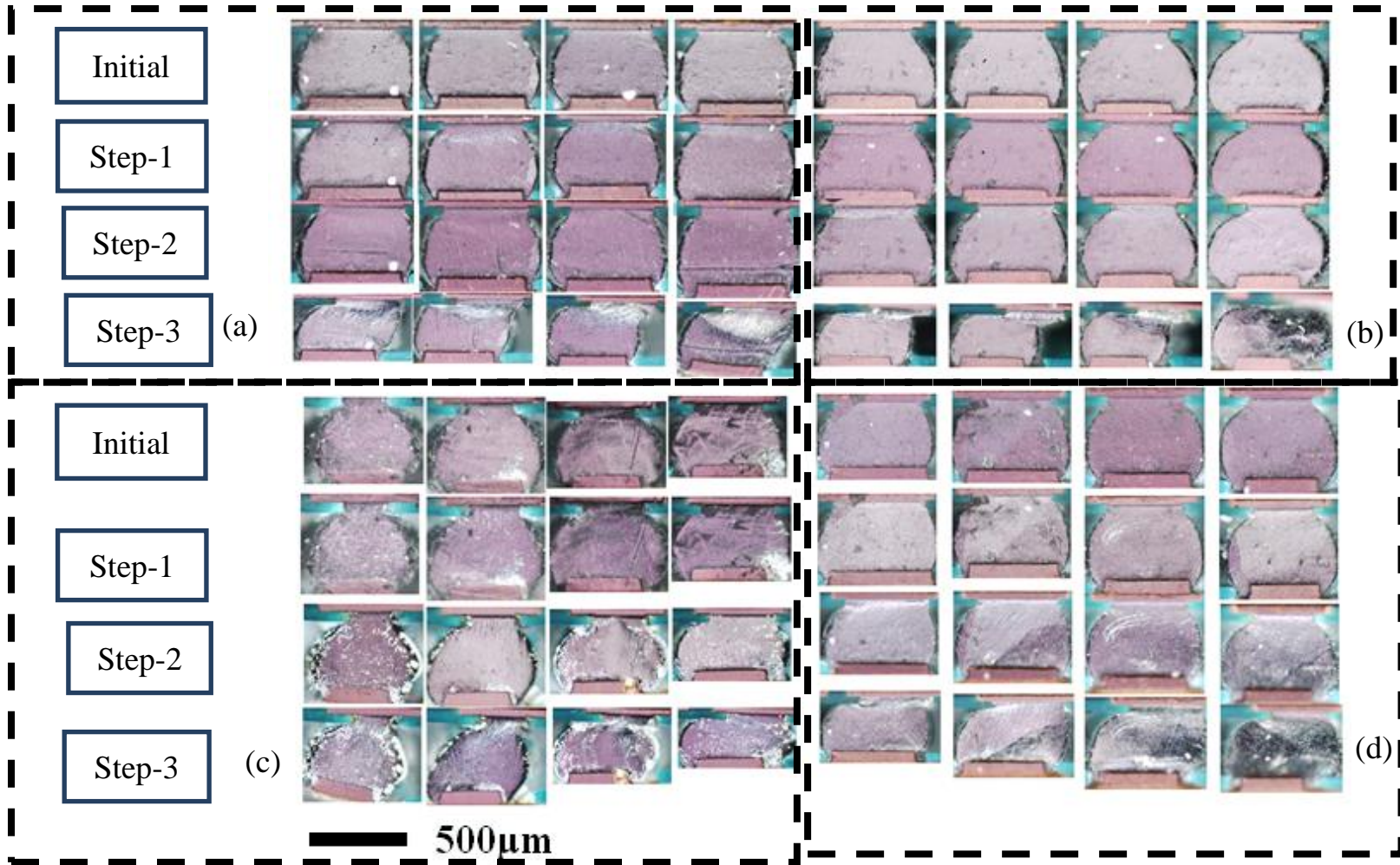
Figure 7.7 Cross-polarized light micrographs of 4 cross sectioned samples in non-aged samples, showing the effects of deformation in three steps at room temperature (a, c) and at 100°C (b, d).

categorize the grain orientation based upon the c-axis maps (as it is illustrated in Figure 7.1). This approach was used to demonstrate evoloution of solders crystal orientations at different steps of deformation for aged and unaged samples by mapping the c-axis based upon the color code which was described in chapter 4 and demonstrated in Figure 7.1. Figures 7.8 and 7.9 show the c-axis maps and evolution of crystal orientations and shape changes at various deformation steps. Due to observation of different single and multi-crystals in terms of c-axis in these set of 32 solder balls, this data set can provide us enough information to conduct a reliable statistical analysis on activity of slip systems.

In order to conduct more accurate examinations, microstructure and Sn grain orientation evolution was observed using a fine scan EBSD map, particularly near the package-solder interface which experienced a higher amount of deformation.

Figure 7.10 shows the optical microscopy, and the c-axis orientation map of a shear deformed solder ball. The c-axis map shows tri-crystals with twinning relationships where two grains intersected with the cutting plane. It is apparent in the optical micrograph that slip happens in neighboring grains and due to the orientation of the grains, two different slip systems contribute to the plastic deformation.

Comparison of calculated slip planes using the Schmid factor with observations of the plane trace on the surfaces of solder balls show that in the left grain (010)[101] (6th mode in Table 2.1) slip system is active. This result is consistent with VPSC simulations conducted by Bieler and
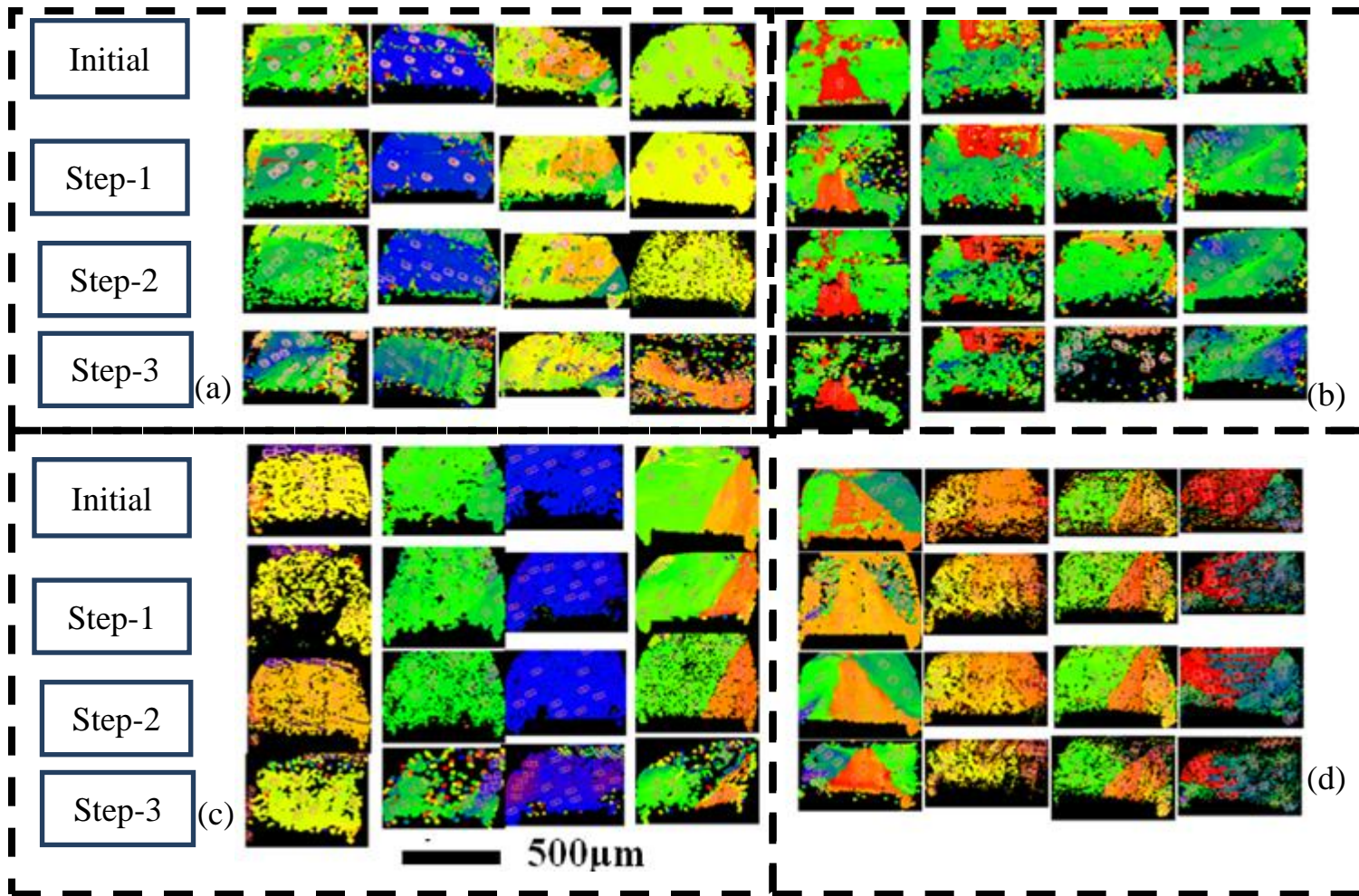
Figure 7.8 C-axis EBSD maps of 4 rows of cross sectioned samples in the pre-aged condition, showing the effect is of deformation in three steps at room temperature (a, c) and at 100°C (b, d).
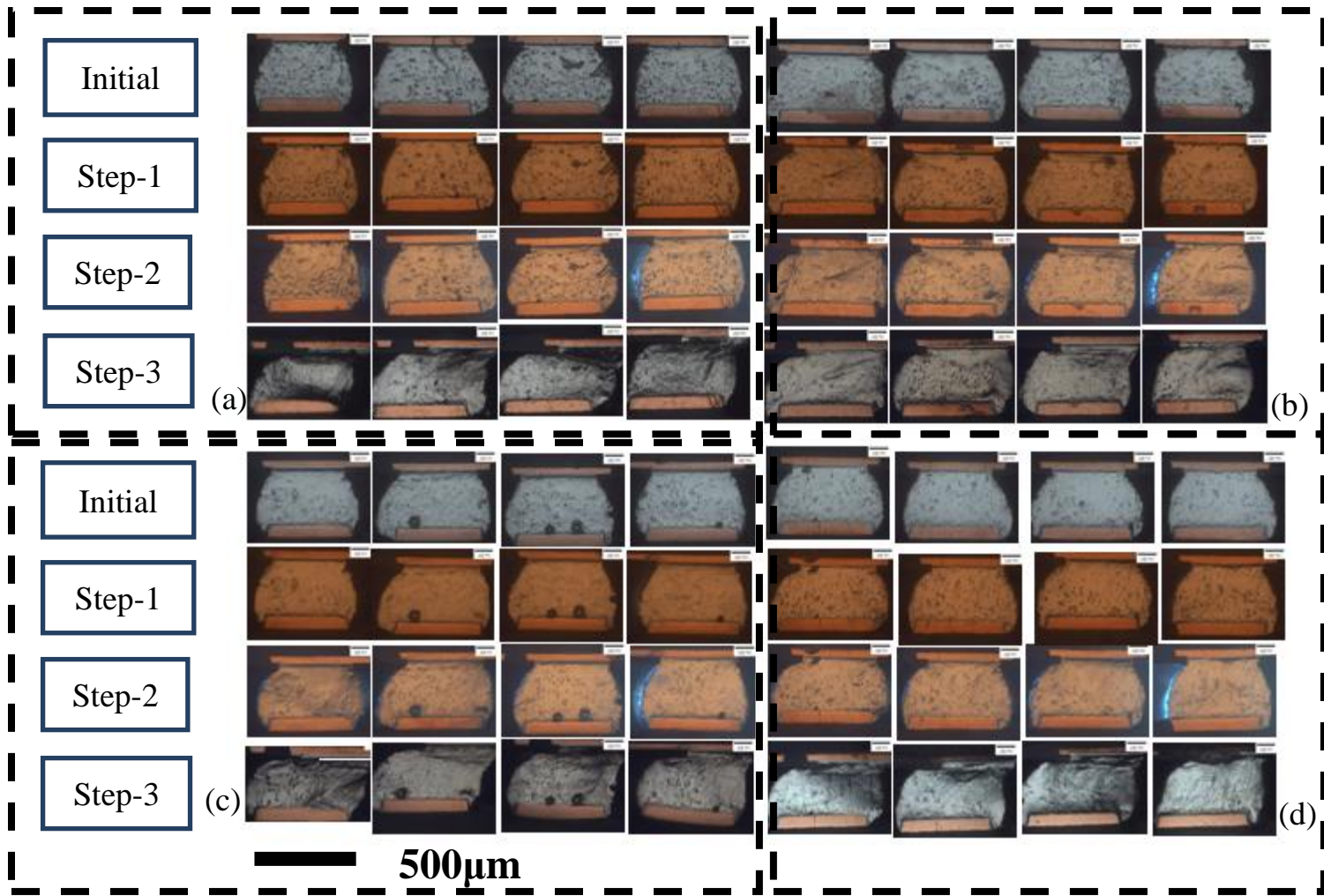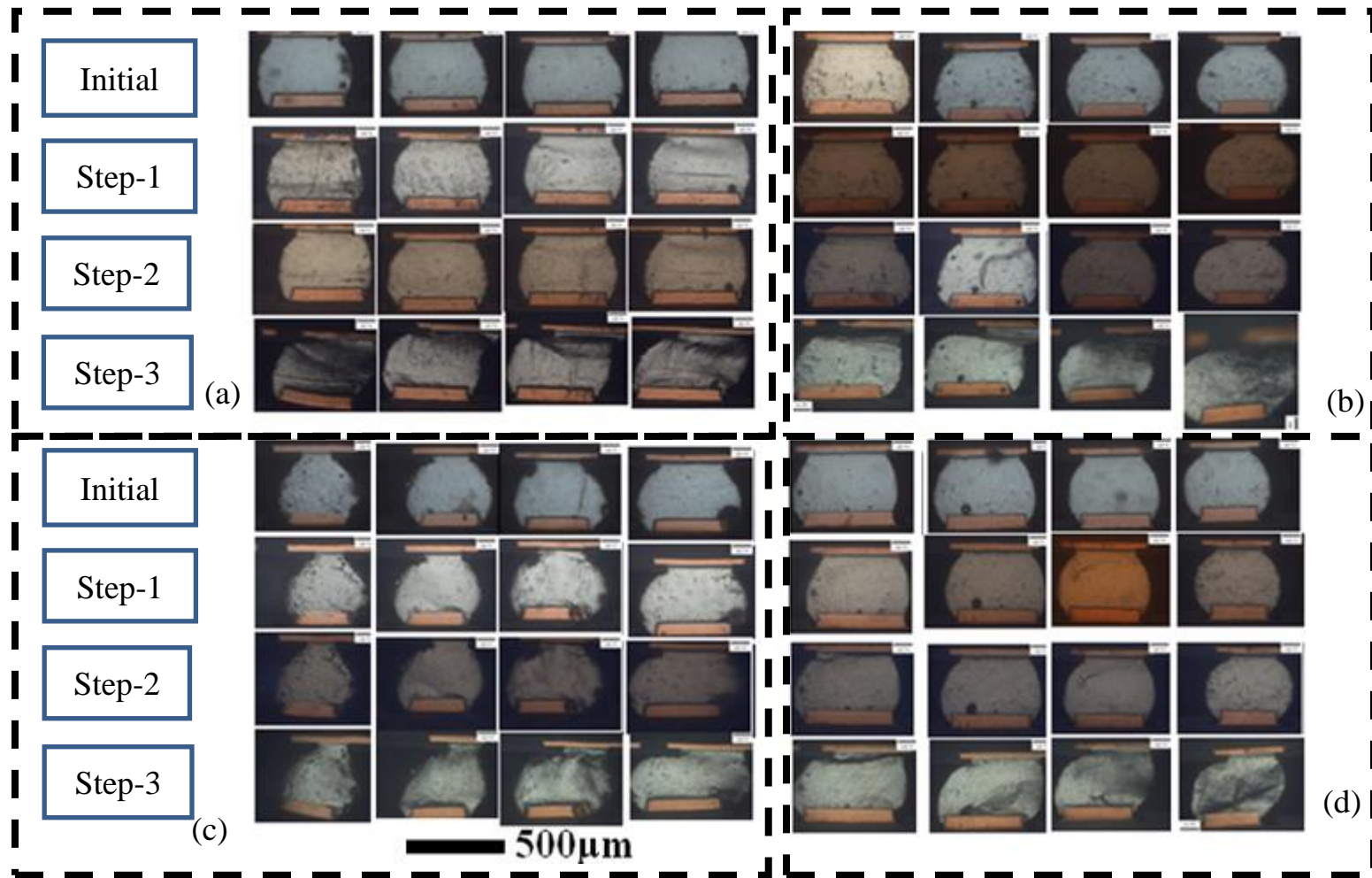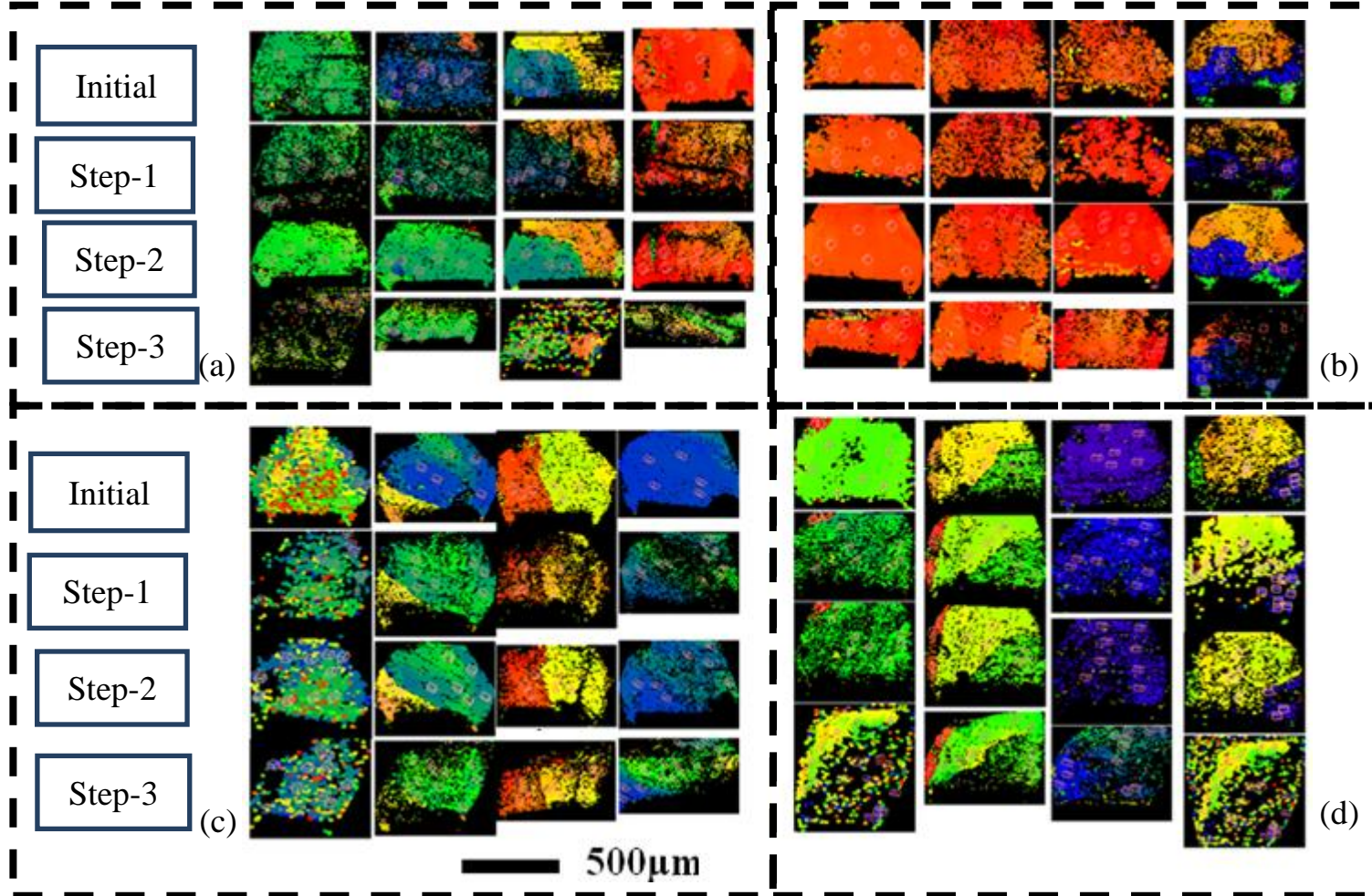
Figure 7.9 C-axis EBSD maps of 4 cross sectioned samples in the unaged condition, showing effects of deformation in three steps at room temperature (a, c) and at 100°C (b, d).
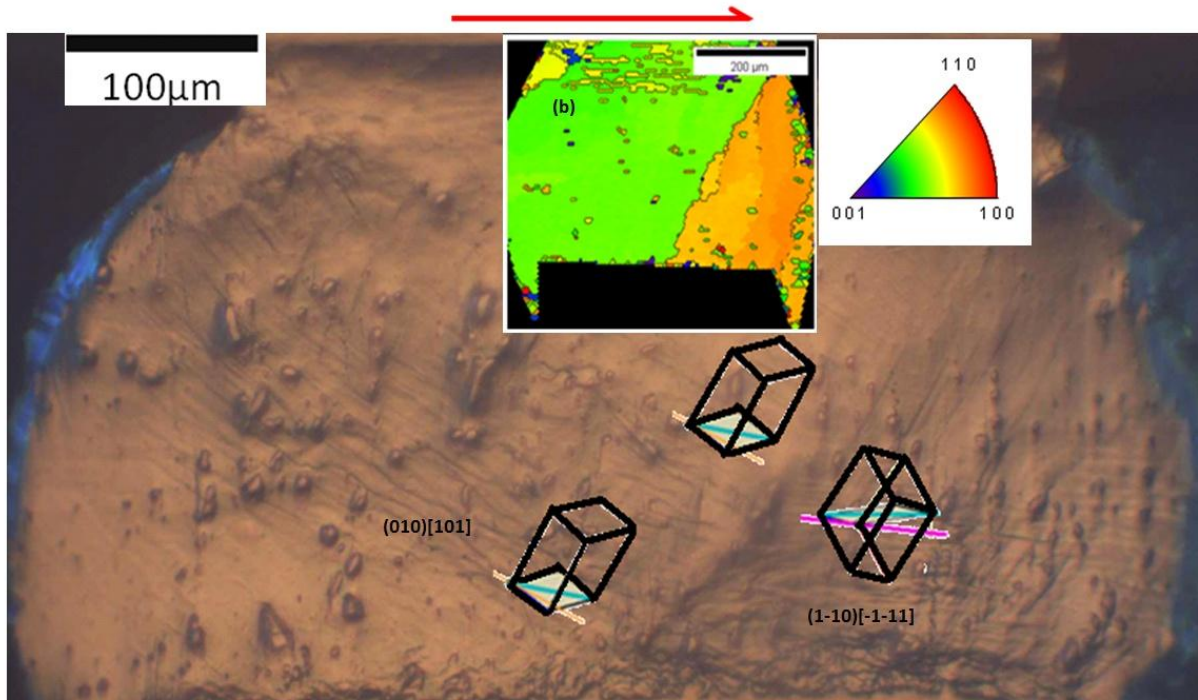
Figure 7.10 Optical micrograph of a solder ball showing slip planes in the right and left areas, (b) c-axis EBSD map corresponding to this solder ball.

Telang (2009). On the right side, (1-10)[-1-11] (4th mode in table 2.1) contributes significantly to the deformation, which shows consistency with observations made by Fujiwara (1987).

Figure 7.11 shows optical microscopy, an SEM Image, and the c-axis orientation map of a shear deformed solder ball. In regions that have "red" orientations where the c-axis is parallel to the interface, the sample undergoes larger deformation. As illustrated in the c-axis map, in the area near the interface there is a grain with red orientation but according to the crystal structure overlaid on this map, the c direction is nearly perpendicular to the shear direction (the shear direction is shown using a red arrow in the top area). Therefore, the contribution of slip along the c-axis is small, and plane trace analysis shows that (-1-21)[101] slip system (10th mode in Table 2.1) was active in this solder ball. This may be due to the fact that increasing the deformation temperature can lead to a decrease in the critical resolved shear stress. This result is consistent with Düzgün et al. (1999) who found out that (121)[10-1] is facile at 90 and 100°C in pure tin single crystals.

Figure 7.12 shows the SEM image and the magnified c-axis orientation map of a shear deformed solder ball (an unaged sample which is deformed at 100 ℃) near the interface area. The c-axis map is illustrated after 0.1mm (b), and 0.42mm (c) deformation. A significant contribution of (1-10)[111] in plastic defo
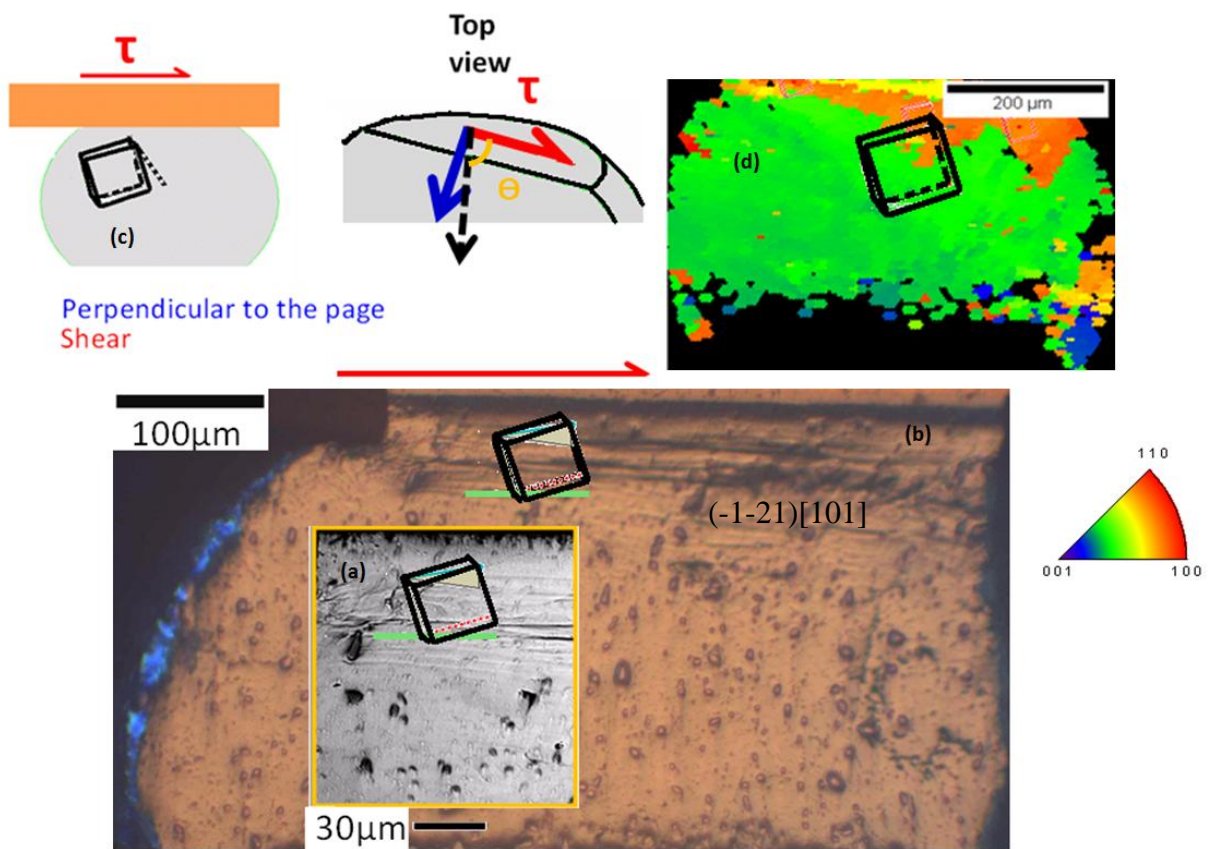
Figure 7.11 (a) inset showing magnified BSE images of an area shown in optical micrograph (b) of sample depicted in (c) to show how the crystal orientation is related to the x-axis slip vector in the "orange" area, (d) c-axis EBSD map.
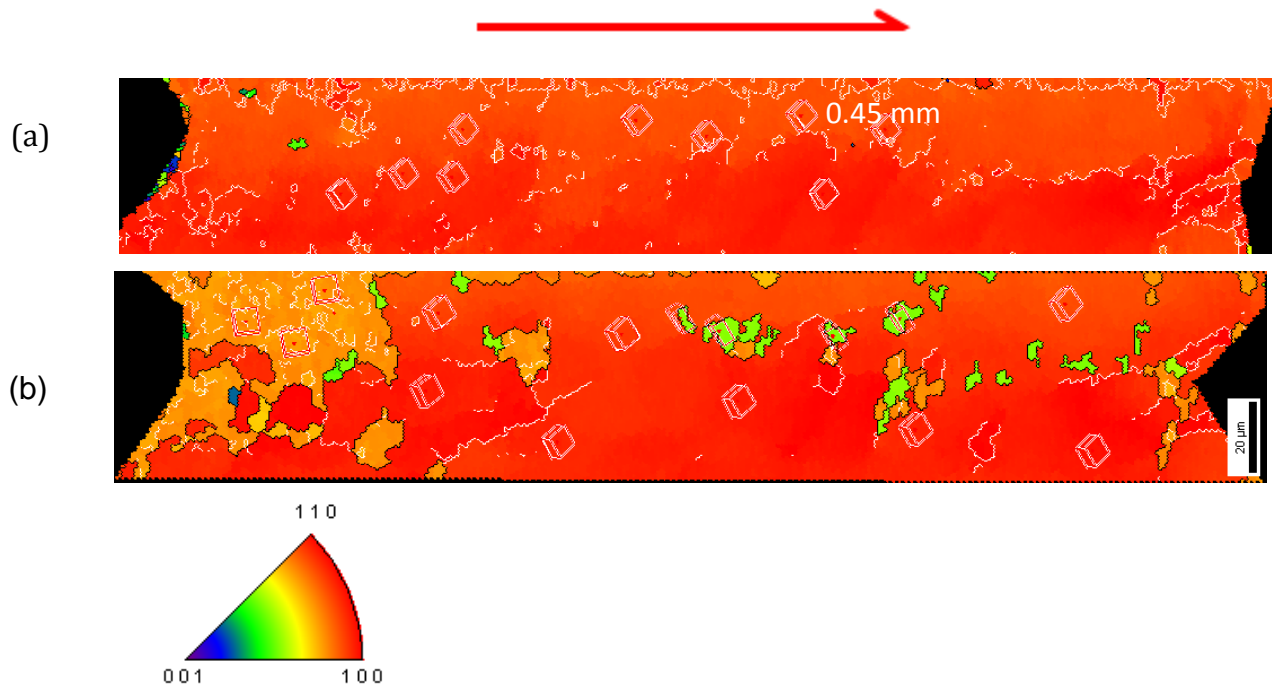
Figure 7.12 (a) c-axis EBSD map for deformed sample after step-1, (b) c-axis EBSD map for deformed sample after step-2, low angle boundaries are illustrated with white lines and high angle grain boundaries are shown with black lines.

rmation along with deformation at 100°C can lead to recrystallization of new grains (orange area in the left part of Figure 7.12(c), and also green and yellow regions in this figure). Observation of this slip system shows consistency with the observation made by Fujiwara (1987).

Figure 7.13 (a-c) shows a comparison between different solder balls in terms of the c-axis orientations (yellow, blue, and red orientations). The figure shows the evolution of the crystal rotation at different steps in the large deformation regions of solder joints (near the interface). It is apparent that in the red orientation c-axis, in which a close packed direction is parallel to the interface, by applying the shear deformation parallel to the interface, a larger amount of deformation and rotation occurs in this area. However, in the blue orientation where the c-axis is perpendicular to the interface, the contribution to the deformation is minimal. This is demonstrated in Figure 7-14 shows the difference in the distribution of misorientation in steps 3 and 1 for three orientations in (a-c). It is evident that a relatively high amount of increase in the misorientation (15-25º) occurs at grain boundaries for the red orientation while for the blue orientation this increase is smaller. For the yellow-green orientation, a decrease in misorientation is observed in the fraction of boundaries misoriented by 15-25º. This indicates that the red orientation has the maximum amount of energy and dislocation content that develops during the large deformation and may represent the early stages of damage evolution. Observation of more damage in the red orientation during the thermo mechanical loading can be related development of more high energy boundaries (Bieler et al (2012)).

Fine-step EBSD c-axis orientation maps and image quality maps for an unaged sample with a blue orientation deformed at 100 ºC is illustrated in Figure 7.15. The c-axis map clearly shows
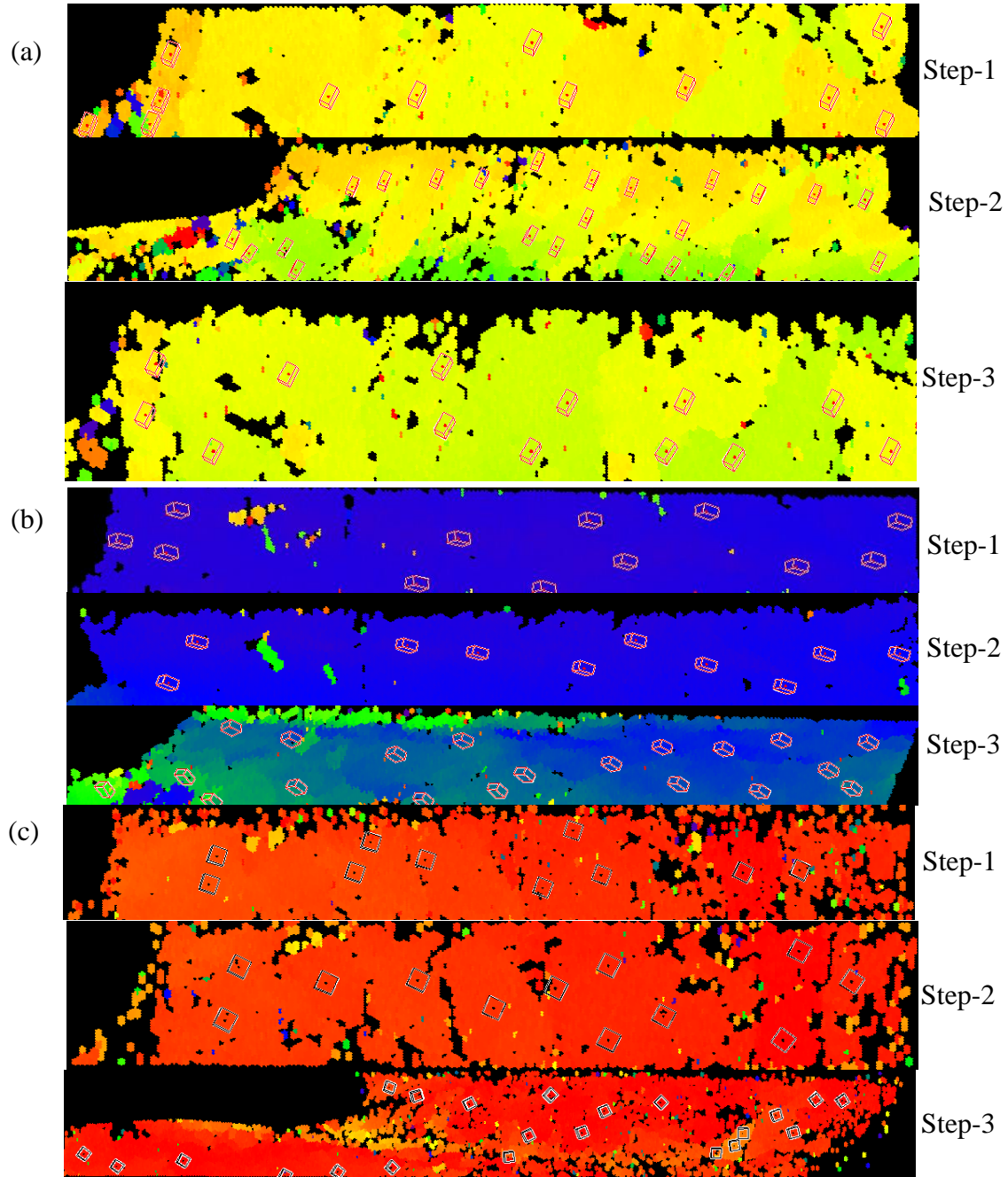
Figure 7.13 Vertical direction c-axis orientation map in large deformation regions of solder joints for three samples with different c-axis orientations and different steps of deformation showing different deformation behavior (a-c). Difference in distribution of misorientation for three orientations in (a-c) showing an increase in the amount of (15-25º) grain boundaries after the large deformation step for blue and red orientations and a decrease in yellow-green orientation (d).
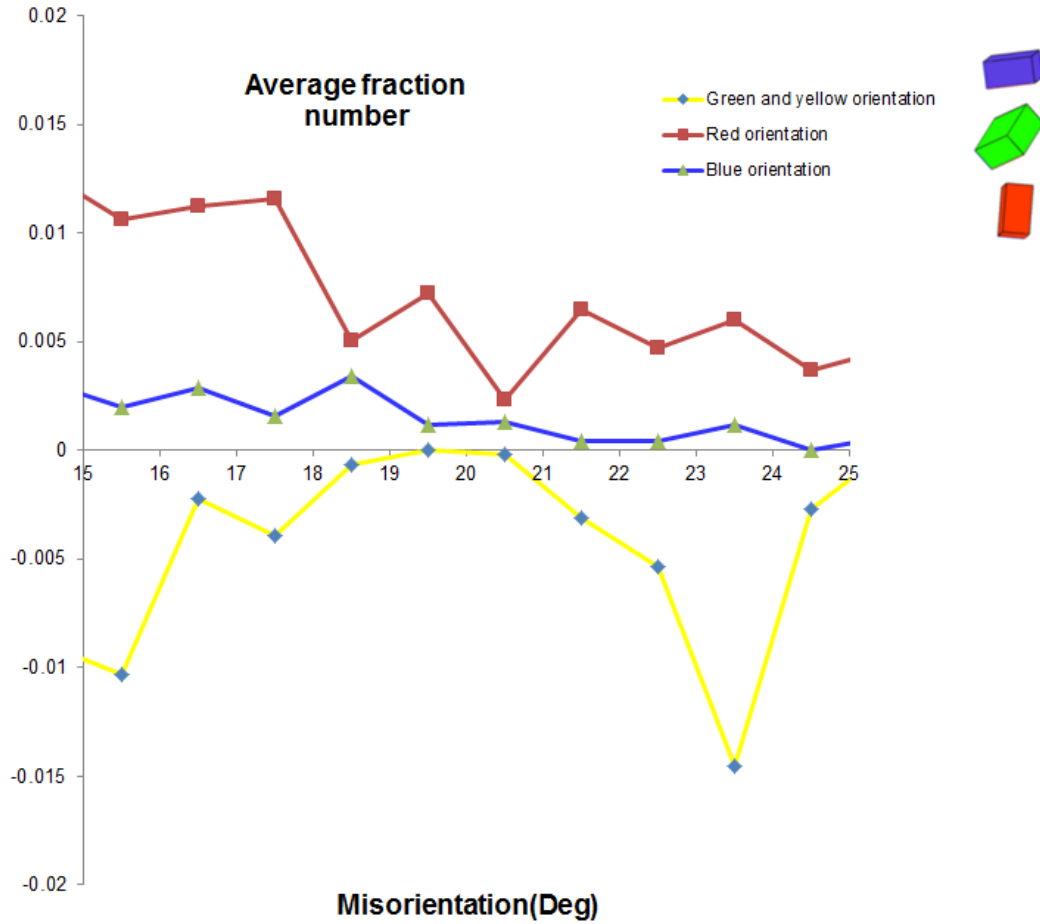
Figure 7.14 Difference in distribution of misorientation for three orientations in (a-c) showing increase in amount of (15-25º) grain boundaries after large deformation for blue and red orientations and decrease in green orientation.

Figure 7.15 Fine-step EBSD c-axis orientation map and image quality maps for step-1(a, b), step-2 (c, d), step-3(e, f) for an unaged sample with blue orientation deformed at 100 ℃, where low angle boundaries are illustrated with white lines and high angle grain boundaries are shown with black lines. Rotation of crystal orientation at different locations (as illustrated with red arrows) due to shear deformation in step-3 (g), evolutions of c-axis pole figures showing the spread in crystal orientations (h).

the change in the crystal orientation due to the large deformation especially at step 3 and at the neck area which shows a shear band (in region that is highlighted with a white arrow). In order to demonstrate inhomogeneous deformation at step-3 the crystal orientation in different locations were compared with the orientation of a location that shows small rotation with respect to step-2. As it is illustrated in 7.15 (g) the rotation generally does not happen around a low index rotation axis in this grain. Development of low angle boundaries [Figure 7.15 (f)] shows the evolution of crystal orientation and increasing the GND's due to the large deformation.

Fine-step EBSD c-axis orientation map and image quality maps for an unaged sample with a red orientation deformed at 100 ℃ is illustrated in Figure 7.16. In this case due to the fact that the the c-axis is parallel to the interface global coordinate system and the crystal coordinate system is coplanar (a plane which is consists of two a-axis in crystal coordinate system is identical to the joint section plane). Therefore, deformation in this orientation occurs with rotation about the c-axis. Similar to the blue orientation the rotation were calculated with respect to a location that its rotation is negligible with respect to the step-2 to be able to represent the crystal rotation that occurs in step-3.

Another important observation regarding these sets of samples is localization of shear deformation, which depending on the crystal orientation can occur in the interior region of grains or along the grain boundaries. Figure 7.17 shows the evolution of microstructure using fine-step EBSD c-axis orientation maps and image quality maps for two steps of shear deformation of an unaged multi-crystal sample deformed at 100 ℃, low angle boundaries are illustrated with white lines and high angle grain boundaries are shown with black lines. As illustrated, a shear band is
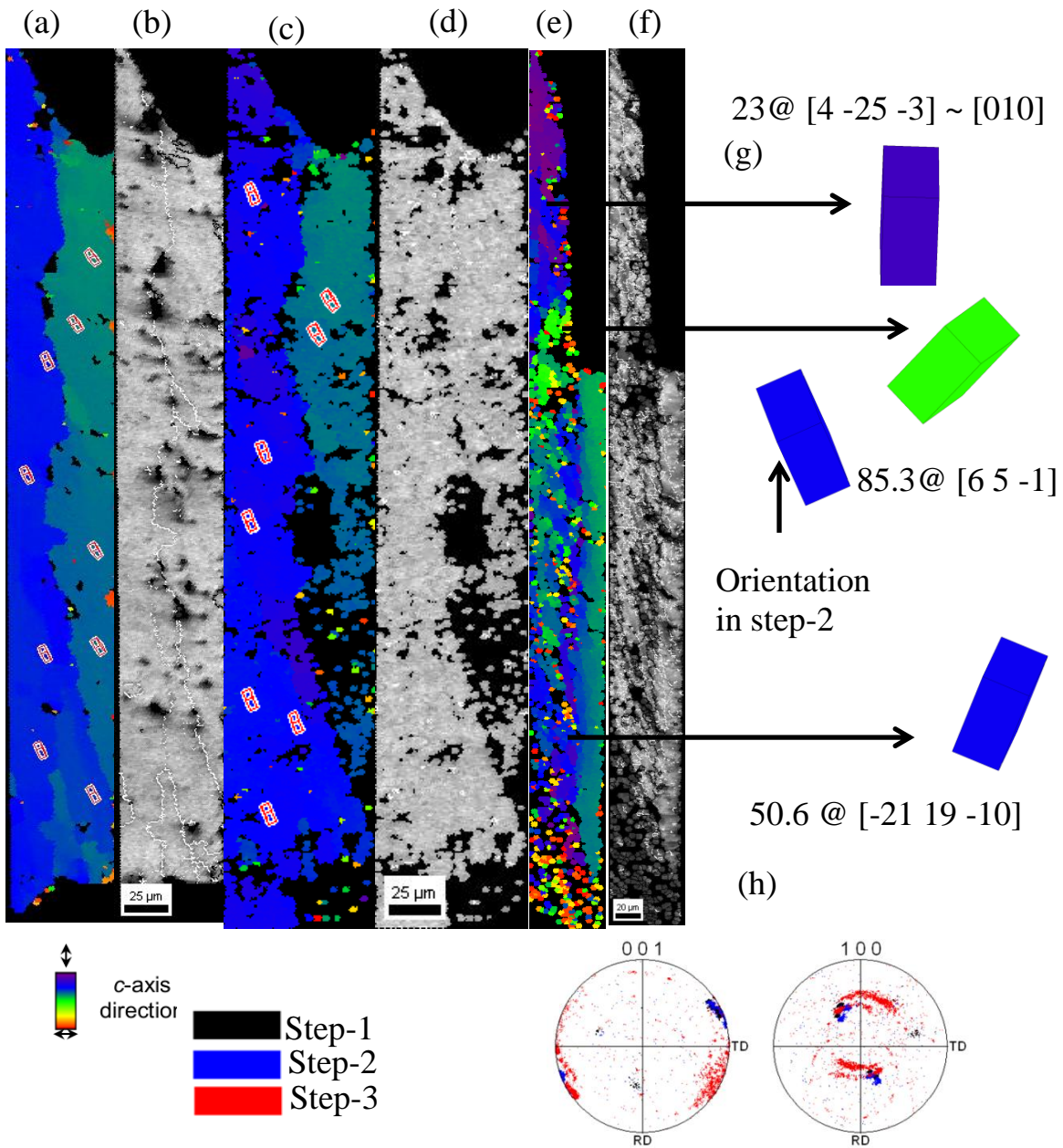
Figure 7.16 Fine-step EBSD c-axis orientation map and image quality maps for step-1(a, b), step-2 (c, d), step-3 (e, f) for an unaged sample with a red orientation deformed at 100 ºC, low angle boundaries are illustrated with white lines and high angle grain boundaries are shown with black lines, crystal rotation at different locations (as illustrated with red arrows) due to shear deformation in step-3 (g), evolutions of c-axis pole figures showing the evolutions of crystal orientations (h).

Figure 7.17 Fine-step EBSD c-axis orientation map and image quality maps for step-1(a, b), step-2 (c, d), step-3(e, f) for a bi-crystal unaged sample deformed at 100 ºC, low angle boundaries are illustrated with white lines and high angle grain boundaries are shown with black lines.

developed in a grain with the blue orientation (7.17(f)) rather than along the grain boundaries. The history of deformation at step-2 (7.17(d)) can assist interpretation of this observation. Development of a shear band at step-3 occurred at regions where sub-grain boundaries were formed at previous steps. Since the deformation happened at 100 ℃ it is expected that plastic deformation leads to the grain boundary movement but in this case the localization of plastic deformation occurs within the grain. This clearly shows the importance of anisotropy associated with the large grain microstructure and crystal structure of Sn which leads to heterogeneous plastic deformation.

In contrast, a completely different phenomenon is observed in Figure 7.18. This figure shows fine-step EBSD c-axis orientation maps and image quality maps for different steps of deformation of an aged sample deformed at room temperature. As illustrated in figure 7.18 (c) deformation at step 3 leads to formation of sub-grain boundaries in one grain but at step-3 the dominant deformation mechanism is movement of grain boundaries. (The grain boundary movement is shown with the red arrow).

Based on the observed activities of these 32 slip systems, OIM, calculated Schmid factor for different slip systems, and observation of plane traces in optical and SEM micrographs, a statistical analysis of the relative activity of slip systems was conducted. Figure 7.19 shows the distribution of the number of observed slip activities on 32 polished half-joints after room temperature shear deformation. These numbers are normalized by the number of slip activities for each family of slip systems. This figure also shows the effect of crystal orientation on the activity of slip systems. For example, for the blue orientation, slip system number 9 is the most
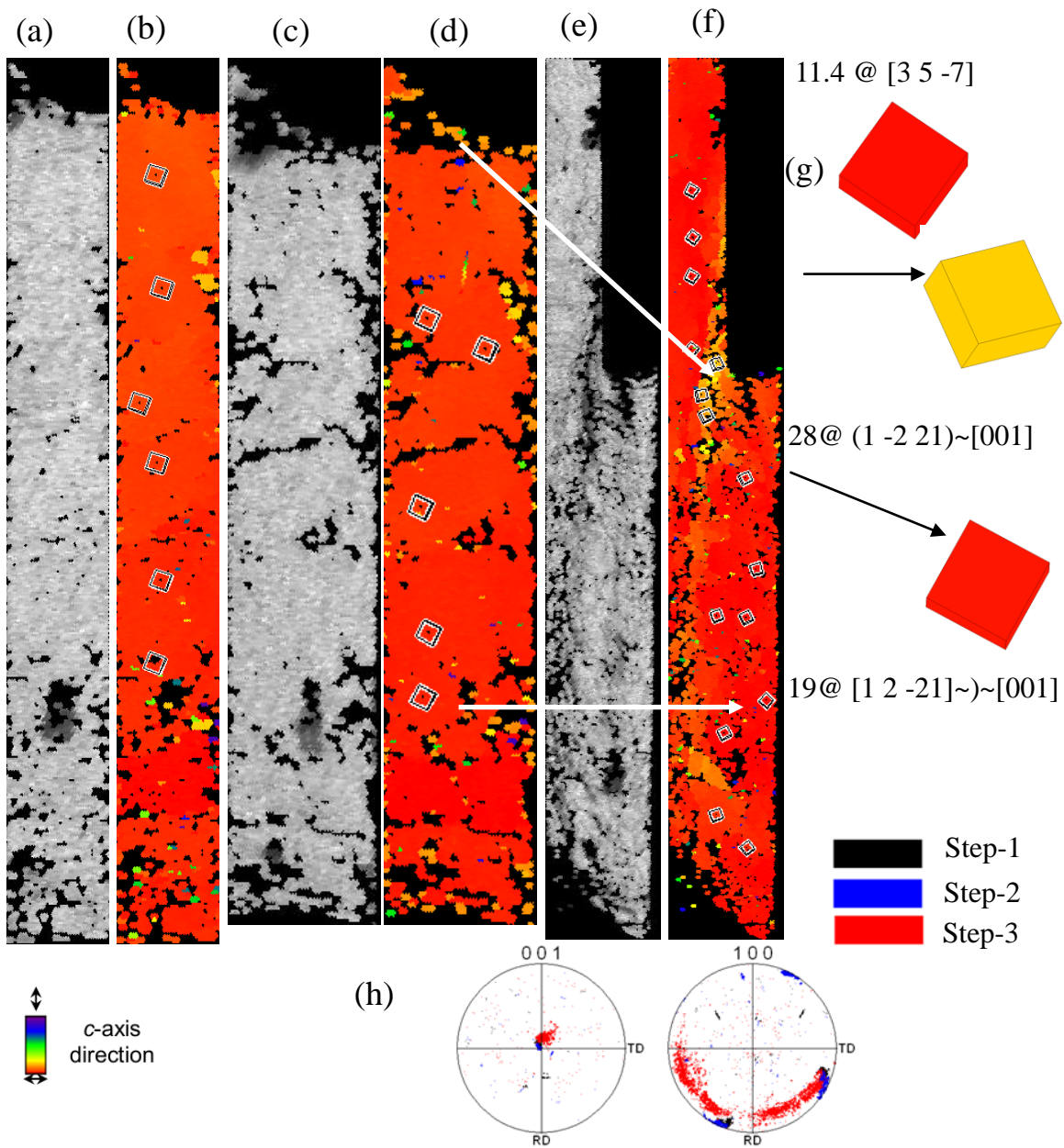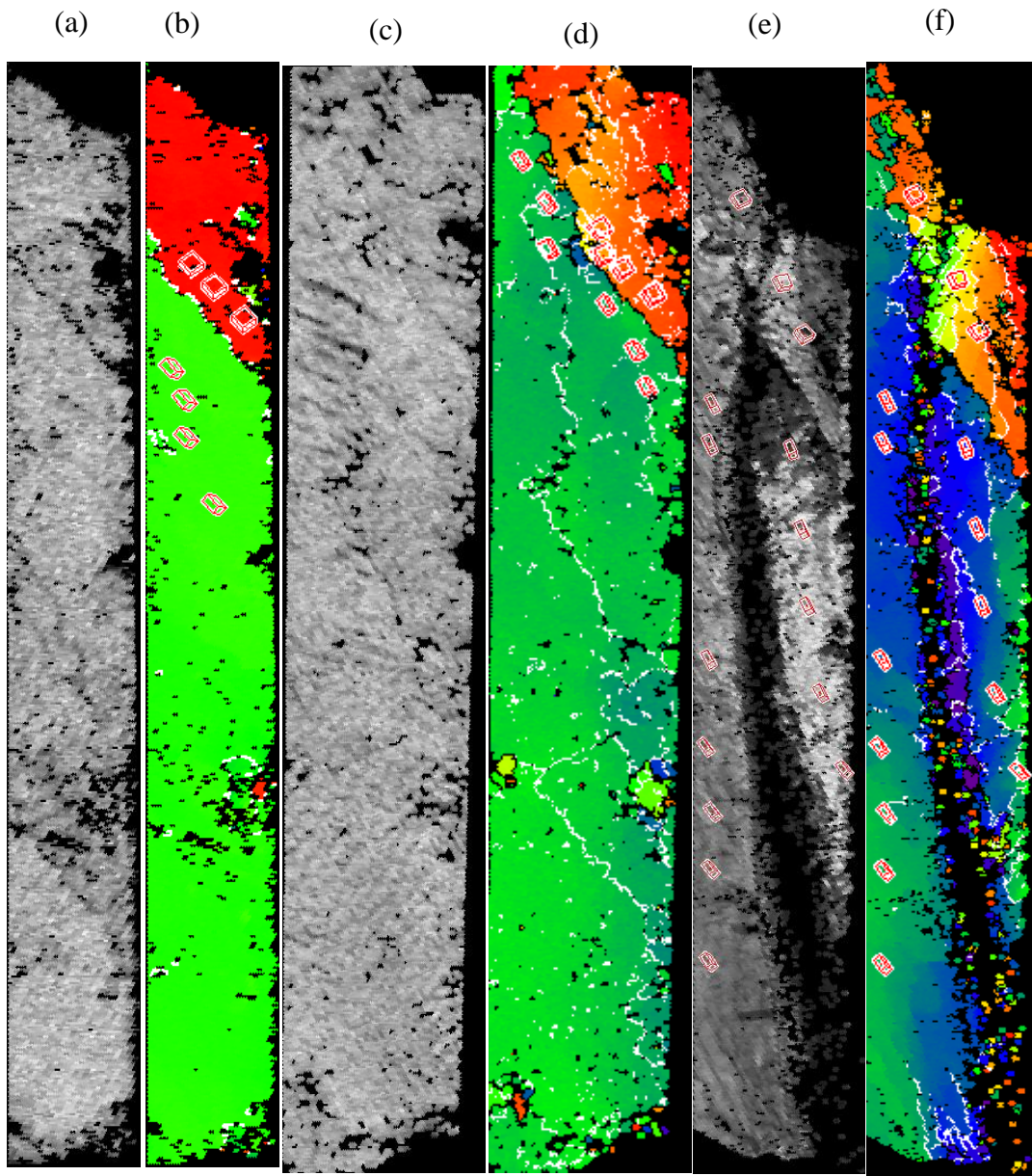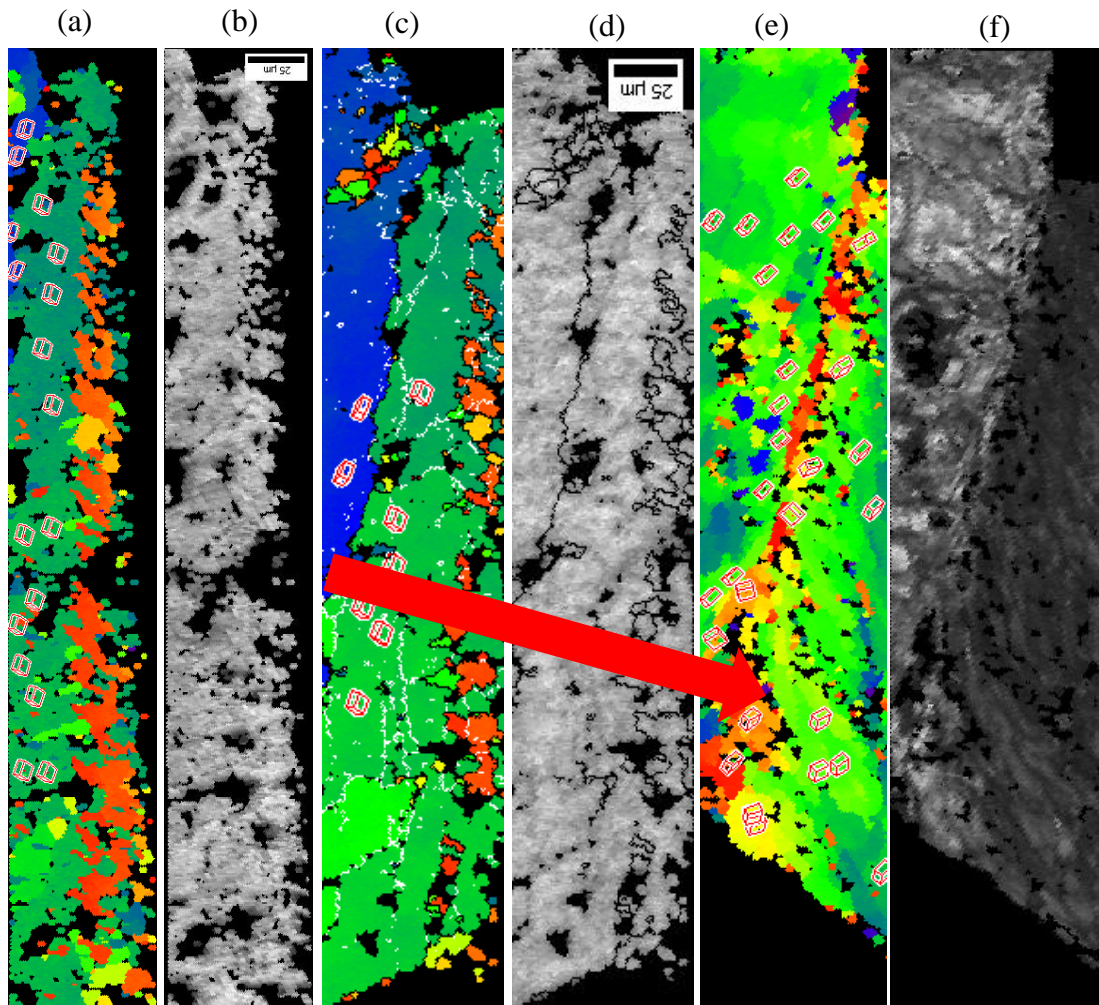
Figure 7.18 Fine-step EBSD c-axis orientation map and image quality maps for step-1(a, b), step-2 (c, d), step-3(e, f) for an aged bi-crystal sample deformed at room tempereture. Low angle boundaries are illustrated with white lines and high angle grain boundaries are shown with black lines.
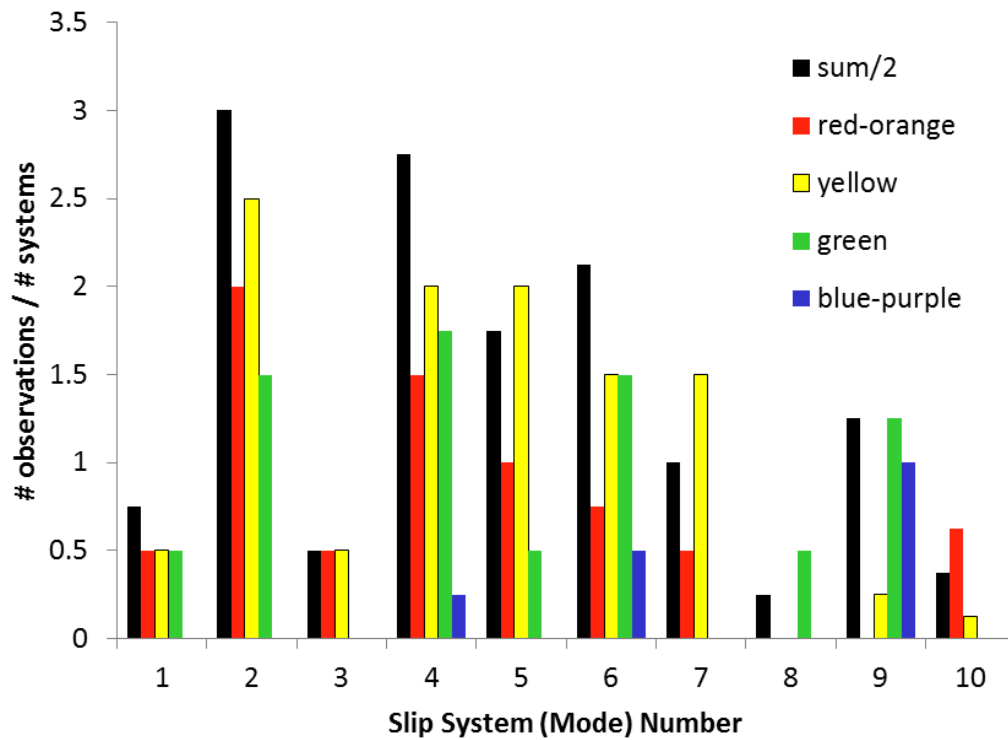
Figure 7-19. Number of observations of slip on 32 polished half-joints after room temperature shear deformation, normalized by the number of slip systems in the family, and separated by the c-axis orientation. Black bars are the sum (divided by 2 to be on a similar scale) of all observed slip activities on joints with c-axis orientations indicated by the colors.

active, while for the red orientation the most active slip system is number 2. The number of observations for slip system number 4 is highest in these set of data.

(note that in Figure 7.19 the number of observation of slip traces is divided by the number of slip systems in each family of slip systems to represent the probability of slip activity and for slip family # 4 which consists of 4 slip systems the number of observation is higher than slip family # 2).

This ranking is different from what Fujiwara found based on the etch-hillocks method for pure tin samples (Table 1). Kinoshita et al. (2012) performed a numerical study using first-principles density functional theory. Based on their orientation-dependence of active slip systems in pure tin samples subjected to uniaxial tension when the c-axis is perpendicular to the loading, the slip system number 9 is the most active slip system, and for the case that c-axis is parallel to the loading direction the slip system number 4 is the most active. These results are similar to what it's observed in this study in terms of the number of observation of each slip systems with respect to c-axis orientation map.

7.4. Summary

Shear deformation was conducted in 3 steps to study the activity of slip systems in SAC305 alloys. Orientation imaging microscopy was performed to identify the orientation evolution of solder balls during shear deformation. Crystal orientation along with SEM and optical micrographs of shear deformed samples, as well as plane trace analysis were conducted to find the relative activity of slip systems. The orientation dependency of the facility in operation of slip systems also was performed. The relative activity of slip systems using this dataset can be

utilized to develop a more reliable crystal plasticity model for SAC 305 alloy which accounts for correlation between critical resolved shear stress and the probability of activating the slip systems based upon the statistical analysis.

CHAPTER 8

EXPERIMENTAL AND NUMERICAL ASSESSMENTS OF TENSILE TEST ON JOINT SCALE SAC 305 SAMPLES

8.1 Introduction

The length scale of the test specimen used to measure the deformation behavior of SAC alloys has significant impact on the mechanical response of these alloys. As it was discussed in chapters 5 to 7, due to the elastic and plastic anisotropy arising from the crystal structure of tin and its large grain microstructure, the sub-mm scale SAC joint exhibits pronounced inhomogeneity in mechanical response as well as damage evolution. Since the length scales of current solder interconnects in the surface mount packages are less than 1000 µm, and this scale is comparable to the characteristic length scale of SAC 305 solders microstructures, the length scales of a reliable test specimen are expected to be comparable with those of functional solder joints to represent the mechanical property and microstructure evolution of lead free solders.

It is important to point out that mechanical properties of sub-mm scale solder balls can be very different from those of bulk materials. At these scales materials experience faster cooling rates than bulk specimens under similar profiles owing to the volume of solder. On the other hand, the larger scale in a bulk specimen results in a gradient in the cooling rate across the entire specimen. Thus, the dendritic and IMC distributions on the edges of the specimen exposed to the ambient are subject to a faster cooling rate compared to those in interior areas. Comparative studies of the microstructures of bulk solder alloys with solder joints of the same alloys show distinctive differences (Sidhu and Chawla (2008) and Sidhu et al. (2008)). In a study by Hegde et al. (2009), the effect that size has on the stress–strain properties of Sn-3.8A g-0.7Cu solder joints was investigated and compared with bulk solder of the same alloy. Their experimental

143

results show a strengthening effect of the constrained joints. The authors suggested that this strengthening is a contribution of the solder joint aspect ratio, state of the stress, and the microstructure.

Due to the complexities arising from the effect of miniaturization in solder balls, prior studies attempted to divide these effects into single parameters in order to treat them individually. Among those parameters, microstructural effects and constraining effects attracted more attention (Khatibi et al (2012)). In order to develop a reliable model that could predict the behavior of SAC alloys at the joint scale, an appropriate framework that accounts for these variables in a single model needs to be developed. Since CPFE models can solve mechanical deformation problems under complicated external and internal constraints imposed by grain morphology (microstructure effects), their use is promising in this context.

Using CPFE is of great importance since at microstructural scales experimental boundary conditions are very difficult to control and monitor. In such cases, experimental results will be very difficult to interpret without the assistance of a model with similar complexity arising from the microstructure and constraining effects.

In this work, a combination of experimental and numerical investigation is utilized to understand the mechanical behavior of joint-scale lead free solders. Although the information in chapter 7 provides valuable insights into the activity of slip systems in SAC 305, these results cannot provide complete information required for developing a reliable model for sub-mm scale solders. Firstly, the load-displacement responses of these shear deformed samples reflect the behavior of 16 solder balls (shear samples have 4×4 configurations) which cannot be directly correlated to the microstructure and crystal orientations of each solder ball. Furthermore,

interaction between different solder balls in the specimen can have a strong impact on the stress evolution at each joint.

The goal of this chapter is to develop a model that not only can satisfy the requirements arising from the kinematic of plastic deformation in terms of both global (shape changes) and crystal (slip activities) coordinate systems, but also accurately predict the magnitude of the stress evolution. Hence, it is important to use the dataset that was developed in chapter 7 to insure that a developed model can satisfy the constraints arising from slip activities.

Previous investigations based on the OIM characterizations and plane trace analysis will define a framework for ranking the slip systems and subsequently defining the critical resolved shear stress based on the probability of activating each slip system. Since the sample preparation for OIM analysis is generally destructive, Synchrotron X-ray microdiffraction experiments were conducted at beamlines 6-ID-D and 34-ID-E at the Advanced Photon Source (APS) to characterize the orientation of each solder joint.

This methodology for developing a new CPFE model, using a combination of experimental and numerical methods, is based on the following steps:

1- Ranking the slip system activities and estimating the probability of activating each slip system based on the statistical data presented in chapter 7.

2- Modeling of the tensile test for a solder ball with a particular orientation which was obtained using X-ray microdiffraction experiments.

3- Finding the value of critical resolved shear stress as a function of the probability of activating each slip system and also fitting the force-displacement data.

Thus, this work provides the basis for developing an integrated, incremental model based on experiment observations, modeling, and comparative analysis. This method is illustrated in

Figure 8.1, and discussed in more detail in section 8.2. The results of non-destructive

characterization, as well as tensile test are described in section 8.3. Finally, section 8.4 describes

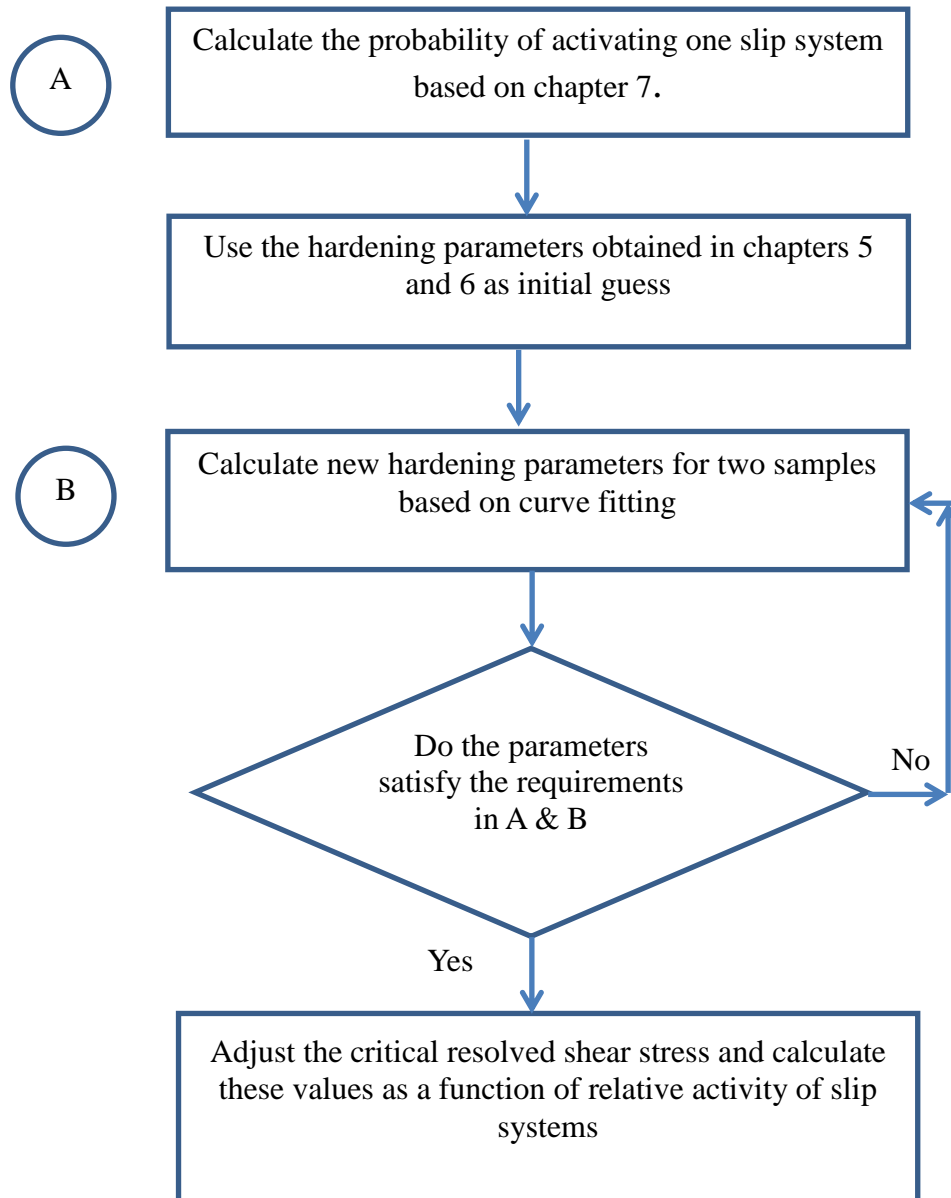the simulation results obtained from our model using steps described above.

Figure 8.1 Flowchart showing the methodology of CPFE modeling of SAC 305 tensile test of SAC 305 joint scale samples using the statistical analysis of slip system activities.

8.2 Statistical analysis on the activity of slip systems

Since the goal is to develop a reliable material model for SAC305 alloys, an appropriate framework is required to represent the relative activity of slip systems. As it was discussed in chapter 2, anisotropy arising from both the complex crystal structure of tin and the large grain microstructures that are observed in SAC 305 alloys have a significant effect on the inhomogeneity in deformation and damage evolution. Anisotropy in the plastic deformation emerges naturally from the activity of slip systems, and in complex crystal structures such as the 32 slip systems in BCT Sn. Understanding the relative activity of slip systems provides a valuable insight into the inhomogeneous deformation in solder alloys. Hence, a model that is developed for SAC 305 has to account for these complexities. Since the critical resolved shear stress is a parameter that represents the relative activity of slip systems in CPFE models, one has to define a framework in which the initial critical resolved shear stress can be correlated with the relative activity of slip systems.

Figure 8.2(a) shows the probability of observation of slip systems based on the assessments that are provided in chapter 7. Based on the methodology that was described above, one can estimate the critical resolved shear stress as following:

$$\tau_{cr}^{\alpha} = \frac{2}{\sqrt{X}} \qquad (8.1)$$

where X is the probability of observation for each slip system. This probability is based on a data set comprising 32 solder balls as illustrated in Figure 8.2 (a). These values are shown in Figure 8.2 (b). In order to be able to propose a more comprehensive model, the chapter 7 dataset was used, which includes both room temperature and 100° C shear deformation. Due to the fact that in tin based solders room temperature is higher than half of its homologous temperature,
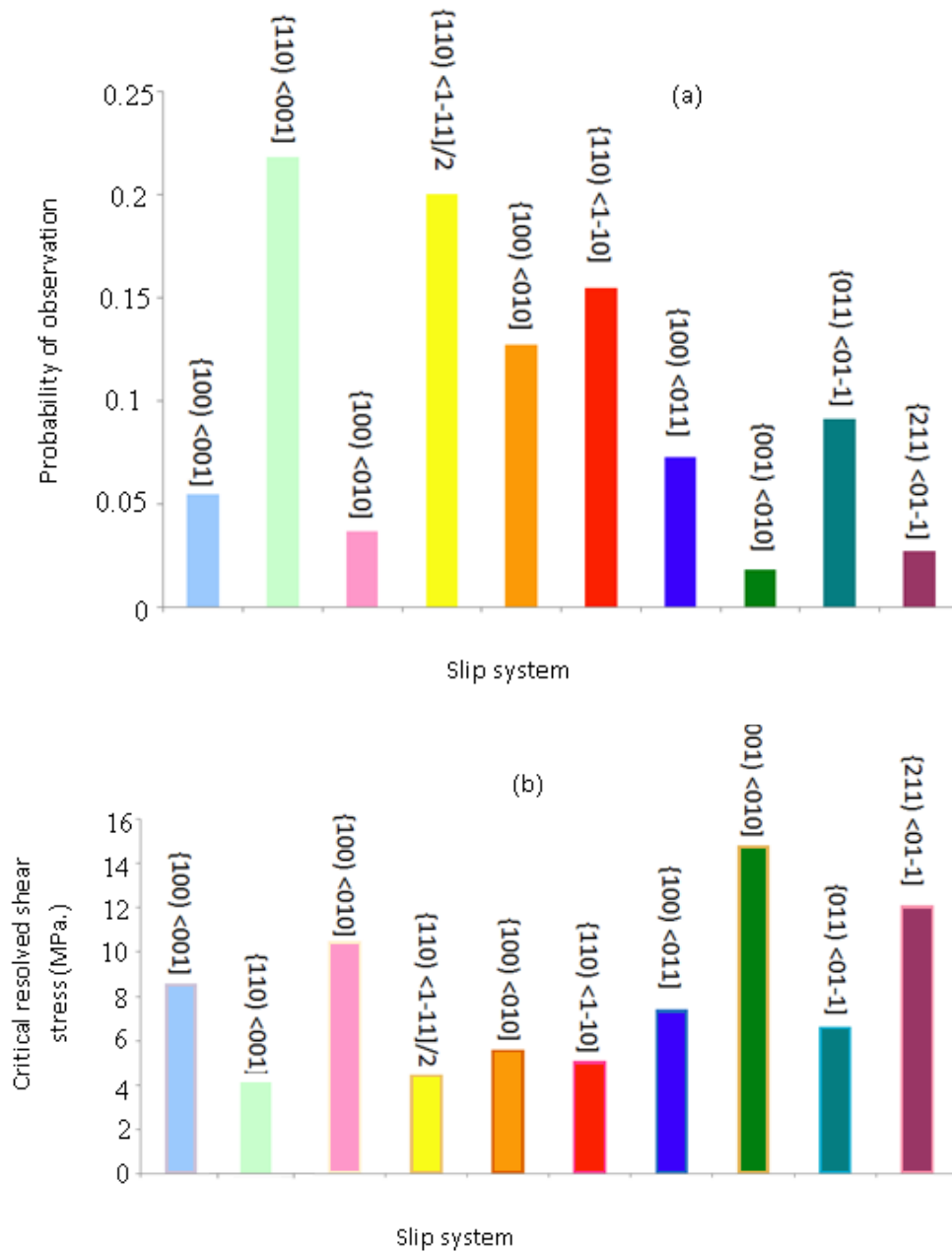
Figure 8.2 (a) Probability of observation of each slip system in data set that was studied in chapter 7. (b) Critical resolved shear stress that is estimated using methodology that is described in Figure 8.1

similar behavior in terms of activity of slip systems and critical resolved shear stress is expected, and as a first generation of the model, the two data sets were merged.

Employing this framework, one can use statistical assessments based on the observation of plane traces using optical microscopy and OIM to estimate the correlation between critical resolved shear stress and the probability of activating slip systems. Based on the flowchart that is illustrated in Figure 8.1, one can estimate the correlation between the critical resolved shear stress and the probability of observation of each slip system based on CPFE modeling of different samples.

Although equation 8.1 is obtained by the curve fitting process, the equations that correlate the dislocation density, shear rate, and the critical resolved shear stress can assist us in understanding the physics associated with that equation. These equations, which were developed by Gilman and Johnson (1957), define a relationship between dislocation density and shear stress.

Figure 8.3 (a) shows this correlation for different materials. The stress dependence of the passage rate of glide dislocations through obstacles in tin is studied by Fujiwara (1987) (Figure 8.3 (b)) .

One can calculate the rate of shear strain based on Orowan's equation as following:

$$\dot{\gamma} = \rho^\alpha b^\alpha v^\alpha \tag{8.2}$$

Where ρ^α, b^α, v^α are dislocation density, burger's vector, and dislocation velocity respectively at each slip system enumerated by the α superscript.
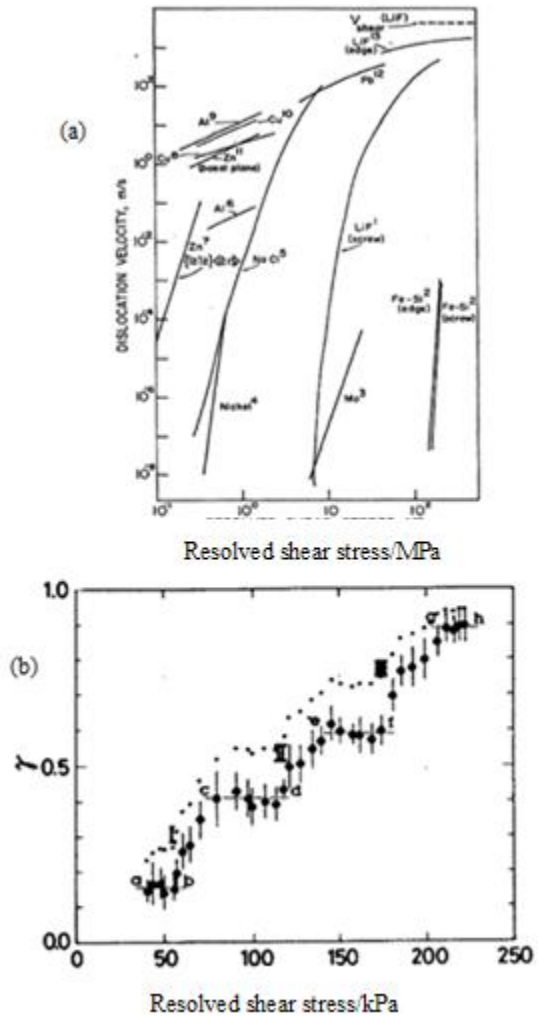
Figure 8.3 (a) Dislocation velocity versus resolved shear stress for different single crystals (Meyers (1984)), (b) Stress dependence of the passage rate of glide dislocations through obstacles in tin (Fujiwara (1987).

Johnston and Gilman (1957 and 1959), Hahn (1962), and Greenman (1967) found the following relationship between the dislocation velocity and the resolved shear stress at a constant temperature:

$$v^\alpha = A \left(\frac{\tau^\alpha}{\tau_{cr}^\alpha} \right)^m \qquad (8.3)$$

Using equations (8-2) and (8-3) one can define the shear strain rate and initial critical resolved shear stress as following

$$\dot\gamma^\alpha = \rho^\alpha b^\alpha v^\alpha = A\rho^\alpha b^\alpha \left(\frac{\tau^\alpha}{\tau_{cr}^\alpha} \right)^m \Rightarrow \tau_{cr}^\alpha = \tau^\alpha \left(\frac{A\rho^\alpha b^\alpha}{\dot\gamma^\alpha} \right)^{\frac{1}{m}} \qquad (8.4)$$

Or:

$$\tau_{cr}^\alpha = \tau^\alpha K_1 \left(\frac{1}{\dot\gamma^\alpha} \right)^{\frac{1}{m}} \qquad (8.5)$$

Where $K_1 = (A\rho^\alpha b^\alpha)^{\frac{1}{m}}$

On the other hand, using Taylor's equation one can calculate the resolved shear stress as follows:

$$\tau^\alpha = \alpha G b^\alpha \sqrt{\sum_{i=1}^{n} \rho^\alpha} = \alpha G b^\alpha \sqrt{\sum_{i=1}^{n} \frac{\dot\gamma^\alpha}{v^\alpha b^\alpha}} = K_2 \sqrt{\sum_{i=1}^{n} \dot\gamma^\alpha} \qquad (8.6)$$

Where $\alpha \; and \; G$ are materials constant and

$$K_2 = \alpha G b^\alpha \mu^\alpha$$

In this equation it is assumed that:

$$\sqrt{\frac{1}{v^\alpha b^\alpha}} = \mu^\alpha = fitting \; parameter$$

One can assume that m=2 in equation 8.5 and write this equation as following:

$$\tau_{cr}^{\alpha} = K_1 K_2 \sqrt{(\sum_{i=1}^{n} \dot{\gamma}) \frac{1}{\dot{\gamma}^{\alpha}}} = \frac{K_1 K_2}{\sqrt{\frac{\dot{\gamma}^{\alpha}}{\sum_{i=1}^{32} \dot{\gamma}^{\alpha}}}} = \frac{K_1 K_2}{\sqrt{X}} \qquad (8.7)$$

where X is the probability of observation for each slip system as it was defined in equation 8.1.

By conducting curve fitting on tensile test data one can find that $K_1 K_2 = 2.0$, similar to what is introduced in equation 8.1.
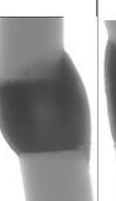
8.3 Experimental results
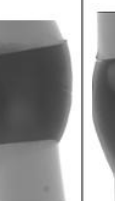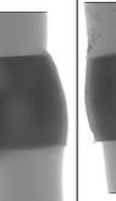
In this study, in order to develop and evaluate the CPFE model, 27 single joints were prepared using a miniature jig. The tensile sample fabrication procedure is detailed in chapter 3. It should be noted that fracture in ductile materials, such as Sn solder alloys, damage nucleation and evolution is controlled by slip or void growth. To investigate the contributions of each parameter, it is necessary to examine the quality of the samples. Radiographic investigations were conducted to examine the quality of single joint samples. Figures 8.4 and Figure 8.5 show the radiographic images of the joints. Since two different characterization methods were employed to extract the crystal orientation in these samples, these sample sets are labeled as A and B.

These examinations assisted in selecting defect free samples with minimal voids and porosity to conduct the CPFE analysis of tensile testing using a realistic geometry. On the other hand, the presence of voids in the samples is a mechanism that has a significant impact on damage evolution. The radiographic images for the tensile deformed samples are shown in Figures 8.4b, and 8.5b. These micrographs clearly show the impact of voids on the nucleation and evolution of crack in the tensile samples.

It is apparent (upper left corner and lower right corners of Figure 8.4-A1), that growth of two neighboring voids and coalescence of these voids can lead to the nucleation of cracks. In addition, a big void at the center of sample A3(a) and development of crack in this area is strong evidence that shows the influence of voids in nucleation and evolution of cracks.

One parameter that is required for conducting the CPFE analysis is grain orientation. Different methods have been utilized to capture the grain orientations of lead free solder balls (Bieler at al. (2012)). In chapter 7, OIM was employed to find the grain orientation for sectioned

(a)

(b)
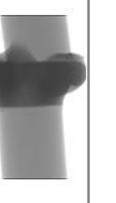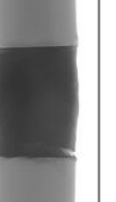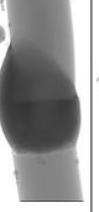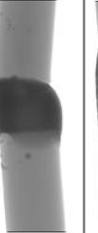
Figure 8.4 Radiographic micrographs of tensile samples which are characterized using beamline 34 before (a) and after (b) deformation. Voids are shown as bright spots.

Figure 8.5 Radiographic micrographs of tensile samples which are characterized using beamline 6 before (a) and after (b) deformation. Voids are shown using bright spots.

shear samples. One of the disadvantages of EBSD is that in order to obtain the back scatter images, generally, it is required to have a flat surface. In this study, the possibility of conducting the OIM investigation without polishing too much of the sample was examined. Due to the roughness of the samples, this approach was unsuccessful. Hence an X-ray diffraction method was employed to extract the grain orientations in joint scale samples.

Synchrotron X-ray microdiffraction experiments were conducted on beamline 34-ID-E at the Advanced Photon Source (APS) at Argonne National Laboratory to characterize the grain orientations for the samples that are shown in Figure 8.. These orientations are obtained up to a 200 micron depth underneath the surface. The characterization of orientation is shown in Figures 8.6 for the front and back of the samples, and the orientations of the samples are tabulated in Table 8.1.

Characterization of crystal orientations for joint scale tensile sample set B are shown in Figure 8.6, using a high energy monochromatic X-ray beam, accomplished at beamline 6-ID-D at the Advanced Photon Source (APS) at the Argonne National Laboratory. These methods are described in chapter 3. Table 8.1 shows the three Euler angle values for samples which were characterized at beamline 6..

The results of tensile testing for sample set A that were characterized at beamline 34-ID-E are shown in Figure 8.7. The crystal orientation is represented by oriented crystal structure with colors identical to each curve. In these sets of samples, due to limitations in preparation of tensile samples, there is inconsistency in geometries of samples. Therefore, correlating the mechanical response (force-displacement curves) which is the function of both sample geometry and crystal orientation with each of these parameters is difficult. However, a few samples (such

Table-8.1 Euler angles value for samples which are characterized using beamline 34 (labeled by "A") and beamline 6 labeled with "B".

Sample	φ_1	Φ	φ_2
A1	178	133	16
A3	352	51	6.8
A4	183	66	39
A5	205	35.6	37
A6	246	40	290
A7	2.69	132	144
A10	314	108	22
A11	336	36	246
A12	63	95	267
B1	9.4	74	137
B2	335	64	39
B3	300	117	201
B9	101	63	304
B12	46	76	134
B14	89	119	294

#	A1	A3	A4	A5	A6	A7	A8
Front							
Back							

#	A10	A11	A12	A13	A14	A15
Front						
Back						

Figure 8.6 Orientation image for samples A in Figure 8.4 which are characterized using beamline 34 before deformation.
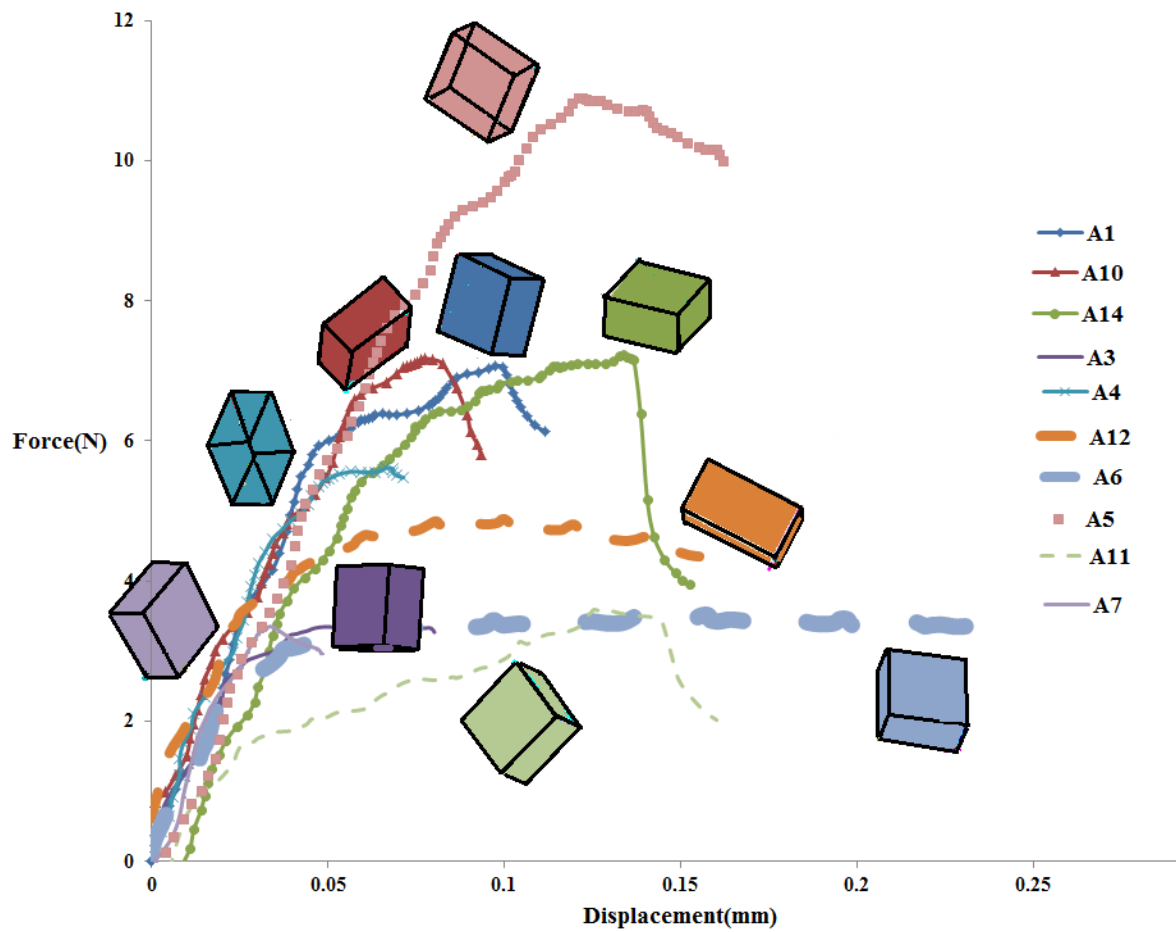
Figure 8.7 Force –displacement curves for tensile sample set A, which were partially characterized using beamline 34. The crystal orientation is overlaid close to each mechanical response to show the correlation between orientations and mechanical responses.

as A12 and A6) had more uniform shapes compared to other samples, and their mechanical behavior is without instability, so that the deformation could be effectively correlated with the crystal orientation. This correlation will be described later.

The results of tensile testing for samples characterized at beamline 6 are shown in Figure 8.8. The crystal orientation is shown with the color similar to each curve. A large amount of plastic deformation (Figure 8.5) and relatively small hardening is observed in sample B3 in which the c-axis has a small deviation from the tensile direction.
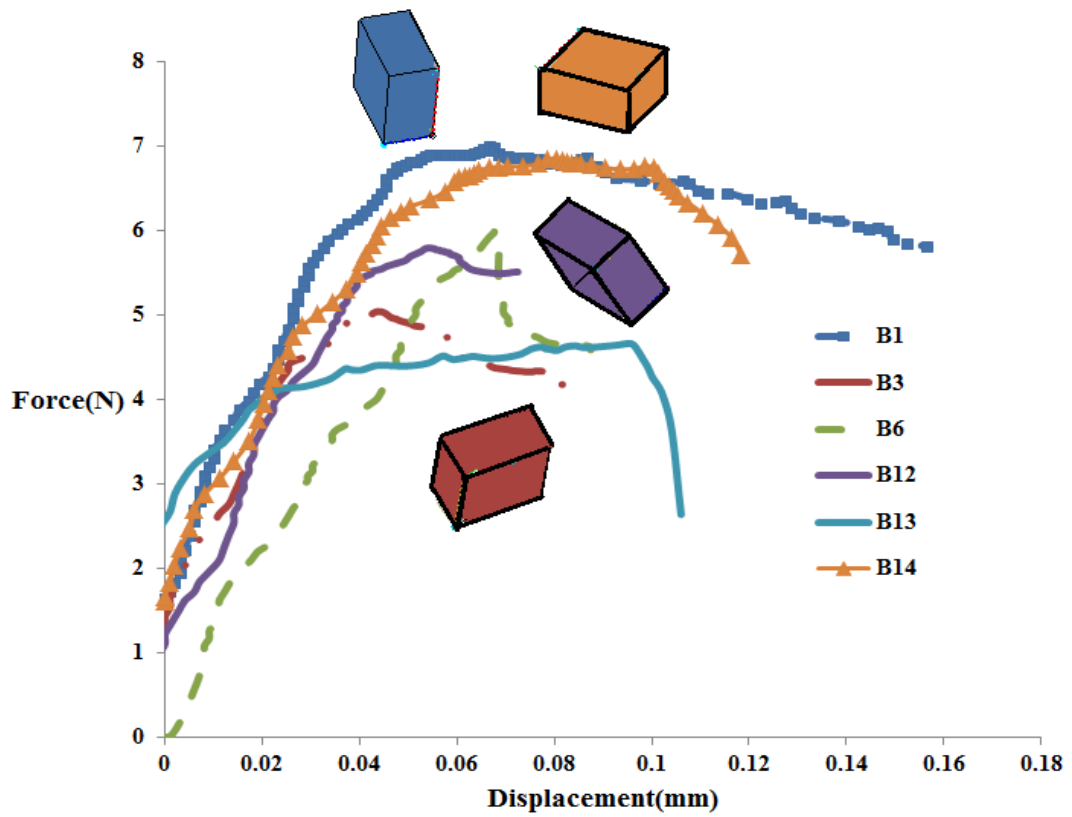
Figure 8.8 Force–displacement curves for different tensile samples which are partially characterized using beamline 6. The crystal structure is overlaid close to each mechanical response show the correlation between orientations and mechanical responses.

8.4 Simulation results:

The crystal plasticity model developed by Zamiri and Pourboghrat (2010) for FCC metals was used to study tin. Firstly, the existing crystal plasticity model was modified in order to account for the more complicated crystal structure of tin. Tin has a body centered tetragonal (BCT) crystal structure with 32 slip systems modeled. Since not much is known from the literature about the relative ease of slip activity of tin slip systems, slip resistance or hardening characteristics, in chapters 5 and 6 a modified crystal plasticity model was developed. This model was used to simulate the deformation of solder balls under shear loading, in order to identify the likely active slip systems and hardening properties that allow comparison with experiments. Experimental verification in those studies were limited to kinematics of plastic deformation, and the hardening parameters were obtained using experiments reported by Darveaux et al. (2005). In this chapter, in light of a better understanding about the activity of slip systems which were obtained in chapter 7, and experimental tensile tests that were described in this chapter, a more sophisticated model was developed which is based on the assumption that the critical resolved shear stress is different in different slip systems.

Due to its formulation, the crystal plasticity model calculates shear rate for each slip system, allowing the user to identify the most active slip systems for a given increment of plastic deformation. The incremental hardening of slip systems is also a function of the magnitude of shear rates, and hardening parameters. Once these parameters were fitted to an experimental dataset, they were no longer modified when the code was used to simulate the deformation of tin solder balls under different loading conditions.

The finite element analysis was performed using the commercial finite element code ABAQUS. The crystal plasticity material model was implemented using a user material

subroutine in FORTRAN (VUMAT). ABAQUS CAE 6.11-1 was used to make the model for the solder joint scale samples, create the finite element mesh, assign boundary conditions, and to build input parameters for the analysis. Element types and number of elements used in CPFE are shown in **Table 8.2.** The elements are 8-node linear bricks with reduced integration and hourglass control. Hourglassing can be a problem with first-order, reduced-integration elements (CPS4R, CAX4R, C3D8R, etc.) in stress/displacement analyses. Since the elements have only one integration point, it is possible for them to distort in such a way that strains calculated at the integration points are all zero, which in turn leads to uncontrolled distortion of the mesh. First-order, reduced-integration elements in ABAQUS include hourglass control, but they should be used with reasonably fine meshes. Hourglassing can also be minimized by distributing point loads and boundary conditions over a number of adjacent nodes. The elastic constants for tin are known and tabulated in **Tables 8.3.** The parameters used for hardening in **Table 8.4** and **Table 8.5** were chosen using the algorithm that is shown in Figure 8.1 so that these parameters not only generated trends that are commonly observed in multi-crystals, but also can satisfy the hardening requirements. Estimation of materials parameters was conducted using the trial and error.

Table 8.2 Element Types and number of elements used in CPFE.

Material	No. of elements	Type of element
Tin	18304	C3D8R
Cu wire	1512	C3D8R

Table 8.3 Elastic Constants (GPa.) of Tin used in numerical analysis.

Parameter	C11	C22	C33	C44	C55	C66	C12	C13	C23
	72.3	72.3	88.4	22.0	22.0	24.0	59.4	35.8	35.8

Table 8.4 Hardening parameters of tin for different slip systems used in numerical analysis.

Parameter	h_0	a	q	m	ρ
	75 (for all sets)	2.0 (for all sets)	1.4	1	60

Table 8.5 Critical resolved shear stress calculated based on statistical analysis

Slip system	# in family	τ_0	τ_s
{100) <001]	2	8.5	11
{110) <001]	2	4.3	9
{100) <010]	2	10.4	11
{110) <1-11]/2	4	4.5	9
{110) <1-10]	2	5.6	10
{100) <011]	4	5.1	10
{001) <010]	2	7.4	10
{001) <110)	2	15	11
{011) <01-1]	4	6.6	9
{211) <01-1]	8	12	11

8.5 Case study- CPFE modeling of sample A12 (in Figure 8.4)

In order to validate the CPFE model and the framework which is developed based upon the microstructural investigations, modeling of one of the solder samples is described in this section. Due to the fact that Sample 12 has a cylindrical geometry and no voids were observed in this sample from radiographic investigations, this sample deformed uniformly, making , this sample is an appropriate candidate for this study.

A simplified geometry and dimensions of sample A12 is shown in Figure 8.9. The coordinate system used to define the Euler angles is illustrated in this Figure. The Euler angles and the geometry are defined in the OIM coordinate system. Copper is modeled as an elastic material with Young's modulus, E =115 GPa and Poisson's ratio of v =0.35. Element types and number of elements used for Cu and Sn are tabulated in **Table 8.2.**
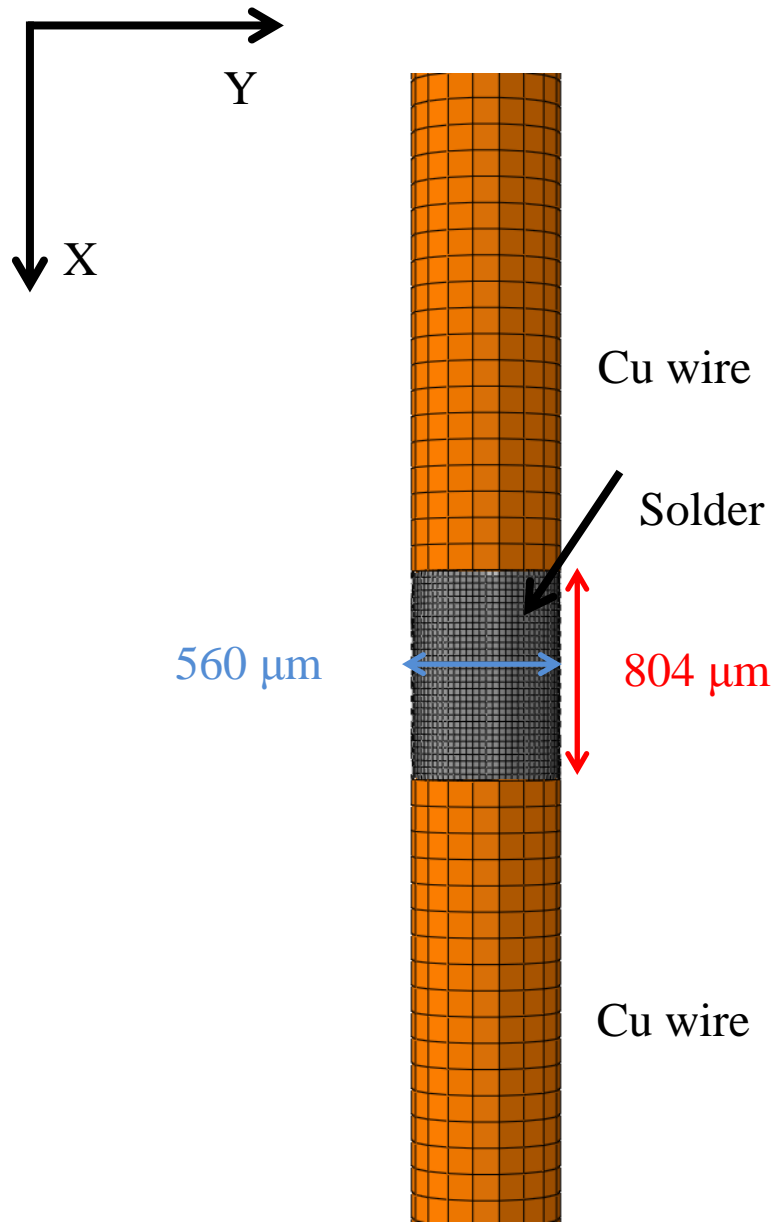
Figure 8.9 Simplified geometry and dimensions of   of sample A 12 in Figure
8-5 , with coordinate system used for Euler angles.

Contours of the von-Mises stress obtained from the CPFE modeling are shown in Figure 8.10. It is apparent in this figure that the localization of the stress and the rotation of the sample take place in the diagonal direction. The predicted maximum value of stress (~ 33 MPa) is in the same range as that reported in the literature for the effective stress in the large plastic deformation of tin alloys.

The relative activity of slip systems are shown in Figure 8.11. As illustrated, the slip system (010)[001] (mode #2 in Table 2.1) has the highest value of activity followed by slip system (011)[01-1] (mode #9 in Table 2.1).

Figure 8.12 shows the force-displacement response of this sample as it undergoes tensile deformation. Curve fitting was conducted to obtain the hardening parameters, and to assess the relative activity of slip systems, as reported in **Tables 8.4** and **8.5.** Also, in order to examine the reliability of the current hardening parameters, sample 6 was also examined. As shown in Figure 8.12, the mechanical response of this sample is quite close to the experimental force-displacement curve corresponding to this sample. This observation shows that the stress evolution using this framework can predict the mechanical response of different samples with a different initial orientation.

Figure 8.13(a) shows a magnified SEM picture for Sample A12 in Figure 8.4. It is evident that plane traces are observed in different locations. In addition, a sample rotation is clearly illustrated in this figure. Using the orientation corresponding to this sample, slip plane estimations associated with this crystal orientation, and slip traces observed in this sample, it is shown that (010)[001] (mode #2 in **Table 2.1**) is the most active slip system. This slip system is shown using a magenta line on this plot.

169

Figure 8.13(b) shows a magnified picture of the slip system activity associated with this slip system. It should be pointed out that there is a mix of crystal rotations and rigid body rotations, which can impact the activity of slip systems. As it is shown, the model can predict the crystal rotation which is in excellent agreement with experimental results. In addition, the model can predict the dominant slip system.

8.6 Prediction capability of CPFE model base on new parameters based on the calibration of tensile test

In order to compare the capability of the new model, the differences in kinematic of plastic deformation is compared in Figure 8.14(b) by overlaying the predicted shape of the deformed solder using CPFE model based upon **Table 8.5** and the computationally deformed sample using CPFE utilizing the hardening values that are tabulated in **Table 5.3**. Although these two results are quite similar but compared to real deformed microstructure (Figure 8.14(c)) the new model shows more similarities in terms of kinematics of plastic deformation. Also, the values of shear stress predicted by hardening parameters that are obtained in this chapter (Figure 8.14(a)) are more realistic compared to the values that are discussed in chapter 6 (Figure 6.7(b)).

8.7 Summary and conclusion

A CPFE model was proposed in this chapter to account for the relative activity of slip systems in SAC305. A statistical analysis was introduced to define a correlation of the critical resolve shear stress and the probability of activating each slip systems. In order to verify the model, joint scale solder joints were fabricated. To characterize these samples non-destructively, Synchrotron X-ray microdiffraction experiments on beamline 34-ID-E as well as high energy monochromatic X-ray beam experiments at the Advanced Photon Source (APS) at Argonne National Laboratory were employed. In addition, radiographic investigation was conducted

before and after deformation to check the quality of samples in terms of voids and porosities and to assess the mechanism that controls the damage evolution.

The results of simulations show that the CPFE model that is developed based on the statistical analysis of the activity of slip systems not only can satisfy the requirements associated with kinematic of plastic deformation in crystal (activity of slip systems) and global (shape changes) coordinate systems, but also is able to predict the evolution of stress effectively in joint-scale SAC305 samples.
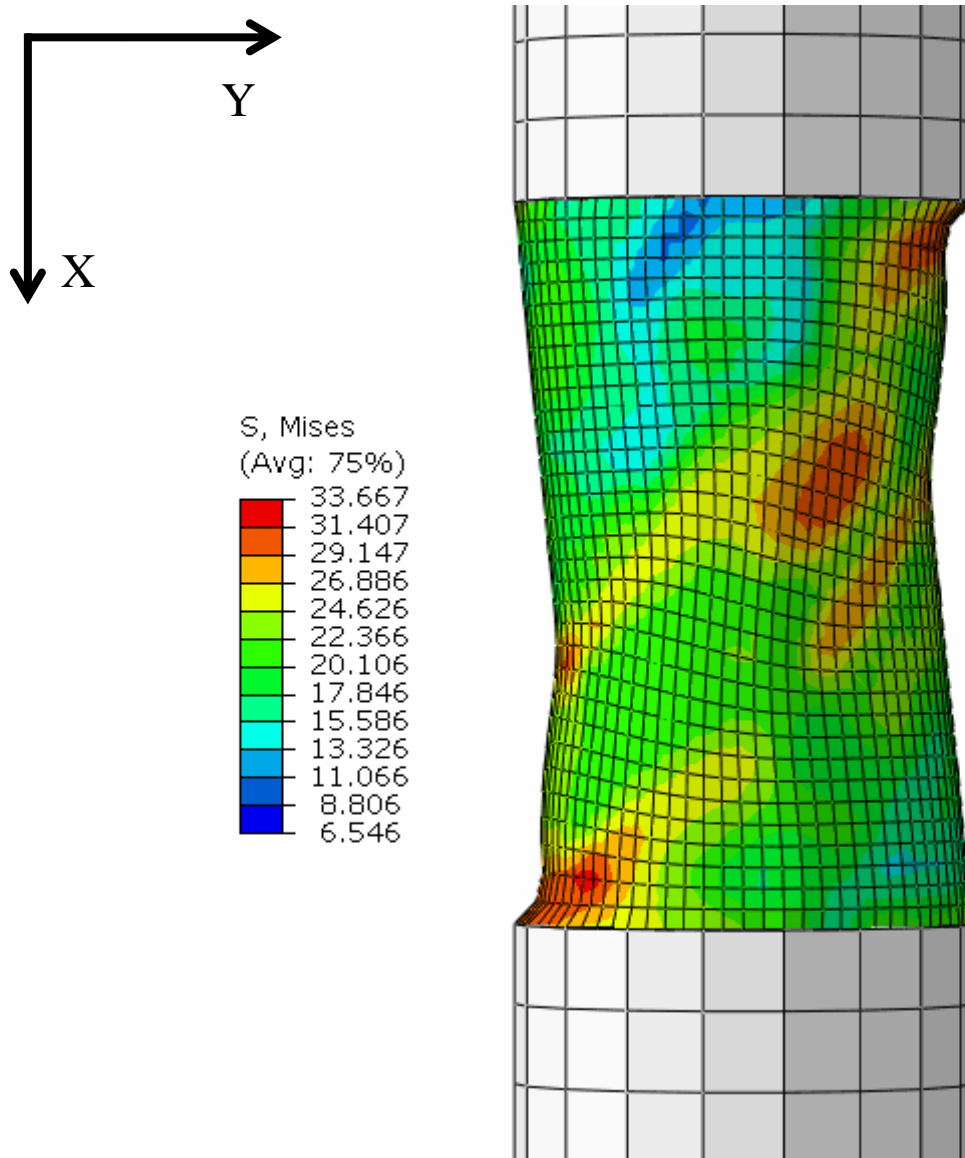
Figure 8.10 Distribution of von-Mises stress in sample-12 obtained using the CPFE modeling. Localization of the stress and rotation of the sample is predicted.
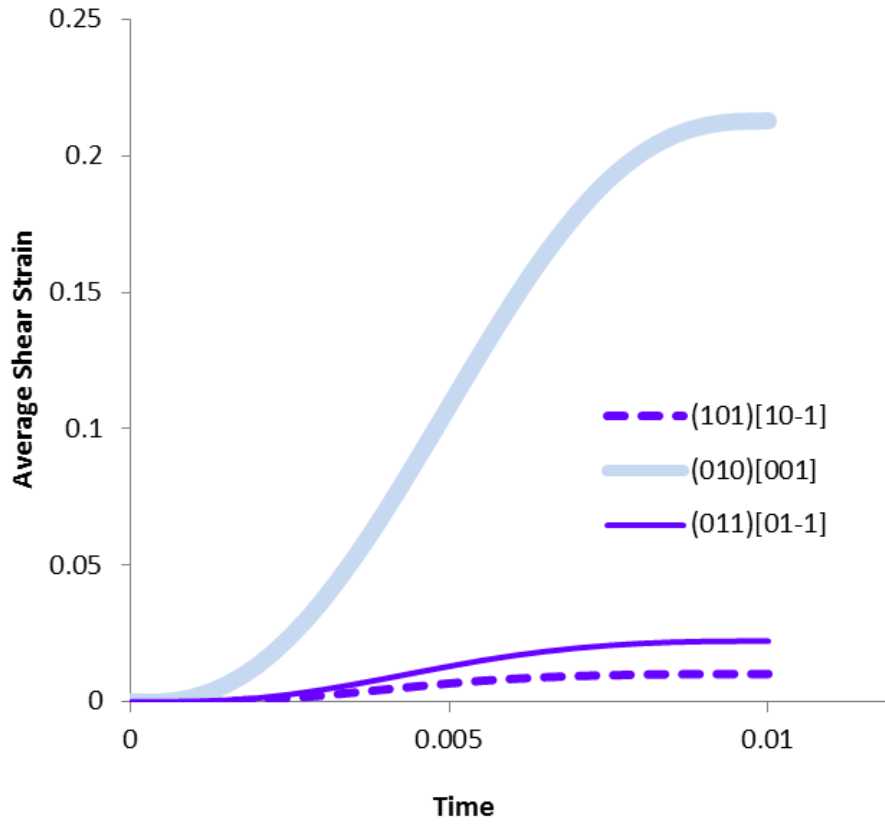
Figure 8.11 Comparison of the average activity in sample 12 predicts three active slip systems, with one dominant, during tensile deformation.
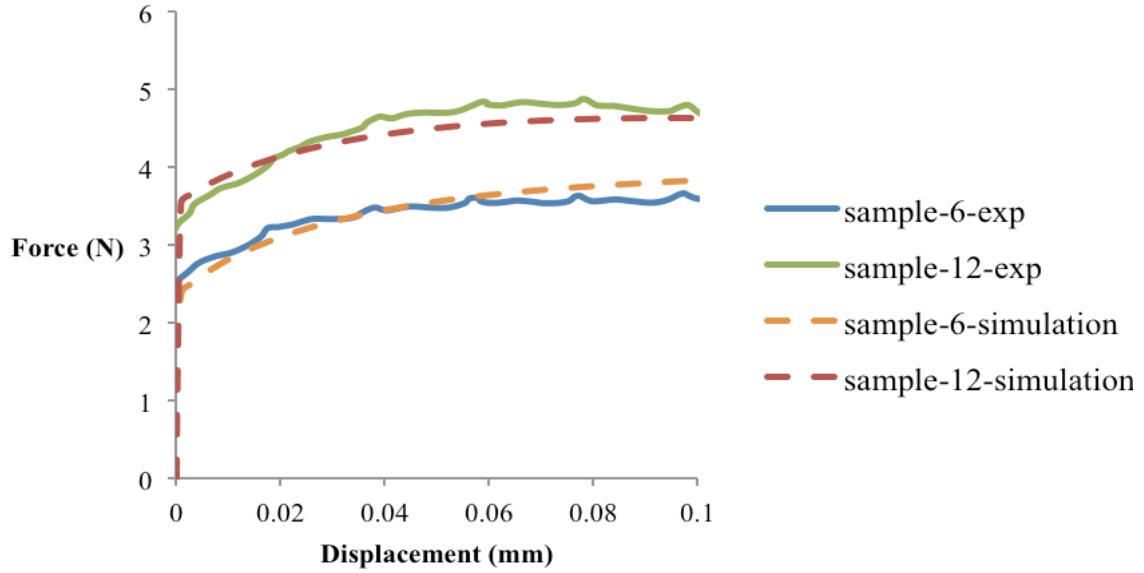
Figure 8.12 Force displacement for two tensile deformed samples 6 and 12 (solid lines) dashed lines shows the simulation results. Curve fitting was conducted based on the assessments on the relative activity of slip systems.

(a)

(b)

0.3697248
0.3393739
0.3090230
0.2786722
0.2483213
0.2179704
0.1876196
0.1572687
0.1269179
0.0965670
0.0662161
0.0358653
0.0055144

[010][001], m=0.403

(c)
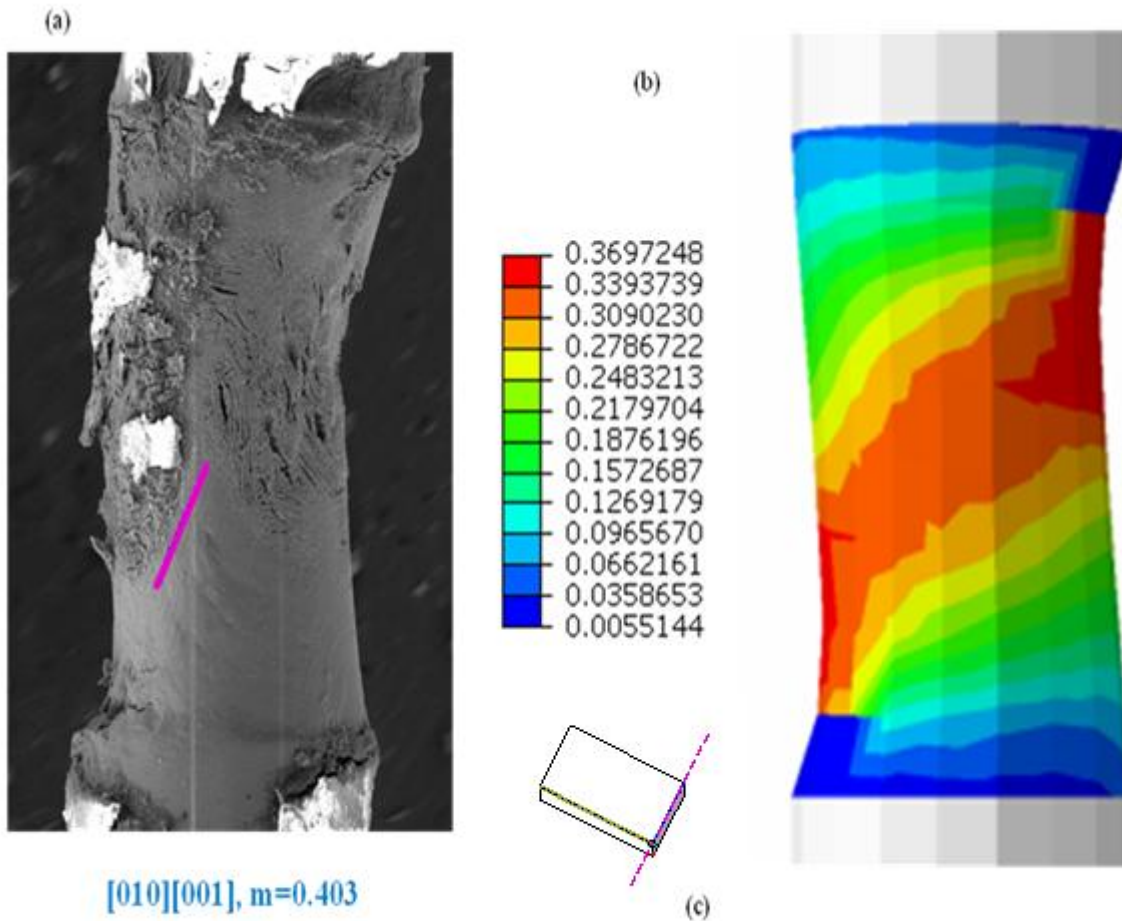
Figure 8.13   SEM image of sample 12 shows the slip plane traces on the surface, sample rotation and shear localization after shear deformation. Plane traces (magenta line) shows that slip system mode 2 is the most active slip systems (a) CPFE simulation of sample 12 predicts that slip system mode 2 is the most active slip system (b). Crystal structure of tin shows the joint orientation and slip trace (c).
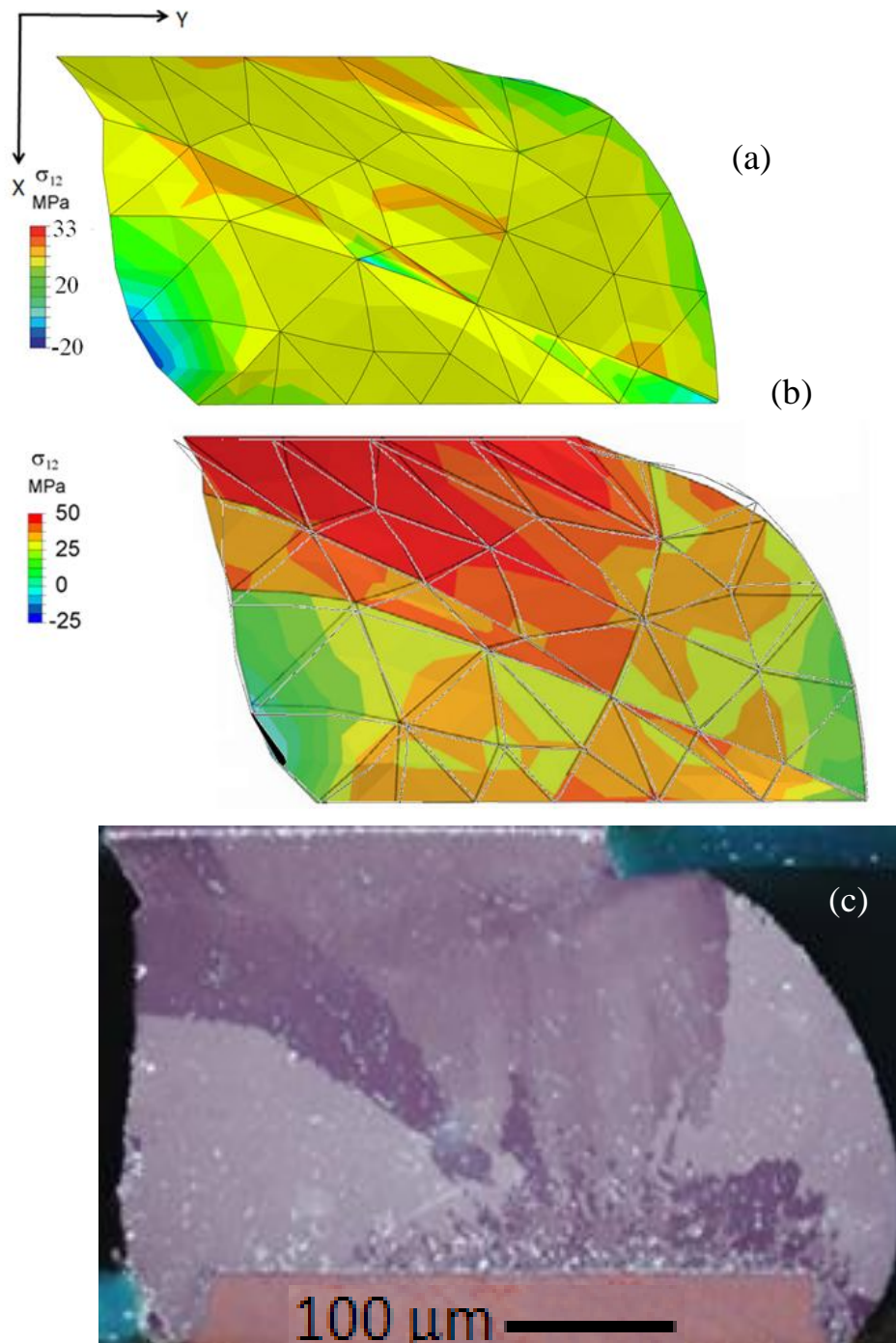
Figure 8.14 Deformed solder ball predicted by CPFE utilizing the material parameters tabulated in Table 8.5 indicating more realistic values of stress compared to Figure 6.7 (a) Comparison of the outline of the model illustrated in (a) and Figure 6.7 (b) indicating the similarity in kinematic of deformation predicted by both models. Polarized light micrograph of beach ball microstructure that was modeled in (a) and (b).

CHAPTER 9

CONCLUDING REMARKS AND FUTURE WORKS

9.1 Concluding Remarks

Anisotropy is of significant importance in all structural metals, but this characteristic is unusually strong in Sn, making Sn based solder joints one of the best examples of the influence of anisotropy. The mechanical properties and damage evolution in SAC 305 alloys strongly depends on the underlying microstructures. The existence of single or multi-grain microstructure in this alloy causes each joint to exhibit a unique mechanical response to stress and strain history. This dissertation provides an improved understanding of the modeling of anisotropy in the elastic and plastic behavior of SAC solder at sub-mm length scales, using a combination of microstructural and mechanical characterization and crystal plasticity finite element (CPFE) modeling approaches.

In developing a mechanistic framework based upon the crystal plasticity finite element modeling of idealized geometries, insights are provided into the effects of initial coarse-grained Sn microstructures and orientations on joint-dependent deformation behavior of SAC305 solders. Furthermore, the capability of a CPFE model to capture the kinematics of in-homogeneous plastic deformation in microstructures that are commonly observed in real SAC305 solders, activity of slip systems and evolution of micro structural features is successfully examined using simple assumptions about the hardening parameters.

The critical issue in modeling of plastic anisotropy is the lack of understanding about the relative ease in activating various slip systems. There is especially uncertainty about the critical resolved shear stress values and hardening characteristics in SAC 305 alloys. To provide more

understanding regarding the activity of slip systems in SAC 305 alloys, experimental investigations were conducted utilizing the orientation imaging microscopy, SEM and plane trace analysis on shear deformed samples.

An improved CPFE model was developed based on a combination statistical analysis on probability of observation of various slip systems in SAC 305 and systematic modeling of tensile tests on joint scale single crystal solder tensile specimens. In this model a correlation is observed between the critical resolved shear stress and the probability of activating different slip systems.

In order to validate this model, joint scale solder tensile samples were fabricated and characterized non-destructively using Synchrotron X-ray micro diffraction on beamline 34-ID-E as well as high energy monochromatic X-ray beam on beamline 6 at the Advanced Photon Source (APS) at Argonne National Laboratory. In addition, radiographic investigations were conducted before and after deformation to check the quality of samples in terms of voids and porosity to understand the mechanism that controls the stress-strain and damage evolution. The results of simulation show that the CPFE model that is developed based on the statistical analysis of activity of slip system not only can satisfy the requirements associated with kinematic of plastic deformation in crystal coordinate systems (activity of slip systems) and global coordinate system (shape changes) but also this model is able to predict the evolution of stress in joint level SAC 305 samples.

9.2 Recommendation for future works

The results of this study are applicable to the mechanical response of solders at low temperature, high strain-rate loading conditions where plastic deformation dominates over creep. Regarding

the further improvement of this model and future development in this area several recommendations are provided as follows:

1- All finite element simulations performed in this thesis were based on this assumption that deformation occurs at room temperature. Development of temperature sensitive models requires further investigation in terms of implementing a temperature dependent activation energy that has been measured in existing experimental studies.

2- Since the experimental measurements and the microstructural evidence indicates that dislocation climb is an important deformation mode [Ghoniem et. al (1990)] in creep deformation, CPFE models based upon the dislocation density can be developed to model the creep in these alloys.

3- Rate effects are another area of interest that can be especially important for modeling of shock performance in SAC 305. This characteristic is very important regarding the reliability of electronic products. Correlating of the shock performance and microstructure is a subject of increasing interest as electronic systems become more portable.

4- Since the CPFE modeling is naturally time expensive, macro scale modeling approaches (which are less time consuming) can be developed by defining an anisotropic yield function based on the CPFE analysis. In this approach the coefficients in the yield function can be defined utilizing the CPFE modeling. Further experimental data in different directions (including joint level shear test and compression test) are required to develop these models.

5- The size effects which are a very important feature of miniaturization cannot be captured using this CPFE model. The above crystal plasticity models can be further improved by

179

implementing the idea of non-local continuum theory to take into account the size effect relevant to microstructure features and deformation mechanisms to make a more accurate model.

6- Another important future research topic is to consider damage prediction in material models. Further work can be conducted to implement damage in the proposed crystal plasticity models. Damage can be implemented in these crystal plasticity models by using several micro-scale damage parameters which evolve with deformation or time. These micro-scale parameters can be a function of temperature and microstructural parameters. These crystal plasticity models can then be used to obtain macro-scale damage parameters for the material.

BIBLIOGRAPHY

BIBLIOGRAPHY

Abtew M. and Selvaduray G., 2000, Lead-free solders in microelectronics, MAT SCI ENG R, Vol. 27, No. 5-6, 95-141.

Adams, P.J., 1986. Thermal fatigue of solder joints in micro-electronic devices, Thesis, MIT. Anand, L., 1982, .Constitutive Equations for the Rate-Dependent Deformation of Metals at Elevated Temperatures, ASME Journal of Engineering Materials and Technology, 104, 12-17.

Asaro, RJ., Needleman, A. 1985, Overview no. 42 Texture development and strain hardening in rate dependent polycrystals, Acta Metallurgica 33, 923.

Bai ,Ning Chen, Xu, , 2009. A new unified constitutive model with short- and long-range back stress for lead-free solders of Sn–3Ag–0.5Cu and Sn–0.7Cu. International Journal of Plasticity, Volume 25, Issue 11, Pages 2181-2203.

Benard D. 2003, Implications of Using Lead-Free Solders on X-ray Inspection of Flip Chips and BGAs, SMTA International Conference Proceedings.

Bieler T. R. , Zhou B. , Blair L. , Zamiri A. , Darbandi P. , Pourboghrat F. , Lee T.-K. and Liu K.Ch. 2012, The Role of Elastic and Plastic Anisotropy of Sn in Recrystallization and Damage Evolution During Thermal Cycling in SAC305 Solder Joints J. Electron. Mater, 41, 283.

Bieler T. R. , Zhou B. , Blair L. , Zamiri A. , Darbandi P. , Pourboghrat F. , Lee T.-K. and K.Ch. Liu 2011, The Role of Elastic and Plastic Anisotropy of Sn in Recrystallization and Damage Evolution During Thermal Cycling in SAC305 Solder Joints Paper 5F.1 Piscataway, NJ: IRPS/IEEE,, p. IRPS11-573-81.

Bieler T.R., Lee T.-K., and Liu K.C. 2009, Methodology for Analyzing Strain States During In Situ Thermomechanical Cycling in Individual Lead-Free Solder Joints Using Synchrotron Radiation J. Electron.Mater.38, 2712.

Bieler T. R. , Telang A.U., 2009. Analysis of slip behavior in a single shear lap lead free solder joint during simple shear at 25°C and 0.1/s," Journal of Electronic Materials J. Electron.Mater. 38 12, 2694.

Bieler T.R., Jiang H., Lehman L.P., Kirkpatrick.T., Cotts. E.J., Nandagopal Joints 2008, Influence of Sn Grain Size and Orientation on the Thermomechanical Response and Reliability of Pb-free Solder IEEE Trans. Compon. Packag.Technol. 31, 370.

Boyce, B. L. ,Brewer, L. N. , Neilsen. M. K. , Perricone.M. J. 2011, On the Strain Rate- and Temperature-Dependent tensile Behavior of Eutectic Sn–Pb Solder. Journal of Electronic Packaging, 133 ,1009.

Bower, A. F., Wininger E. 2004 A two-dimensional finite element method for simulating the constitutive response and microstructure of polycrystals during high temperature plastic deformation, Journal of the Mechanics and Physics of Solids, 52, 1289 – 1317.

Bunge, H. J. (1982). Texture Analysis in Materials Sciences. Mathematical Methods. Butterworths Publ. London.

Busso, E. P., Kitano, M. and Kumazawa, T., 1992 .A Visco-Plastic Constitutive Model for 60/40 Tin-Lead Solder Used in IC Package Joints. ASME Journal Eng. Materials and Technology, V. 114, 331-337.

Busso, E. P., Kitano, M. and Kumazawa, T., 1994 .Modelling Complex Inelastic Deformation Processes in IC Packages' Solder Joints. Journal of Electronic Packaging, V. 116, 1994, 6-15.

Brown, S. B., Kim, K. H., and Anand, L., 1989, .An Internal Variable Constitutive Model for Hot Working of Metals. International Journal of Plasticity, 5, 95-130.

Darveaux R. et al. 2005, Shear Deformation of Lead Free Solder Joints Electronic Components and Technology Conference.
Deshpande V.T. and Sirdeshmukh D.B. 1962)., Thermal expansion of tin in the β-γ transition region Acta Cryst. 15, 294.

Desai C. S., 1997. Disturbed state unified constitutive modelling for thermomechanical behavior and computer analysis of chip-substrate systems. Proc., Interpak, Advances in Electronic Packaging, E.

Dieter.N, 1976, Mechanical metallurgy,NY, MacGraw-Hill.
Ding Y, Wang Ch., Tian Y, Li M., (2007), Influence of aging treatment on deformation behavior of 96.5Sn3.5Ag lead-free solder alloy during in situ tensile tests, Journal of Alloys and Compounds 428 274–285.

Dong. H., Fan .L., Moon. K.S., Wong. C. P. 2005,Conference Molecular Dynamics Simulation of Lead Free Solder for Low Temperature Reflow Applications, Electronic Components and Technology,1,4, 983 – 987.

Düzgün B. and Aytaş I., 1993, Investigation of operative slip system in β-Sn single crystal and the relation between the crystal orientation and the slip systems, JPN J APPL PHYS, Vol. 32, No. 7, 3214-3216.

Düzgün B., Ekinci A.E., Karaman I., and Ucar N., 1999 Investigation of dislocation movements and deformation characteristics in beta -Sn single crystals J. Mech. Behav.Mater.10, 187.

Daymond M. R. and Withers P. J., 1996, A synchrotron radiation study of transient internal strain changes during the early stages of thermal cycling in an Al/SiCw MMC, SCRIPTA MATER, Vol. 35, No. 10, 1229-1234.

Dingley D. J. and Babakishi K., 1986, Use of electron back scatter diffraction patterns for determination of crystal symmetry elements, SCAN ELECTRON MICROS, Vol. 2, 383-391.

Ekinci A.E., Ucar N., Cankaya G., Duzgun B., 2003, Flow behavior of beta Sn single crystals Indian J. Eng. Mater. Sci. 10 5, 416.

Fiedler R. and Lang A. R., 1972, Dislocation generation at surfaces of tin single crystals, J MATER SCI, Vol. 7, No. 5, 531-542 .

Fiedler R. and Vagera I., 1975, On the Burgers vectors in β-Sn single crystals, PHYS STATUS SOLIDI A, Vol. 32, No. 2, 419-424.

Honda K., 1978, Configuration, formation and Burgers vector of coupled dislocations straddling a polygon wall in white tin single crystals, JPN J APPL PHYS, Vol. 17, No. 1, 33-41.

Honda K., 1979, Dislocation walls consisting of double arrays in white tin single crystals, JPN J APPL PHYS, Vol. 18, No. 2, 215-224 .

Honda K., 1987, Dislocation reactions in a boundary of a white tin crystal, JPN J APPL PHYS, Vol. 26, No. 4, 637-638.

Ice G. E., Larson B. C., Tischler J. Z., Liu W., and Yang W., 2005, X-ray microbeam measurements of subgrain stress distributions in polycrystalline materials, MAT SCI ENG A-STRUCT, Vol. 399, No. 1-2, 43-48.

Fujiwara M. and Hirokawa T., The Strength of Main. 1987 Obstacles to Dislocation Motion in White Tin Crystals J. Jpn. Inst. Met.51, 830.

Fujiwara.M. and Hirokawa. T, 1986, Jpn. J. Appl. Phys., Part 1 Regular Papers & Short Notes), 25, 1598.

Gao, F , Qu J. ; F.Z.,L., Williams, R.L., 2010. Interfacial failure simulation of single solder joint using a multiscale approach .Thermal and Thermo-mechanical Phenomena in Electronic Systems ITherm), 12th IEEE Intersociety Conference on, 1-6.

Gong J., Ch. Liu, Conway P. P., Silberschmidt V. V. 2007 , Micromechanical modelling of SnAgCu solder joint under cyclic loading: Effect of grain orientation Computational Materials Science 39, 187.

Gong J., Liu Ch., Conway P. P., Silberschmidt V. V., 2006 . Micromechanical modelling of SnAgCu solder joint under cyclic loading: Effect of grain orientation Computational Materials Science 43 199.

Ghoniem, N. M., Matthews,J. R., and Amodeo.R. J. 1990 . A dislocation model for creep in engineering materials. Res Mechanica, 29:197–219.

Henderson ,D.W., Woods, J.J., Gosselin, T.A., Bartelo J., King, Korhonen, D.E., , Korhonen, T.M..M.A., Lehman. L.P., Cotts. E.J., Kang S.K, Lauro. P., Shih, D-Y., C. Goldsmith, and K.P. Puttlitz, 2004 .The microstructure of Sn in near-eutectic Sn–Ag–Cu alloy solder joints and its role in thermomechanical fatigue. J. Mater. Res. 19, 1608.

Herkommer, Reid, and Punch 2009 in Situ Optical Creep Observation of Joint-Scale Tin–Silver–Copper Solder Shear Samples, J. Electron. Mater.38, 2085.

He, Y, Xu Chen, Bai N. , 2006 Simulation of Sn-0.7cu solder with Bonder-Paraton constitutive model. Thermal and Thermomechanical Phenomena in Electronics Systems, 2006. ITHERM '06. The Tenth Intersociety Conference on, 984 – 989.

Hill, R, 1966 . Generalized constitutive relations for incremental deformation of metal crystals by multislip , Journal of the Mechanics and Physics of Solids14, 95.

Hill.R. 1948 . A theory of the yielding and plastic flow of anisotropic metals. Proc. Roy. Soc. London, 193:281–297.
Hutchison, J.W. 1976 Elastic-plastic behaviour of polycrystalline metals and composites Proceedings of the Royal Society of London Series A 319, 247.

House D.G. and Vernon E.V., Br. J. 1960 , Determination of the elastic moduli of tin single crystals, and their variation with temperature, Appl. Phys. 11, 254.

Johnson, G. R., and Cook, W. H., 1983 , .A Constitutive Model and Data for Metals Subjected to Large Strains, High Strain Rates and High Temperatures. Proceedings of the 7th International Symposium on Ballistics, pp. 541–547.

Ju .S.H, Sandra, B.I, Plesha,M.E. 1996 Life Prediction of Solder Joints by Damage and Fracture Mechanics., J. Electron. Packag., 118, 4, 193.

Kim,K.S., Huh, S.H., and Suganuma.K., 2002 .Effects of cooling speed on microstructure and tensile properties of Sn – Ag – Cu alloys. Mater. Sci. Eng. A333, 106.
Kouhashi. Y., 2000 Sendai: Transactions of the Japanese Society for Strength and Fracture of Materials, , 12, 15.

Kapoor, R., Nemat-Nasser, S., 1999 . High rate deformation of single crystal tantalum: Temperature dependence and latent hardening. Scripta Materialia 40 ,2, 159.

Keer. W. S. , L. M., Vaynman, S. and Lawson, L. R., 2002 .A constitutive model for a high lead solder. IEEE Trans. on Components and Packaging Technology, vol. 25, pp. 23–31

Lebensohn R.A. and Tomé C.N. 1993 , A Self-Consistent Anisotropic Approach for the Simulation of Plastic Deformation and Texture Development of Polycrystals—Application to Zirconium Alloys Acta metal. mater., 41 ,2611.

Lehman.L.P., Atavale. S.N., T Fullem.Z., A.C. Giamis, R.K. Kinyanjui, M. Lowenstein, K. Mather, R. Patel, D. Rae, J. Wang, Y. Xing, L. Zavalij, P. Borgesen, and E.J. Cotts 2004, Growth of Sn and intermetallic compounds in Sn-Ag-Cu solder.Journal of Electronic. Materials. 33, 1581.

Lehman L.P., Atavale S.N., Fullem T.Z., Giamis A.C., Kinyanjui R.K., Lowenstein M., K. Mather, Patel R., Rae D., Wang J., Xing Y., Zavalij L., Borgesen P., and Cotts E.J. 2004 , Growth of Sn and intermetallic compounds in Sn-Ag-Cu solder J. Electron. Mater.33, 1581.

Lehman L.P., Xing Y., Bieler T.R., and Cotts E.J. 2010 , Cyclic Twin Nucleation in Tin Based Solder Alloys Acta Mater. 58, 3546.

Li .J., H. Xu, T.T. Mattila, J.K. Kivilahti, T. Laurila, and M. Paulasto-Krockel, 2010 .Simulation of dynamic recrystallization in solder interconnections during thermal cycling. Comput. Mater. Sci. 50, 690.

Liu W., Ice G. E., Larson B. C., Yang W., Tischler J. Z., and Budai J. D., 2004, The three-dimensional X-ray crystal microscope: A new tool for materials characterization, METALL MATER TRANS A, Vol. 35, No. 7, 1963-1967.

Liu W., Ice G. E., Larson B. C., Yang W., and Tischler J. Z., 2005, Nondestructive three-dimensional characterization of grain boundaries by X-ray crystal microscopy, ULTRAMICROSCOPY, Vol. 103, No. 3, 199-204.

Matin M.A., Coenen E.W.C., Vellinga W.P., Geer M.G.D., 2005 Correlation between thermal fatigue and thermal anisotropy in a Pb-free solder alloy Scripta Materialia 53 927–932.

Matin M. A., Vellinga W. P., and Geers M. G. D., 2006, Microstructure evolution in a Pb-free solder alloy during mechanical fatigue, MAT SCI ENG A-STRUCT Vol. 431, No. 1-2, 166-174.

Matin M. A., Vellinga W. P., and Geers M. G. D., 2007, Thermomechanical fatigue damage evolution in SAC solder joints, MAT SCI ENG A-STRUCT Vol. 445-446, 73-85.

Mattila .T. and Kivilahti.J.K., 2010 . The Role of Recrystallization in the Failure of SnAgCu Solder Interconnections Under Thermomechanical Loading. IEEE Trans. Compon. Packag. Technol. 33, 629.

Maciucescu, L., Sham, T.-L., Krempl E., 1999 .Modeling the deformation behavior of a Sn-Pb Solder alloy using the Simplified Viscoplasticity theory based on Overstress. ASME Journal of Electronic Packaging, 121, 92-98.

Mc Dowell, D. L., Miller, M. P. and Brooks, D. C., 1994 .A unified creep-plasticity theory for solder alloys. Fatigue of Electronic Materials, ASTM STP 1153, 42-59.

Mc Dowell, D. L 2000 , .Modeling and experiments in plasticity. International Journal of Solids and Structures 37 , 293-309.

Mills D. M., 2002, Third-generation hard X-ray synchrotron radiation sources: Source properties, Optics, and Experimental Techniques, John Wiley and Sons.

Nagasaka M. 1999 , Strain-Rate and Temperature Dependence of Plastic Deformation in White Tin Single Crystals, Jpn. J. Appl. Phys. Part 1-Regular Papers Short Notes & Review Papers 38 1A, 171.

Obinata J. and Schmid E., 1933, Über die Dehnung von Zinnkristallen, Z PHYS, Vol. 82, No. 3-4, 224-234.

Ojima K. and Hirokawa T., 1983, Motion of individual dislocations in white tin single crystal deformed in tension, JPN J APPL PHYS, Vol. 22, No. 1, 46-51.

Park S., Dhakal R ., Gao J., 2008 Three-Dimensional Finite Element Analysis of Multiple-Grained Lead-Free Solder Interconnects J. Electron.Mater, 37, 8.

Pei. M, Qu. J, 2005 .Constitutive Modeling of Lead-free Solders, Proceedings of ASME InterPACK, July 17-22.

Rayne J.A. and Chandrasekhar B.S. 1960 ., Elastic Constants of β Tin from 4.2°K to 300°K Phys. Rev. 118, 1545.

Sidhu R. S., Madge S. V., Deng X., and Chawla N., 2007, On the nature of the interface between Ag3 Sn intermetallic and Sn in Sn-3.5Ag solder alloys, J ELECTRON MATER, Vol. 36, No. 12, 1615-1620 .

Sidhu R. S. , Chawla N., 2008, Thermal fatigue behavior of Sn-Rich Pb-free solders, METALL MATER TRANS A, Vol. 39, No. 4, 799-810.

Taylor, G.I., 1938 .Plastic strain in metals. Journal of Institutional Metallurgy 62, 307–324.

Telang A.U., Bieler T.R., Zamiri A., and Pourboghrat F., 2007 Incremental grain growth driven by elastic strain energy release in a thermomechanically fatigued lead-free solder joint Acta Mater. 55, 2265.

Telang A.U. and Bieler T.R. 2005 Orientation Imaging Microscopy of Lead-Free Sn-Ag Solder Joints, JOM,57, 44.

Tyte L. C., 1938 , The rate of viscous flow of metals: Part 1, tin, P PHYS SOC, Vol. 50, No. 2, 153-175.

Wang. C. Z., Becker Z., K. and Wilde.J., 2001 .Applying Anand model to represent the viscoplastic deformation behavior of solder alloys. Trans ASME J. Electronic Packaging, Vol. 123, No. 3, 247-253.

Weertman J. and Breen J. E., 1956 , Creep of tin single crystal, J APPL PHYS, Vol. 27, No. 10, 1189-1193.

Wen.S., L ,Keer. M., Mavoori, H., 2001 .Constitutive and Damage Model for a Lead-Free Solder. Journal of electronic materials, 30,. 9.

Whitelaw R S, R W Neu, D T Scott , 1999 .Deformation behavior of two lead-free solders: Indalloy 227 and Castin alloy. Journal of Electronic Packaging , 121, 2, 99-107.

Wilde, J.   Becker, K.   Thoben, M.   Blum, W.   Jupitz, T.   Guozhong Wang   Cheng, Z.N. , 2000 .Rate dependent constitutive relations based on Anand model for 92.5Pb5Sn2.5Ag solder., IEEE Transactions on advanced Packaging, Vol. 23, 408-414.

Xuming.W., Fei.Q., Tong.A., 2011 . A Constitutive Model for Lead-free Solders Considering the Damage Effect at High Strain Rates. International Conference on Electronic Packaging Technology and High Density Packaging.

Yang F. , Li J.C.M., 2007 . Deformation behavior of tin and some tin alloys, J. Mater. Sci.: Mater. Electron.18, 191.

Yao D, Kremple .E. 1985 , Viscoplastic theory based on overstress, International Journal of plasticity. 1., 259-274.

Zhou B., Bieler T. R, T Lee.-K., Liu K.Ch., 2009 , Methodology for Analyzing Slip Behavior in Ball Grid Array Lead Free Solder Joints after Simple Shear J. Electron. Mater. 38, 12, 2702.

Zamiri A., Bieler T.R., and Pourboghrat F., 2009 , Anisotropic Crystal Plasticity Finite Element Modeling of the Effect of Crystal Orientation and Solder Joint Geometry on Deformation after a Temperature Change J. Electron. Mater., 38, 231.

Zamiri A.R., Pourboghrat F., 2010 , A novel yield function for single crystals based on combined constraints optimization International Journal of Plasticity 26, 731.

Zhou, B, 2012 , Characterization of Tin crystal orientation evolution during thermal cycling in lead-free solder joint, PhD thesis.

Zhou B., Bieler h. R, Lee T.-K., Liu K.Ch., 2009, Methodology for analyzing slip behavior in ball grid array lead free solder joints after simple shear , J. Electron. Mater. 38, 12, 2702.